2011

An Optimization-based Approach to Dosimetry Planning for Brachytherapy

Tianhao Tiam Zhang

An Optimization-based Approach to Dosimetry Planning for Brachytherapy

(Spine title: Optimization-based Dosimetry Planning)

(Thesis format: Monograph)

by

Tianhao Tiam Zhang

Graduate Program
in
Engineering Science
Electrical and Computer Engineering

A thesis submitted in partial fulfillment
of the requirements for the degree of
Master of Engineering Science

School of Graduate and Postdoctoral Studies
The University of Western Ontario
London, Ontario, Canada

THE UNIVERSITY OF WESTERN ONTARIO
SCHOOL OF GRADUATE AND POSTDOCTORAL STUDIES

CERTIFICATE OF EXAMINATION

Supervisor	Examiners
Dr. Rajni Patel	Dr. Remus Tutunea-Fatan
	Dr. Mehrdad Kermani
	Dr. Ilia Polushin

The thesis by

Tianhao Tiam Zhang

entitled:

An Optimization-based Approach to Dosimetry Planning for Brachytherapy

is accepted in partial fulfillment of the
requirements for the degree of
Master of Engineering Science

Date_____

_____
Chair of the Thesis Examination Board

Abstract

Prostate cancer is the second leading cause of death from cancer in North American men, with a reported 32,050 deaths in the U.S. alone for 2010; lung cancer is reported as the number one leading cause of death from cancer in both men and women in North America, its estimated death toll in the U.S. alone in 2010 is over 157,000. One method of treating prostate cancer patients nowadays is by Low Dose Rate Brachytherapy, a process where radioactive seeds are placed in or near the tumor site to kill cancerous cells. For lung cancer, brachytherapy has begun to attract attention due to the advent of robotics assistance and there is increasing research currently in the area. While brachytherapy is gaining popularity as a commonly practiced method for treating cancer patients, the procedure itself has several drawbacks that require further research. One such drawback is that the dosimetry plan created based on the pre-operative imaging may not be accurate due to (a) the change in the tumor's size as a result of the time elapsed between pre-operative imaging and seed implantation; and (b) movement of the organ under treatment from the position and orientation in pre-operative imaging; this is particularly important in the case of lung brachytherapy as it would have to take into account lung deflation and respiratory and cardiac motions as well. In addition, seeds may be misplaced during implantation as a result of limitation of the manual or robotic procedures. When this happens, the final dose coverage of the tumor is no longer the same as the intended coverage in the dosimetry plan.

In this thesis, the development, implementation and evaluation of two algorithms are presented. The first algorithm is the pre-planning algorithm, which aims to reduce

the errors in the dosimetry plan caused by the change in the tumor's size by providing a mechanism to perform dosimetry planning on-line. By doing this, the first algorithm can also eliminate the need for the patient to be imaged twice, so that the same set of images can be used for dosimetry planning as well as seed implantation. The second algorithm deals with intra-operative dynamic dose optimization, where real-time seed compensation is performed to compensate for any seed misplacements so that an optimal final coverage can be achieved. The results of the experimental evaluation performed in this project indicate that these algorithms are feasible and have the potential to be applied in the operating room following appropriate animal and clinical validation.

Keywords: LDR Brachytherapy, Lung Cancer, Prostate Cancer, Dosimetry, Pre-planning.

Acknowledgements

First and foremost, I would like to thank my supervisor, Dr. R. Patel during the past two years both for the guidance of this thesis research work and in every aspect of my studies at The University of Western Ontario. It is a priviledge to be his student, for he has been an inspiration and has helped me blossom at both professional and personal levels.

I would also like to thank my colleagues at Canadian Surgical Technologies & Advanced Robotics (CSTAR) for their help and advice throughout my study. In particular, I would like to mention Harman Bassan for helping me during the early stage of my research; also I would like to thank Ana Luisa Trejos and Abelardo Escoto for their assistance with the experimental work.

My special appreciation goes to Joanna Sun, for all her support and effort throughout the writing and proofreading of this thesis. At times she has sacrificed her own work to help with my thesis writing.

Last but not least, I would like to express my deepest gratitude to my parents for their unconditional love, constant encouragement and support in every aspect of my life.

Table of Contents

List of Tables

List of Figures

List of Symbols and Abbreviations

Abbreviation/Symbol	Description	Page Reference
HT	Hormonal Therapy	1
keV	Kilo-electronvolt	1
MeV	Mega-electronvolt	1
EBR	External Beam Radiotherapy	1
LDR	Low Dose Rate	2
MDR	Medium Dose Rate	2
HDR	High Dose Rate	2
TRUS	Transrectal Ultrasound	2
CT	Computed Tomography	2
^{125}**I**	Iodine 125, radioisotope of Iodine 127	3
^{103}**Pd**	Palladium 103, radioisotope of Palladium 106	3
^{192}**Ir**	Ytterbium 169, radioisotope of Ytterbium 173	3
^{137}**Cs**	Cesium 137, radioisotope of Cesium 133	3
^{60}**Co**	Cobalt 60, radioisotope of Cobalt 59	3
$T_{1/2}$	Half life of radionuclide	3
HVL	Half Value Layer	3
PSA	Prostate-Specific Antigen	5
OR	Operating Room	6
US	Ultrasound	6
MRI	Magnetic Resonance Imaging	6
OAR	Organs At Risk	11

Abbreviation/Symbol (cont.)	Description (cont.)	Page Reference (cont.)
IDDO	Intra-operative Dynamic Dose Optimization	14
DDC	Discrete Dynamic Contour	23
IMR	Interventional Magnetic Resonance	25
CSTAR	Canadian Surgical Technologies and Advanced Robotics	25
FFR	Fluroscopic Frame of Reference	27
UFR	Ultrasound Frame of Reference	27
ROI	Region of Interest	28
MIP	Mixed Integer Programming	28
U_b	Accepted upper bound of the prescribed dose	29
L_b	Accepted lower bound of the prescribed dose	29
MIRA	Minimally Invasive Robot-Assisted	32
AAPM	The American Association of Physicists in Medicine	34
$\dot{D}(r)$	Dose rate of radioactive source	34
$D(r)$	Dose of radioactive source	34
τ	Meanlife of radionuclide	34
k_u	Time conversion factor for calculating $D(r)$ from $\dot{D}(r)$	35
DOPAL	Dosimetry preplanning algorithm proposed by this thesis	38
d_h	Spacing between slices in 3D volume contour	39
COM	Center Of Mass	40
temp_seed	Matrix containing locations of temporary seeds to be used for optimization	40

Abbreviation/Symbol (cont.)	Description (cont.)	Page Reference (cont.)
DOPAL_2Dseeds	Seed configuration produced by *2D_Optimization*	41
vio_amt	Amount of violation in the 3D volume in DOPAL	41
overdose_amt	Amount of violation in DOPAL due to overdose	41
underdose_amt	Amount of violation in DOPAL due to underdose	41
seeds_other_slices	Seeds from other slices in the DOPAL algorithm	42
new_DOPAL_seeds	New seeds produced by DOPAL on every optimization iteration	42
2D_Optimization	2D Optimization	42
min_vio	Minimum amount of violation on the current slice of interest	42
vio_pts	Amount of violation on the the current slice	44
3D_Optimization	3D Optimization	45
run_num	Number of times the algorithm had been run	45
S_x	Values for the location of a seed in the x direction for a shape with no forbidden region	48
S_y	Values for the location of a seed in the y direction for a shape with no forbidden region	48
P_x	x coordinates of the contour of a shape with no forbidden region	48
P_y	y coordinates of the contour of a shape with no forbidden region	48

Abbreviation/Symbol (cont.)	Description (cont.)	Page Reference (cont.)
S_{xn}	Boundary values in the x direction for a seed in the n^{th} region	49
S_{yn}	Boundary values in the y direction for a seed in the n^{th} region	49
P_{xo}/P_{xi}	x coordinates of the outer/inner contour of a shape with forbidden region	49
P_{yo}/P_{yi}	y coordinates of the outer/inner contour of a shape with forbidden region	49
cur_seeds	All seeds currently found in the tumor volume	53
vol_contour	The 3D contour describing the tumor volume	53
desd_goal	Desired dosage to be delivered to the target/forbidden region	53
z_val	Value of the z coordinate of the current slice	53
inner_cont	Coordinates of the inner contour	54
outer_cont	Coordinates of the outer contour	54
Obj_fn	Objective Function of DOPAL	54
Opt_Cons	Optimization Constraints of DOPAL	56
DOPAL_3Dseeds	Dosimetry Plan, output of the DOPAL algorithm	59
preplan_seeds	Seeds from dosimetry planning to be used as an input to IDDO	59
cur_dep_seeds	Currently deposited seeds in the tumor volume	59
desd_dose	Intended dose of the preplan calculated from *preplan_seeds*	60
cur_dose	The amount of dose currently delivered to the tumor volume as a result of *cur_dep_seeds*	60

Abbreviation/Symbol (cont.)	Description (cont.)	Page Reference (cont.)
tol_val	Amount of tolerance imposed on *desd_dose* to calculate the UB and LB for IDDO calculations	61
req_dose	Amount of dose required to deliver the desired amount of dose at each point throughout the IDDO volume	62
min_vioamt_IDDO	Volume wise minimum violation amount in IDDO	62
new_seeds_IDDO	New locations for the remaining seeds generated by IDDO	62
cur_vioamt_IDDO	Current amount of violation in the 3D volume in IDDO	62
$\bar{P}_x$	Collection of x coordinates from all slices of the volume	64
$\bar{P}_y$	Collection of y coordinates from all slices of the volume	64
$\bar{P}_z$	Collection of z coordinates from all slices of the volume	64
final_seeds_IDDO	Final seed configuration of IDDO	68
IDDO_Obj_Fn	Objective Function of IDDO	69
IDDO_Opt_Cons	Optimization Constraints of IDDO	69
RDP	Robarts Dosimetry Planning software, provided by Dr. Fenster from the Robarts group	71
DVH	Dose Volume Histogram	78
V90	Volume of the tumor receiving 90% of the prescribed dose	79
D90	The amount of dose delivered to 90% of the tumor volume	79
V100	Volume of the tumor receiving 100% of the prescribed dose	79

Abbreviation/Symbol (cont.)	Description (cont.)	Page Reference (cont.)
V200	Volume of the tumor receiving 200% of the prescribed dose	79
D100	The amount of dose delivered to 100% of the tumor volume	79
V120	Volume of the tumor receiving 120% of the prescribed dose	79
V150	Volume of the tumor receiving 150% of the prescribed dose	79
r_cyl	Radius of the inner Cylindrical volume	84
r_tube	Radius of the outer Cylindrical volume	85
r_sph	Radius of the Spherical volume	85
DNE	Does Not Exist	97
I-3D	Intra-operative 3D algorithm	102
EOD	Extend of Disease	125
DNA	DeoxyriboNucleic Acid	133

Chapter 1

Introduction

Cancer commonly manifests itself as malignant tumors that are fast growing and invade surrounding tissue and cells, new tumor growth can also occur at other locations through a process known as metastasis. Treating the malignant tumor at an early stage is highly desirable to prevent metastases, with surgical removal/resection (such as prostatectomy for prostate cancer or lobectomy for lung cancer) and chemotherapy being the traditional and commonly practiced methods. Other treatment methods are also available, such as the use of Hormonal Therapy (HT) for prostate cancer, which targets one specific type of cancer, is a procedure where testosterone production is decreased.

Radiation therapy is another technique for treating cancer, it uses high energy rays, usually in kilo-electronvolts (keV) or mega-electronvolts (MeV) to kill the tumor [1]. A traditional form of radiation therapy is the External Beam Radiotherapy (EBR). In EBR, keV x-rays, also known as superficial x-rays, are used for skin cancer and superficial structures; whereas MeV x-rays, also known as deep x-rays, are used for tumors that are deeply-seated, such as on the bladder, prostate, lung and brain etc. The application of radiation therapy on internal organs must be done with care since the high energy beam kills all cells that are within range, be it cancerous or healthy. Therefore the most difficult task in radiation therapy is to target the tumor cells only.

1.1 Prostate and Lung Brachytherapy

Brachytherapy, which translates to short-range-therapy, is a more recent development in radiation therapy compared to EBR. The biggest advantage of brachytherapy over other treatment methods from radiation therapy is that it is both safer and less time-consuming. In brachytherapy, it is possible to achieve a high ratio of cancer dose to normal tissue dose by placing radiation sources inside or next to cancerous tissue, thus avoiding harming normal and healthy tissue during the treatment process, and is an improvement over EBR. Nevertheless, no method is proven to be 100% safe and all may lead to undesirable side effects.

There are mainly three categories of brachytherapy in use today, they are Low Dose Rate (LDR), Medium Dose Rate (MDR) and High Dose Rate (HDR). The biggest difference between all these categories is the dose administered to the patient during treatment. For example, LDR is generally between $0.4Gy$[1] to $2Gy$ per hour, MDR is from $2Gy$ to $12Gy$ per hour, while HDR is usually more than $12Gy$ per hour. The focus of this thesis is on LDR brachytherapy in the prostate and the lung.

The LDR brachytherapy treatment procedure involves permanently placing the radioactive seeds inside the patient, which is why it can also be referred to as permanent brachytherapy, is usually composed of four steps with the support of several medical imaging modalities, such as transrectal ultrasound (TRUS), computed tomography (CT) and radiography. The first step, which is known as pre-implant volume study, uses either TRUS or CT to determine the volume of the target [2, 3, 4]; the second step is called pre-planning, where a dosimetry plan is created by the radiation oncologist in an off-line environment; thus no imaging is required for this step. TRUS

1. Gray (symbol: Gy) is the SI unit of absorbed radiation dose of ionizing radiation. $1Gy = 1\frac{J}{kg} = 1m^2 \cdot s^{-2}$

and radiography are usually used in step three, which is commonly known as seed implantation [2, 3]. CT is required some time after the implant to assess the quality of the procedure in step four, known as post-implantation [2, 3].

1.1.1 Brachytherapy Seeds

According to [5], there are three types of seeds commonly selected for interstitial brachytherapy, they are Iodine 125 (^{125}I), Palladium 103 (^{103}Pd) and Iridium 192 (^{192}Ir), while the less frequently used seeds are, Cesium 137 (^{137}Cs) and Cobalt 60 (^{60}Co). All the elements listed above are the unstable radioisotopes of their stable atoms. For instance, the stable atom of Iodine has 53 protons and 74 neutrons, the sum of which gives an atomic mass of 127 for the stable form of Iodine. The radioisotope ^{125}I on the other hand, has only 72 neutrons. Similarly, ^{103}Pd has 57 neutrons while the stable ^{106}Pd has 60 neutrons. A more detailed description on the properties and radioactivity of ^{125}I are given in Appendix D. Section 1.1.1.1 discusses ^{125}I in more detail; here ^{103}Pd and ^{192}Ir are briefly examined.

The short half-life ($T_{1/2}$) of ^{103}Pd of 17.0 days means that it is only good for permanent implants [5], and is a common replacement for ^{125}I in permanent brachytherapy. Even the geometries of ^{103}Pd sources are very comparable to that of ^{125}I sources. The high initial dose rate of ^{103}Pd is appropriate when applied in interstitial implantation of rapidly proliferating tumors. The Half Value Layer (HVL) for ^{103}Pd at $0.008mm$ is lower than the HVL for ^{125}I, which is given by [6] as $0.025mm$. HVL is discussed in more detail in Appendix D.

^{192}Ir, has a longer half-life at 73.83 days [5]. They appear as small cylindrical sources for interstitial use in the United States, which are approximately $3mm$ long and $0.5mm$ in diameter. In Europe however, ^{192}Ir is most commonly used in the

Figure 1.1: Size of brachytherapy seeds

form of a wire. As reported in [7], ^{192}Ir has now established itself as the preferred radionuclide for all temporary brachytherapy applications, which are not LDR.

1.1.1.1 Iodine 125

By comparison, ^{125}I is by far the most commonly used seed for LDR brachytherapy (details on the decay and radioactivity of ^{125}I are given in Appendix D). Three models of the ^{125}I seeds are available, they are the 6702 and 6711 type manufactured by Amersham and the 2300 type marketed by Best Industries. The 2300 type is said to be more isotropic in dose pattern due to the presence of iodine on the ends of the seed and on the surface of the tungsten wire that is inside the titanium encapsulation [8]. Even though the design and appearance of one seed differs from those of another, the size of all these seeds are generally no bigger than a grain of rice.

This thesis uses the 6711 model of ^{125}I seed by Amersham; reference [5] provides detailed information on this type of seed. The half-life, $T_{1/2}$, of this seed is given by [5] as 59.4 days, which translates to 1426 hours. This type of seed is approximately $4.5mm$ in length, and its diameter is about $0.8mm$, enclosed in a $0.05mm$ thick

titanium wall. This seed type offers air kerma strength of up to $6.3U$[2], which is equivalent to an apparent activity of $5mCi$[3]. The interior design of the Amersham seed consists of a hollow cylinder made of a double-walled titanium tube. Two of the advantages offered by this designed are that, one there is a higher isotropy of the irradiation field around the source, and two there is a reduced chance of seed migration [7].

1.1.2 State-of-the-art Prostate Brachytherapy

Despite brachytherapy being more advantageous than other radiation therapy treatment methods as mentioned previously, it is not always recommended for all cancer patients. Even when brachytherapy is selected as the primary treatment method, additional therapy is sometimes required to complete the treatment process [6]. Regardless of the treatment strategy employed, the long-term cure rate is always favorable for patients with early stage cancer. For example, patients with low-risk prostate cancer are usually recommended for the four-step prostate brachytherapy. Low-risk prostate cancer is defined for patients that have a Prostate-Specific Antigen (PSA) level of $10ng/mL$ or less, a Gleason score of 6 or less, and clinical stage T2a or less [6]. PSA, the Gleason score and prostate cancer staging are discussed in more detail in Appendix A. The reason for choosing the four-step procedure for low-risk prostate cancer is that the disease would be more likely to have been confined to the prostate in these patients. In addition, there are other factors that could influence the decision to offer brachytherapy, such as the size of the prostate must be less than $60cc$ [9]. Once a patient is found to have met these criteria, and thus be eligible for prostate

2. U, unit for air kerma strength, usually specified at $1m$. $1U = 1\mu Gy \cdot m^2 \cdot h^{-1}$ [5]

3. Curie (symbol: Ci) is a unit of radioactivity. $1Ci = 3.7 \times 10^{10}$ decays per second

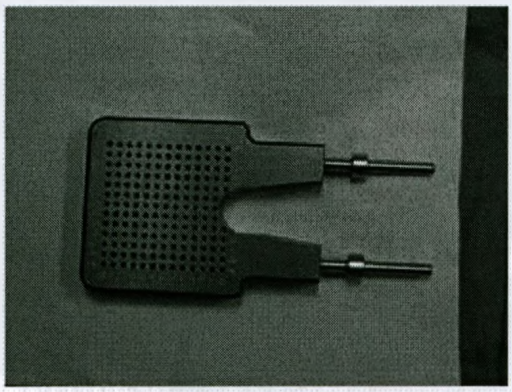

Figure 1.2: A sample seed template used for prostate brachytherapy

brachytherapy, an ultrasound-guided prostate volume study must be performed as the first step.

1.1.2.1 Step 1 - Pre-implant Volume Study

During the volume study, the size of the gland and the relation of the gland to the pubic arch are assessed; this study also determines the target volume and tracks the urethra through the prostate. This volume study is carried out with the patient sedated in the lithotomy (treatment) position [9], usually with the aid of a TRUS probe to visualize the prostate in the transverse and sagittal dimensions [10]. This probe is mounted on a stabilization apparatus that's affixed to the Operating Room (OR) table with a template grid attached, the angle of the mount and the probe are recorded. A sample template is shown in Fig. 1.2, the purpose of which is to assist needle insertion. The probe is then lubricated with ultrasound (US) jelly before being inserted into the rectum, this is to reduce air interference between the US probe and the rectal wall to achieve the best visualization of the prostate. CT or Magnetic Resonance Imaging (MRI) could also be used in place of US, though due to practical

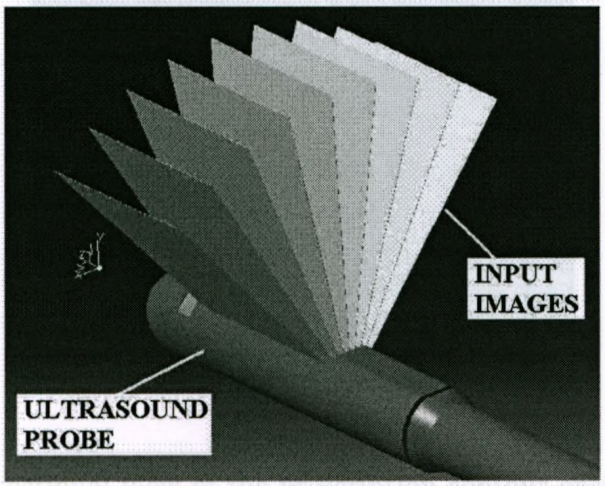

Figure 1.3: TRUS probe and 2D input US images

operating room constraints, these modalities are only available at a limited number of institutions [10].

The set of images of the prostate are acquired at $< 1^{\circ}$ intervals by the TRUS probe as the probe is rotated about its axis. The acquired images appear as a fan and are in polar coordinates. A polar to rectangular transformation is required to construct the 3D volume in cartesian coordinates before these images can be used for contouring purposes. Figure 1.3 shows a graphical representation of the probe and the images obtained which are then used as input images for the polar to rectangular transformation.

Once the prostate and the surrounding organs are displayed, contours can be defined to identify the target and normal tissues. The contours of the target, namely the prostate, should then be compared with the length of the prostate that was measured on the sagittal views, the volume of the gland should also be recorded for comparison purposes. Hormonal treatment may be applied to abnormally large glands to shrink the prostate, the volume of which may decrease by as much as one third

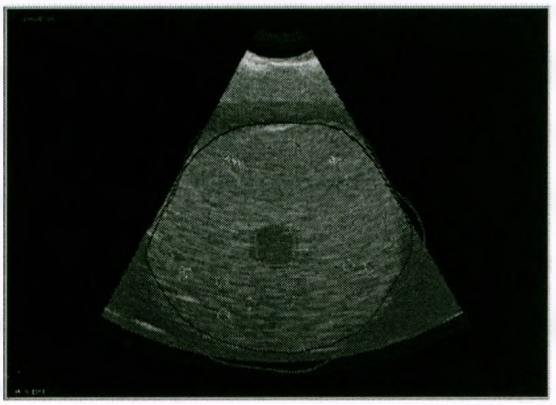

Figure 1.4: Cross-sectional view of the prescription contour enclosing the prostate

within 4 months of the treatment. For a prostate volume that is within the defined limits, these contours and images can be transferred to a treatment-planning system for step two of the procedure known as dosimetry planning, which is explained in the next paragraph. The current image acquisition software found in clinics superimposes a series of dots on the US images, which correspond to the holes in the seed template.

1.1.2.2 Step 2 - Pre-planning

The second step is called dosimetry planning, or pre-planning, the aim of which is to calculate the seed positions required to deliver the desired dose to the entire tumor volume [2]. During dosimetry planning, the intention is to enclose every cross-sectional image of the prostate within the prescription dose contour, as shown in Fig. 1.4. This is to ensure that the entire gland can receive a proper dose, since the size of the prostate gland is relatively small. Pre-planning for lung cancer is rather different, where only the tumors (and a specified margin around them) are to receive the prescribed dose and not the entire organ.

In any case, there are usually dosimetry constraints that govern the dosimetry

planning process. For example, a constraint of dosimetry planning for the prostate is the amount of dose that can be delivered to the urethra. Reference [2] suggests that as much as 125% of the prescribed dose can be delivered to the urethra, even though the dose to the urethra should be kept as low as possible. Other constraints may include the dose to the rectum and to the boundary of the prostate itself. All in all, dosimetry planning tries to limit the number of low-dose regions or "cold spots", which may lead to tumor relapse, while the number of high-dose regions or "hot spots" in normal tissues must also be limited, which may result in late complications [6] such as the killing or damaging of healthy tissue. Due to the presence of the seed template, the brachytherapy seeds are generally spaced at $10mm$ in the cranio-caudal direction, which would be the direction coming out of the page as in Fig. 1.4. In Cartesian coordinates, if the cranio-caudal direction is intepreted as the z-axis, then the seeds are spaced at $5mm$ or more in the x and y directions, which are co-planar to the direction shown by view in Fig. 1.4.

1.1.2.3 Step 3 - Seed Implantation

Seed implantation is the next step after dosimetry planning, which usually takes place a few weeks after the volume study has been done [2]. Before loading the seeds into the brachytherapy needles for implatation, the seeds are unpacked first and then their activity is checked in a calibrator. The activity defines the number of disintegrations within a given time for a particular radioactive source, which is a measure of how radioactive the source is; activity is discussed in more detail in Appendix C. The loading and checking of the seeds are done under sterile conditions. The seeds are then loaded in to the needles according to the dosimetry plan, also called a pre-plan. A sample pre-plan of prostate brachytherapy is shown in Fig. 1.5, which contains information for the 'hole location' of the needles expressed in terms of an alphabet and

Needle Number	Retraction (cm)	Hole Location	Number of Seeds
1*	3.00	c4.5	1
2	1.50	D4.0	3
3	1.50	E4.0	3
4	1.50	b3.5	2
5	1.50	C3.5	3
6	1.50	e3.5	3
7	2.00	a3.0	2
8	2.00	F3.0	3
9*	1.50	G3.0	1
10	1.50	B2.5	2
11	1.00	b2.5	3
12	1.00	F2.5	4
13*	4.00	D2.0	1
14	0.50	E2.0	2
15	1.50	f2.0	2
16	2.00	B1.5	2
17	0.50	c1.5	4
18	2.00	a1.5	3
19	2.00	F1.5	2
20	2.00	b1.0	2
21	2.00	E1.0	2
* Indicates special loading			

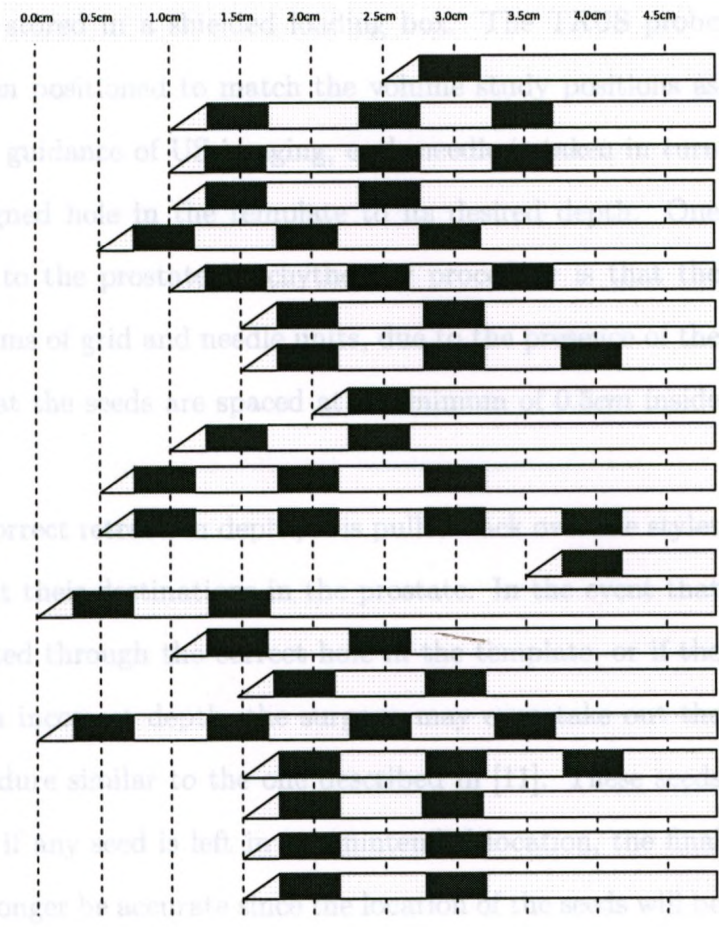

Figure 1.5: A sample pre-plan for prostate brachytherapy

a number that corresponds to the horizontal and vertical indices on the seed template to provide the exact location of where the needle should be inserted. Furthermore, the plan contains information on the depth at which the seeds should be deposited, indicated by the values under 'retraction'. The preloaded needles with the seeds are kept within a shielded vault, they are only taken out of the vault and handed to the physician when he or she is ready to insert each individual needle.

A stylet is placed after the train of seeds in each needle in order to push the seeds out once the needle has been deposited at its destination. To protect the patient and staff while the patient is being anaesthetised and placed in the lithotomy position

again, the loaded needles are stored in a shielded loading box. The TRUS probe and the seed template are then positioned to match the volume study positions as closely as possible. Under the guidance of US imaging, each needle is taken in turn and inserted through its assigned hole in the template to its desired depth. One limitation related specifically to the prostate brachytherapy procedure is that the seeds can only be placed in terms of grid and needle units, due to the presence of the seed template and the fact that the seeds are spaced at a minimum of $0.5cm$ inside the needles.

Once the needle is at the correct retraction depth, it is pulled back over the stylet to deposit the train of seeds at their destinations in the prostate. In the event that the needle has not been inserted through the correct hole in the template, or if the seed has been deposited at an incorrect depth, the surgeon may even take out the misplaced seeds using a procedure similar to the one described in [11]. These seeds need to be taken out because if any seed is left in an unintended location, the final coverage of the tumor will no longer be accurate since the location of the seeds will be different to the pre-plan. The used needle and stylet are discarded and the rest of the needles are inserted in the way described above. At the end of this step, radiography is used to check the positioning of the seeds. The post-implant dosimetry check-up, which is step four of the procedure, must be performed some time after the seed implantation has taken place.

1.1.2.4 Step 4 - Post-implant Check-up

The post-implant check-up is usually conducted using CT, the main goal of this step is for quality control purposes, as well as evaluating the dosimetry to the surrounding Organs At Risk (OAR). The time between seed implantation and post-implant check-up have been suggested as anywhere between 1 to 30 days after seed implantation [9].

According to [9], most post-implant check-up is done 4 weeks after implantation to allow the edema to subside. Ultrasound is not used in this step because the artifacts from the implanted seeds may cause image degradation. The CT images are imported into a treatment-planning system to identify the seeds in the prostate and analyze the dosimetry data based on the contours defined for the prostate. The data of importance are discussed in more detail in section 4.3.

The four-step prostate brachytherapy procedure described above suffers from a change in the size and volume of the prostate between volume study and seed implantation, as mentioned previously in section 1.1.3 and in [9]. As a result, intra-operative planning has been reported in [2], [6] and [9]. One advantage discussed in these literature is the improved accuracy of seed implantation since both the volume study and seed implantation are carried out at the same time, which effectively avoids any changes to the prostate compared to the four-step procedure; whereas in the four-step procedure the time spent waiting between the volume study and the actual implantation might be long enough for the tumor to expand. Another advantage is that the patient is required to be sedated only one time such that minimal discomfort exists whereas in the four-step procedure the patient must undergo sedation for both volume study and seed implantation which means there is more discomfort. The disadvantage, as mentioned in [2], is that more seeds tend to be wasted since the precise number of seeds required is unknown in advance and they must be unpacked and loaded in the OR.

1.1.3 Procedural Deficiencies

As mentioned above, the brachytherapy procedure at the moment is far from perfect. In the prostate brachytherapy procedure, the dosimetry plan created in step two is

based on the US images obtained from step one. The time between the creation of the pre-plan to seed implantation in step three can be long enough for the tumor size to change. Thus a pre-plan may no longer be accurate by the time seed implantation takes place [12]. The multiple TRUS imaging sessions could also create a certain amount of discrepancy between the US images acquired at different times as it is generally not possible to place the patient and insert the rectal probe in exactly the same way as before. Furthermore, seed misplacement was hard to avoid because of shifts in the prostate, tissue deformation and needle flexing. This makes the post-implantation session an absolute necessity to check the actual coverage obtained after the seed implantation.

Compared with prostate brachytherapy, there is relatively little work done to date on lung brachytherapy. Much of the work is still at a research stage with additional interest created by the availability of surgical robotic systems where, in [13] the accuracy of manual seed implantation is compared to that of the ZEUS robot. Nonetheless, the accuracy of the current lung brachytherapy procedure has also been suffering from drawbacks such as the changes in tumor's size and location between pre-planning and seed implantation, as well as the inability to compensate for inaccurate seed placements [14]. The procedure is further complicated by the more sensitive area and the need to perform brachytherapy in the presence of motion (respiratory and cardiac).

1.2 Research Motivation

Given some of the drawbacks of the brachytherapy procedure at the current stage, the motivation behind this research is to reduce the errors in the brachytherapy procedure with reference to the lung and prostate brachytherapy. As mentioned

before in section 1.1.2, a seed template is currently used to control the placement of seeds inside the tumor. However, the template may also be a nuisance in the sense that the template grid that is overlaid on the tumor in the pre-operative images are different to the template grid seen during actual implantation, which might lead to inaccurate dosimetry results; also seed misplacements may occur if a needle is inserted through the incorrect hole in the template. With the advances in medical robotics, the elimination of the template can prevent these errors mentioned above, where seeds can be deposited anywhere inside the tumor from any angle as desired. To this end, this research is conducted based on the availability of such a robotics set-up, which is described in more detail in section 4.1.1.2.

In particular, this research consists of two components, which are the pre-planning or dosimetry planning component, and the intra-operative dynamic dose optimization (IDDO) component. The first component attempts to provide a means for the online generation of a dosimetry plan for use in seed implantation, effectively reducing the time span between dose planning and seed implantation. The IDDO component aims to compensate for seed misplacements by updating the dosimetry plan dynamically to ensure that an optimal coverage is achieved at the end of the procedure. Post-implantation evaluation is still required nonetheless, to verify the actual seed locations against the desired seed locations, i.e. to verify that the desired radiation coverage is achieved.

1.2.1 Goal of Pre-planning

The goal of the pre-planning component is to generate seed locations to deliver the prescribed dose to the target volume in on-line mode, in other words, to create the dosimetry plan in real-time. In doing so, the same images that are used to generate the

dosimetry plan are also used during the actual implantation of the seeds; meanwhile the time span between the dosimetry planning step and the seed implantation step is reduced to a minimum. The pre-planning component essentially combines steps one and two of the four-step procedure described previously, thus reducing the amount of error that is present in the current four-step procedure between the intended tumor coverage of dosimetry planning and the actual tumor coverage at the end of seed implantation. There are mainly two factors that contribute to this error.

One is imaging errors between dosimetry planning (pre-planning) and seed implantation, because dosimetry planning is carried out on the US images obtained during pre-implant volume study (section 1.1.2), while seed implantation is performed on a new set of real-time US images obtained in the OR during treatment. Since the images for the pre-planning step (which is taken at pre-implant volume study) and the seed implantation step are taken at different times and possibly different locations, it is very important that the patient, and the equipment are positioned in exactly the same way in both steps in order to obtain identical images in both steps. However, during seed implantation, it is nearly impossible to duplicate exactly the position of the patient and equipment from before, even though the angle of the mounting apparatus of the probe and the angle of the probe itself are recorded during pre-implant volume study as mentioned in section 1.1.2. Even the smallest discrepancy between how the equipment or patient have been placed from one step to the other might lead to a significant amount of error between the images for pre-planning and seed implantation. This will ultimately lead to a discrepancy between the intended coverage of the tumor which is based on images from pre-implant volume study and the actual coverage of the tumor which is based on a different set of images.

Another factor is due to the waiting time (usually a few weeks) in the currently practiced brachytherapy procedure between the off-line dosimetry planning and actual

seed implantation. The dosimetry plan is created based on the US tumor images obtained during pre-implant volume study, and the seeds are deposited in the tumor volume according to this plan during seed implantation. The time elapsed between pre-planning and seed implantation may have caused a change in the size and shape of the tumor, and thereby the dosimetry plan for the pre-implant tumor may no longer be appropriate for the tumor at seed implantation, even if the patient and equipment have somehow been placed in exactly the same way in both steps.

To this end, the aim of the pre-planning component is to solve these problems by doing everything 'on-line', from pre-implant volume study to creating the dosimetry plan, which would then be ready to be used for immediate seed implantation. Thus ideally only one US imaging session would be required, during which time pre-implant imaging, dosimetry planning, as well as seed implantation (which are the first three steps in the commonly practiced four-step procedure for brachytherapy) would all take place, thereby minimizing errors caused by different positioning of the patient or equipment during a later session; as well as minimizing errors caused by the natural growth of the tumor itself because the exact same images are used for both pre-planning and seed implantation and that the time elapsed between the steps are very short. Thus, as long as the seeds are deposited accurately according to the dosimetry plan, the actual coverage of the tumor at the end of seed implantation will be much closer to, if not exactly the same as, the intended coverage at pre-planning.

1.2.2 Goal of IDDO

The second component of this research - Intra-operative Dynamic Dose Optimization, involves performing optimization in real-time in order to compensate for any seed misplacements.

As described in section 1.2.1, the seeds must be accurately deposited according to the pre-plan in order to achieve the intended radiation coverage of the tumor. Though, as mentioned in section 1.1.2, needles can sometimes be inserted through the wrong hole in the seed template or the seeds themselves may be deposited at an incorrect depth. On top of these preventable human errors, there are other errors that are not preventable which will lead to a different coverage of the tumor volume as compared to the one from pre-planning. These errors may again be caused by the difference in the positioning of the patient and/or equipment from pre-implant imaging to seed implantation as in the case of prostate brachytherapy. As described in section 1.1.2, the current dosimetry planning software overlays the seed template grid on top of the US images, and thus the dosimetry plan is created with a pre-defined position of the seed template. It has been mentioned in section 1.2.1 that during the seed implantation step, it is difficult to mount the seed template exactly according to how it was done in pre-implant volume study. However, the template position from the pre-implant volume study is assumed by the dosimetry planning software as the template position that is used during seed implantation too. As such, during seed implantation, it might not be possible to deposit the seeds at their intended destinations due to a shifted seed template.

To account for this drawback, and therefore to compensate for any seed deviations, the IDDO component is used to generate a new dosimetry plan in real-time to best meet the intentions of the dosimetry plan as specified during pre-planning. IDDO can also compensate for seed misplacements due to tissue shift, needle bending or deflection. The IDDO component is necessary to guarantee that the best possible coverage can be achieved, thus eliminating the repetition or extension of the brachytherapy treatment. In the end, a post-implant check-up can be performed to ensure that adequate dosimetry coverage has been achieved.

1.3 Thesis Contribution

As a whole, this thesis improves upon the current LDR brachytherapy method with particular reference to prostate and lung cancer. In particular, one contribution of this thesis is to improve the accuracy of the overall procedure by performing dosimetry planning on-line. In terms of the four-step procedure, this implies that pre-implant volume study, dosimetry planning, and seed implantation are all performed together, thus reducing any errors that could be caused by the different positioning of the patient and/or equipment, or by the natural growth of the tumor, between pre-operative imaging and treatment. In addition, the dosimetry planning in the four-step procedure is created off-line because it is quite time consuming since it is commonly done by the radiation oncologist by an educated guess. Achieving on-line dosimetry planning by this thesis effectively leads to the creation of a more accurate plan in very little time, which in turn would lead to a more complete and accurate coverage of the tumor volume.

The other major contribution of this thesis lies in the real-time compensation for any misplaced seeds during seed implantation, thereby ensuring that an optimal dose can be delivered to the entire tumor by the end of the procedure. Compensation for seed misplacement is in fact absent in the currently practiced four-step procedure, however seed misplacements do occur in the OR as mentioned previously in section 1.1.2. By introducing real-time compensation for seed misplacements, in the event that seeds are deposited incorrectly or even if the dosimetry plan does not provide a complete coverage to the tumor volume, new seed locations can be generated on-the-fly so to speak to achieve the intended dose so that the final coverage of the tumor volume would still be satisfactory and the overall procedure would be more successful.

Both of the contributions described above are novel contributions in brachyther-

apy, and will particularly improve the LDR brachytherapy treatment technique for prostate cancer and provide a viable approach for dosimetry planning for lung cancer. Application to the lung and the prostate are of particular interest in this thesis because for North American men, prostate cancer is the most commonly found cancer and the second leading cause of death from cancer [15, 16], while lung cancer is the most common cancer found in both genders worldwide [17] and it is the number one leading cause of death from cancer [15, 16, 17].

Another contribution of this thesis is the use of these algorithms with the aid of a robotic-assisted brachytherpay set-up (which is described in more detail in section 4.1.1.2) under image-guidance, where seed insertion can be performed from various angles and there is no restriction of seed separation or discrete locations because a template is no longer in place. It is important to develop online dosimetry planning approaches and also online procedure for correcting the effect of implantation errors as they have been done in this project so that a more complete coverage of the tumor can be obtained to take the brachytherapy procedure for the prostate, lung and possibly other organs, to the next level.

1.4 Organization of Thesis

Chapter 2 of this thesis presents an overview of the current research topics on lung and prostate brachytherapy. The details on the formulation of the optimization problems for dosimetry planning and seed compensation components are presented in Chapter 3 while the experimental results are described in Chapter 4. Chapter 5 concludes the thesis by summarizing the achievements of this work, as well as outlining future research on the topic.

Chapter 2

Background and Literature Review

This chapter presents a review of the work done in this field, specifically on the development of real-time intra-operative planning for prostate brachytherapy (section 2.1.1). While there is currently not much work in the area of lung brachytherapy, an overview of some of the recent research work is presented in section 2.1.2 to show that this a promising treatment for lung cancer. Modeling of brachytherapy seeds is discussed briefly in section 2.2, and section 2.3 presents the parameters involved in calculating the dose delivered by brachytherapy sources.

2.1 Current Work

In the following, first the development of intra-operative dosimetry for prostate brachytherapy is described; followed by a description of some of the work in the area for the development of lung brachytherapy.

2.1.1 Prostate Brachytherapy

Referring back to the dosimetry planning step in the four-step procedure for prostate brachytherapy from section 1.1.2, it is generally not possible to deliver the exact amount of desired dose to the target volume while providing precise coverage at the boundaries of the treatment region, thus the solution to the dosimetry planning

problem becomes one of finding the 'optimal' solution [18]. This section starts with a brief history on prostate brachytherapy, before introducing the current research on intra-operative planning for prostate brachytherapy.

2.1.1.1 Background

In 1917, treating prostate cancer using prostate brachytherapy involved inserting radium needles transperineally [19]. Up to the 1960s, various radioactive substitutive materials were tried as a replacement for radium in prostate brachytherapy, including colloidal gold. It is mentioned in [20] that a transrectal ultrasound that was developed for use in prostate biopsies was extended to the implantation of iodine seeds. With the improvements in US imaging, the improved visualization of the prostate and surrounding structures lead to the first major attempt at prostate brachytherapy using ^{125}I seeds in 1972 at the Memorial Hospital in New York [21]. In this work, the seeds were implanted by the retropubic approach, which is through a lower abdominal incision. Another attempt made in 1987 also used the retropubic approach [22]. Poor long term results were reported in [23] as due to the poor geometrical arrangement as a result of the implantation method. The US and perineal template combination insertion method was refined by Ragde and his colleagues in Seattle [24], which was later taken up across North America. Real-time implantation of permanent source into the prostate was introduced at the Mount Sinai Medical Center in New York in 1990 [25].

Since then, much research and development have been devoted to the field of prostate brachytherapy, the focus of which is particularly on real-time implantation and intra-operative optimized planning. The sections below will describe some commercial systems, as well as current research that is trying to achieve real-time implantation and intra-operative planning.

2.1.1.2 Commercially Available Systems

The commercially available systems presented in [12] are the Interplant System (Burdette Medical System, Champaign, IL); PIPER (RTek, Pittsford, NY) which is short for Prostate Implant Planning Engine for Radiotherapy; SPOT (Nucletron Corporation, Veenandaal, Netherlands) which is short for Sonographic Planning for Oncology Treatment; Strata (Rosses Medical Systems, Columbia, MD); and VariSeed (Varian Medical Systems, Palo Alto, CA).

The Interplant System uses a built-in optical encoder to register the US images in real-time against the probe and template positions, thus providing instant feedback of the probe position within the prostate. Seed positions are estimated from the probe position and the needle track, so the plan can be updated if required [12].

The PIPER system offers automatic segmentation of the prostate, rectum and urethra on TRUS images, which can all be done in less than 2 minutes [12]. Live TRUS is used to identify the needle tracks, from which the needle path can be determined. The seeds are assumed to lie at their pre-planned positions in the z direction, so that compensations for deviations in the x and y directions can be done through an iterative process of isodose review, and dosimetry data analysis.

SPOT uses 3D US to identify the needles and seeds as they are implanted into the prostate volume. However, manual intervention is often required to localize many of the seeds and needles. The resulting absolute or percentage dosimetry data can be displayed with respect to the absolute, or percentage prostate volume [26]. In Strata, the seeds are assumed to have been deposited at their pre-planned locations, based on needle information extracted from TRUS and sagittal US images [26].

The VariSeed system assumes that the needles run straight and do not deviate [12], and the tip of the needles are identified using TRUS. As the seeds are inserted, their

positions are marked on the planning system, and the corresponding isodose curves are generated. As mentioned in [26], this system does not account for intra-operative seed motion.

2.1.1.3 Image Guidance & Robot Assisted Approach

In modern prostate brachytherapy, free-hand seed implantation has been replaced by the image guidance of MRI, TRUS [27], as well as fluoroscopy imaging. The ability of TRUS in providing real-time localization of the prostate and needles at the same time has seen TRUS being used as the primary source of image guidance in brachytherapy procedures nowadays. Due to the inherent noise in US images, segmentation of the prostate gland is commonly done manually, which is a tedious and time-consuming process if the planning is to be done intra-operatively. Reference [27] describes a method where US images are pre-processed to remove noise and increase the contrast, in order to segment the prostate gland automatically.

A four-step procedure has been proposed in [28, 29], where 3D TRUS guidance has been used throughout to achieve dynamic intra-operative prostate brachytherapy. The first step involves the semiautomatic segmentation of the prostate using a Discrete Dynamic Contour (DDC) model. The segmentation of the prostate is an iterative process where four points must be selected on an initial slice to start the segmentation process. The DDC model has been used in a similar fashion to the work in [30, 31, 32], which involves segmentation of the prostate using the DDC model. In the second step, the 3D dosimetry planning for the segmented volume is based on geometric optimization and simulated annealing. To perform dynamic replanning and intra-operative dosimetry evaluation, needles and seeds are located in the 3D TRUS images in steps three and four, respectively. The accuracy of the overall brachytherapy

procedure in [29] is further enhanced by the assistance of a robot, where the needle targeting accuracy has been reported to be $0.79mm \pm 0.32mm$.

Another method utilizing real-time TRUS guidance for dynamic intra-operative prostate brachytherapy has been proposed in [33], where the treatment planning software is supplied with real-time TRUS images. Each seed is identified in real-time by the dosimetrist with concurrence by the clinician, based on the needle tip that is visible in the sagittal view. In this work, real-time feedback of the deposited seeds forces the treatment planning software to update the dosimetry, with regard to the implanted seeds and seeds that are yet to be implanted. When the dosimetry result on 90% of the target is showing a difference of more than 5% from the intended dose, a re-plan is required. The re-plan takes into account the effect of the deposited seeds and generates a new dosimetry plan for the remaining seeds. Reference [33] reports satisfactory results in terms of dosimetry parameters, because there are no significant differences between the intra-operative dosimetry and the post-implant evaluation.

Reference [34] describes a technique that allows for accurate seed and needle placement also by using real-time US feedback. The technique does not require pre-planning and dynamically implants seeds into the prostate, taking into account prostate motion during implantation. In this work, the prostate volume is calculated from the US images in both transverse and longitudinal directions. Without the need for a pre-plan, the needles are then inserted based on the dosimetry evaluation from idealized and prior implants. In particular, [34] mentions that 60% to 70% of the needles will be inserted into the periphery of the gland, while the remaining needles are inserted into the interior of the gland. The seeds are then deposited using the Mick applicator. As mentioned in this work, the major advantage is the elimination of the time-consuming pre-planning. A similar technique has also been described in [35].

An iterative algorithm has been described by [36], where one seed is placed at each step to achieve an optimal coverge of the prostate, using real-time interventional magnetic resonance (IMR). The use of real-time IMR can provide both geometric and dosimetric feedback during needle placement. In this work, the position of the needles are observed before the sources are placed, especially for needles that have been placed incorrectly. Incorporating this information into the treatment plan, and thereby evaluating the dose to the entire target volume at each step, the underdosed regions can then be determined as to where the next seed will be placed. The pre-planned coverage reported in this work suggested that the prescribed dose covered at least 93% of the tumor; though as much as 13% coverage of the tumor was lost after updating the plan with real-time needle feedback.

A robotics-based prostate brachytherapy setup has also been developed at CSTAR (Canadian Surgical Technologies and Advanced Robotics) [37]. Force interaction between the needle and tissue are used to detect and control the location of needles and accurate placement of seeds inside the prostate. The same subject is discussed in a different paper in [38], in which the main focus is put on controlling the trajectory of the needle after insertion. Reference [38] proposes rotating the needle at particular locations during insertion in an attempt to insert the needle according to its desired trajectory. In particular, the developed algorithm is applicable for a period of time during a prostate brachytherapy procedure when imaging feedback is unavailable. Although the intention of this work is to improve the accuracy of needle insertion prior to visulization of the needle tip on the US screen, the authors also plan to integrate their work with real-time imaging to better control the motions of the needle once they are near the target.

2.1.1.4 Image Registration Approach

In [39], both TRUS and fluoroscopy are used to perform real-time dosimetry for prostate brachytherapy. TRUS and fluoroscopic images are registered using a single fluoroscopic image of the TRUS probe, edges of the probe are found in the fluoroscopic image by using an intensity-based edge detector and a least-squares fit. The tip of the needle, which is a white flash, is manually located in the TRUS image. The seeds are modelled as line sources, where the x, z coordinates of the seeds are determined from fluoroscopic images while the y coordinates of the seeds are determined from TRUS images. Based on the location of the seeds, dosimetry due to the currently deposited seeds can be calculated, and underdosed regions can be identified, so that the radiation oncologist can perform interactive planning and update the plan if necessary.

Reference [40] proposed performing intra-operative dosimetry for prostate brachytherpay by the use of a nonisocentric C-arm, where the fluoroscopic images are registered to the US images. Fluoroscopy images of intraprostatic sources and fluoroscopy tracking fiducial (FTRAC) are taken from multiple angles, so that the source positions can be superimposed onto the US images of the prostate by running a source segmentation algorithm that computes the fluoroscopy angle from the fiducial image. The source segmentation was carried out by a morphologic top-hat transform, followed by thresholding and region labeling to obtain the regions that are source-like. Registration of US to fluoroscopy (RUF) is performed twice, once after the placement of approximately half of the planned seeds, and then after the completion of the placement of all planned seeds. During RUF, a set of 4-5 C-arm images is obtained. The sources are reconstructed in the US space, before they are exported to the treatment planning system, where the deposited sources can be removed from the original plan

to generate a 'residual implant plan'. Based on the 'residual implant plan', the physician can modify the remainder of the seeds to optimize the overall plan. This work presented the results from six patients, in all of which at least 88% of the tumor volume received 100% of the prescribed dose. The consequence of this however, is an undesired high dose (> 98% of the prescribed dose) to 30% of the urethra.

Elsewhere, in [41], the dynamic dose optimization relies on the updated structure volumes by registering images from the Fluoroscopic Frame of Reference (FFR) to the Ultrasound Frame of Reference (UFR). The FFR is the system of axes imposed by the C-arm geometry, while the UFR is the system of axes determined by the US probe and seed template. The contours of the prostate, and other structures are outlined by the physician in the UFR. In this work, first the coordinates of the seeds are automatically calculated with reference to the FFR. Then, the images from the FFR space is fused together with the UFR, which is done by identifying reference points (lead markers) in both the FFR and the UFR. The reference points are non-coplanar x-ray opaque markers imbedded in the US probe, so that they are visible in both frames. Generally speaking, five to seven markers are required to minimize errors. The transformation that allows the superposition of the two sets of markers effectively defines the translation-rotation transformation between the two systems. The lead markers are extracted from a grey-level image (fluoroscopic image) of the implanted seeds. The seeds must also be identified in each image, however separating a single seed from a cluster of two or more seeds is an apparent difficulty. Lastly, by verifying the results after registering images from the FFR to the UFR, a decision can be made regarding whether re-planning is necessary.

2.1.1.5 Algorithm-based Approach

Reference [42] describes a method for treatment planning using the ^{125}I or ^{103}Pd seeds by calculating the dosimetry data in the volume before the placement of each individual seed, and thus determining the underdosed regions in the tumor and where the next seeds should be placed. The optimal seed configuration is one that has the minimum total activity due to all of the implanted seeds. The clinical results showed an improvement over the older treatment methods.

The algorithm developed by [43] for the purpose of intra-operative real-time planning is based on region of interest (ROI) adjoint functions. The adjoint functions have been defined as the sensitivity of the average dose in the ROI to a unit-strength brachytherapy source at any seed postion. Using the ratio of target to critical structure adjoint functions, the seed positions are ranked according to the amount of radiation delivered to the target ROI versus the critical structure ROIs. Before the optimization process, this ratio is computed for all seed positions, so that the optimization process can select the appropriate seed position according to the computed ratio values. The main achievement in this work is that the proposed algorithm is about 1500 times faster than the branch-and-bound Mixed Integer-Programming (MIP) model.

The work by Alterovitz focuses on using Linear Programming for HDR brachytherapy, the goal here is also aimed at delivering a desired amount of dose to the target volume [44]. In this work, it is also stated that the objective function values have been significantly improved using linear programming than using Simulated Annealing. Due to the nature of the optimization technique, the potential seed locations are discretized in this work.

In [45], a genetic algorithm for the optimization of prostate implants was carried

out on an idealized model using ^{103}Pd sources. In this work, the coordinates of the template grid within the field-of-view of the target volume's image are encoded into a fixed-length linear string, where 0 indicates no seed placement and 1 indicates a seed has been placed. The algorithm presented is based on varying the distributions of needles and sources. In paticular, the quality of the source distributions has been expressed in such a way as to reflect dosimetric and clinical considerations, so that an optimal coverage can be achieved in the end. The results showed improvement over the implantation of unoptimized implants for the same given target volumes.

Several MIP models have been proposed by [46], where the optimization involved a number of branch-and-bound strategies. The focus of this work is on two dimensional prostate contours, where near-optimal seed placements are generated in less than five minutes on a 333 MHz machine; the extension to the three dimensional case involves the appropriate interrelation of a sequence of the two dimensional problems.

Lee's MIP Models

Lee's optimization approach in solving the dosimetry planning problem in [47] employs the MIP algorithm. Due to this integer-based approach, the seed space must be discretized. In this work, the variable x_j is used to record the placement ($x_j = 1$) or non-placement ($x_j = 0$) of a seed at point j, where n is the total number of points available and X_j is the vector of the coordinates of point j. Two models are proposed in [18], the essence of these models is to deliver an optimal dose to the target volume, while constraining the dose delivered within an upper and lower limit. However, it is stated in their work that it is generally not possible to satisfy all the constraints.

The first model tries to maximize the number of points that will satisfy U_b and L_b, by first identifying a maximum feasible subsystem. U_b is defined as the accepted upper bound of the prescribed dose, usually at more than 100%, while L_b is defined

as accepted lower bound of the prescribed dose, usually at less than 100%. The constraints of this model are given below in Eq. (2.1),

$$\begin{aligned} \sum_{j=1}^{n} D(\|P - X_j\|)x_j + N_p(1 - v_p^L) \geq L_b \\ \sum_{j=1}^{n} D(\|P - X_j\|)x_j - M_p(1 - v_p^U) \leq U_b \end{aligned} \tag{2.1}$$

where P is a vector corresponding to the coordinates of the point of interest, so then for $x_j = 1$, $D(\|P - X_j\|)$ refers to the dose at point P due to the j^{th} seed at location X_j. In this equation, v_p^L and v_p^U have values of 0 or 1, and M_p and N_p are positive constants. The goal of this model is to deliver a final dose that lies within the bounds L_b and U_b, thus forcing v_p^L and v_p^U to be 1. The goal is stated as follows,

$$\text{Maximize } \sum_{p}(\alpha_p v_p^L + \beta_p v_p^U + \gamma_p v_p^{LU}) \tag{2.2}$$

In Eq. (2.2), α_p and β_p are weighting factors to reflect that certain points might be more critical to achieve the target dose level than others. $v_p^L = 1$ implies that the dose at point p is $\geq L_b$, though the dose might even be greater than the imposed upper limit; on the other hand, $v_p^L = 0$ implies that the dose is less than L_b, and obviously less than U_b too. $v_p^U = 1$ represents that the dose at point p is $\leq U_b$, but might even be smaller than L_b; whereas if v_p^U is equal to 0, this would mean that the dose at point p is larger than U_b, in the meantime larger than L_b too. A value of 0 for v_p^{LU} indicates that the dose at point p is either more than the upper limit or less than the lower limit, but if v_p^{LU} is equal to 1, then the dose at point p is within the limits set by U_b and L_b. Thus it would be desirable to have $v_p^{LU} = 1$, for this condition would mean that v_p^L and v_p^U also have a value of 1.

The second model proposed by Lee in [18] attempts to minimize a weighted sum of the deviations, by calculating the amount of deviation from the desired target at each individual point in the tumor volume. The constraints for this model are similar to those in the first model and are given in Eq. (2.3),

$$\begin{aligned} \sum_{j=1}^{n} D(\|P - X_j\|)x_j + y_p^L &\geq L_b \\ \sum_{j=1}^{n} D(\|P - X_j\|)x_j - y_p^U &\leq U_b \end{aligned} \tag{2.3}$$

where y_p^L and y_p^U are positive continuous variables that represent the deviations from the lower limit and upper limit respectively. They are used as constraints in minimizing the weighted objective function in Eq. (2.4):

$$\text{Minimize} \sum_{p} (\alpha_p y_p^L + \beta_p y_p^U) \tag{2.4}$$

Lee's work proposes using the conformity index (a ratio of total volume enclosed by the isodose surface to the target volume enclosed by the same surface) and the coverage index (ratio of target volume enclosed by the isodose surface to the total target volume) to aid the assessment of the quality of their results. Section 4.3.4 presents a comparison of the dosimetry planning results between Lee's work and the algorithm proposed by this thesis.

2.1.2 Lung Brachytherapy

As for lung brachytherapy, there has been relatively little work done on dosimetry planning. Even for the equipment used in lung brachytherapy, adaptation from the prostate brachytherapy environment is difficult not only due to limited access because

of the presence of the ribcage, but also more constraints need to be met for lung brachytherapy procedures since there are vital organs in close proximity and there is significant motion due to respiration and heart beat. Trejos *et al.* (from CSTAR) have developed devices, integrated systems and a test-bed for minimally invasive robot-assisted lung brachytherapy [48, 49, 50]. In [48], they discussed issues that affect the precision in seed deployment, such as the difficulty in the penetration of the needle to the correct destination due to obstacles as a result of anatomical structures and organs. Also the instability of the equipment while dropping the seeds might lead to seed misplacements. To account for these factors, and to reduce exposure to radiation for healthcare personnel during a brachytherapy session, the constructed device from [49] has been implemented in an integrated system along with commercially available dosimetry planning software to perform minimally invasive lung brachytherapy under the guidance of US imaging. Moreover in [50], the dosimetric results of the MIRA (Minimally Invasive Robot-Assisted) V system are assessed against various radiation parameters and the *in vitro* results obtained are acceptable.

Also, [51] reported a procedure for lung brachytherapy where ^{125}I seeds are sewn into resection margins for T1 and T2 stage lung tumors. Lung tumor staging is explained in more detail in Appendix A. In this study, the ^{125}I sutures are secured in a nonabsorbable mesh, which is then pushed through the endoscope and secured in a 'tent-like' fasion over the resection margins. This method is especially beneficial to patients with small T1 or T2 stage lung tumors who are unfit for lobectomy or pneumonectomy due to an inadequate pulmonary reserve. Experimentally, this procedure has been performed on two separate lobes in the right chest cavity of a pig with the help of the da Vinci robotic system. The seeds are sewn in place using either the 'looping' technique or the 'longitudinal' technique [51]. Reference [51] emphasizes that with the advent of robotic technology, new options for the treatment of lung

cancer, such as the one that they proposed, may improve and overcome technical difficulties of instrumental manipulations in the narrow chest cavity.

In addition to the above technique, [9] also discussed how to physically implant ^{125}I seeds to cover the volume of disease in the lung, this procedure is called volume implant. Though the results of volume implant show inferior results as compared to surgery, at least it is an option to treat patients who cannot undergo any surgical resection.

2.2 Modeling Brachytherapy Seeds

The cylindrical nature of the brachytherapy seeds induces an anisotropic dose distribution around an individual seed, forcing the correct modeling of the seeds to be an important aspect in improving the overall accuracy of LDR brachytherapy. The anisotropicity is due to extra attenuation by greater length of material on the long axis of the source, which results in a higher dose rate in the transverse axis as compared to the long axis.

A study carried out by [52] examines the dose distribution of the 6711 model of ^{125}I in 2D space indicates that at a distance r from the center of the seed, the dose varies with angle θ, which is the angle relative to the seed's long axis. The study also presentes an empirical expression that approximated the measured results, since the r-dependent dose distributions are different at different values of θ.

The dose distribution of ^{125}I in 3D space was studied by [53] using a point source distribution formula by Berger, which neglected the dose deviation from the exact dose at distances less than $0.5cm$. In this work, the radiation in 3D space has been calculated and measured, and they found that there is a 5% difference between the two results at an angle perpendicular to the seed's axis. The formula used determines

the 3D dose distribution at any point of interest with a 6% uncertainty. The work in [53] stated that a complete mathematical function describing the entire 3D space dose distribution in tissue is required if the precise 3D distribution is to be calculated.

2.3 Dose Calculation

Guidelines supplied by [5] from the American Association of Physicists in Medicine (AAPM) provided detailed information on brachytherapy seed types, isotope radioactivity, dose rate calculation and suggested clinical dose. The work described in this thesis follows the recommendations of [5] and uses $144Gy$ as the suggested 100% dose. To calculate the dose at a particular point, the dose rate formula from [5] is used. The dose rate, $\dot{D}(r)$, due to a point source at r units away is given by the formula below:

$$\dot{D}(r) = S_k \cdot \Lambda \cdot g(r) \cdot G(r, \Theta) \cdot \Phi_{an}(r) \tag{2.5}$$

In this equation, S_k is the initial activity of the source, Λ is the dose rate constant, $g(r)$ is the radial dose function in the transverse axis of the seed, $G(r, \Theta)$ is the geometry factor for the seed source, and $\Phi_{an}(r)$ is the anisotropy correction factor. The details for these parameters are given in Appendix B.

Prior to converting dose rate to dose ($D(r)$), $T_{1/2}$ of the source is required to calculate the meanlife of the radionuclide, τ,

$$\tau = \frac{T_{1/2}}{ln(2)} \tag{2.6}$$

A value of 1426 hours is used for $T_{1/2}$ as mentioned in section 1.1.1.1. From here, the

dose at any point is given by 2.7 as in [7],

$$D(r,\Theta) = \dot{D}(r,\Theta,t_0)\cdot\tau\cdot k_u \tag{2.7}$$

where k_u is a conversion factor in hours (h), and in this case, since the half-life is already expressed in h, the value of k_u is 1.

The details on the formulation of the optimization problems for dosimetry planning and dynamic dose optimization are explained in the next chapter.

Chapter 3

Optimization-based Planning Approach

This chapter starts with an overview of the proposed solution in section 3.1. Then the details on the formulation of the dosimetry planning and IDDO optimization problems are presented. In particular, an in-depth description of the dosimetry planning algorithm is given in section 3.2 while section 3.3 presents the details of the IDDO algorithm.

3.1 Proposed Solution

In order to achieve the goals stated in section 1.2, two optimization problems are formulated and solved for each of the **dosimetry planning** and **IDDO** components. In general, the optimization problems are constrained by the condition that the dose at each and every point of interest throughout the volume has to be within the imposed bounds U_b and L_b. The purpose of the governing objective function is to deliver the desired amount of dose to all points under consideration.

Different from the results of Lee's work which produced seed locations specified in discrete-space, the locations of the seeds produced by the proposed algorithms in this thesis are to be specified in continous-space, implying that there are no limitations on the final locations of the seeds so long as they are all within the volume of the tumor. The actual tumor volume is not defined in the continuous-space but has been discretized to make the problem more tractable, for a tumor volume defined in the

continuous-space would be composed of an infinite number of points, and it would not be possible to consider and satisfy all these points for dosimetry. The discretization of the tumor volume is based on the tumor shape, and since no assumption has been made regarding the shape and size of the tumor, this guarantees that the optimization problem is applicable to all tumors.

The approach undertaken in this thesis is to optimize the overall dose that would be delivered to the target tumor, in such a way that the sum of rewards would be maximized while the sum of penalties would be minimized. A reward corresponds to a point in the target volume that is feasible, i.e., satisfies the upper and lower limits of the prescribed dose; whereas a penalty corresponds to an infeasible point in the target, i.e., one that receives a dose that is more than the upper limit or less than the lower limit of the prescribed dose. Essentially, maximizing the sum of rewards is equivalent to minimizing the sum of penalties. So the objective of the optimization can be stated as either Eq. (3.1a) or Eq. (3.1b) below:

$$\text{Maximize } \Sigma(r) \mid L_b \leq D(r) \leq U_b \tag{3.1a}$$

$$\text{Minimize } \Sigma(r) \mid D(r) < L_b, \text{ or, } D(r) > U_b \tag{3.1b}$$

Here, r represents all points found in the tumor volume and $D(r)$ represents the dose present at the particular point, r.

3.2 Pre-planning Algorithm Description

This section describes the formulation of the optimization problem for dosimetry planning. The problem description is further broken down into three subsections, section 3.2.1 looks at how the problem is formulated in 3D space; section 3.2.2 explains

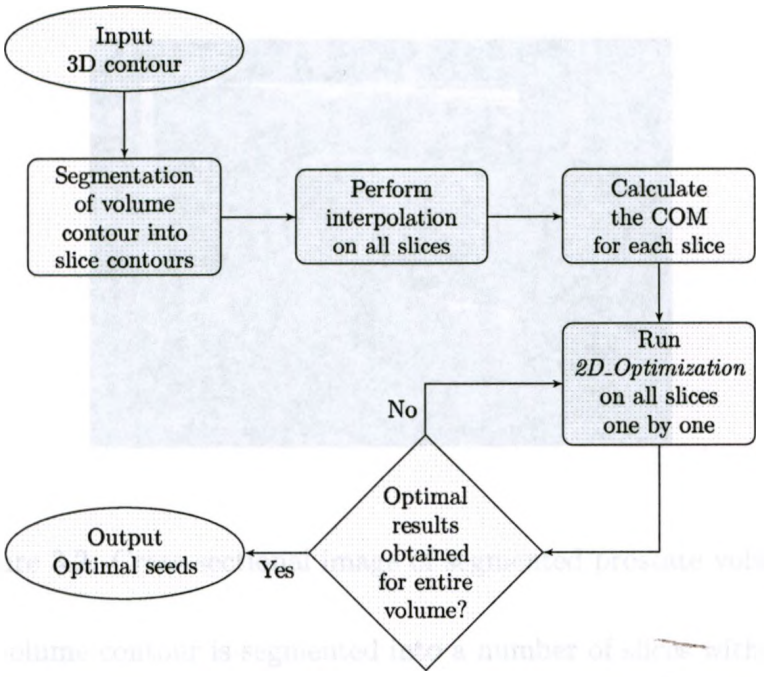

Figure 3.1: Flowchart for *3D_Optimization*

how the 3D problem is broken down into a series of 2D problems, which are then solved one by one using an optimization routine. The details of this optimization routine including the parameters involved are explained in section 3.2.3. The overall algorithm is given the name DOPAL, which stands for **DO**simetry **P**replanning **AL**gorithm.

3.2.1 Pre-planning 3D Problem Formulation

Figure 3.1 shows the basic steps involved in the *3D_Optimization* algorithm. The following will examine these steps in more detail.

The target tumor's 3D volume information is the first thing that is required to begin the pre-planning process using the proposed algorithm. Specifically, the algorithm is to be provided a collection of points that describe the contour of the volume, which trace out a mesh of the actual target as seen in 3D space. Section 4.1.2 explains how to obtain the contour of *ex vivo* tumors, which must be done manually.

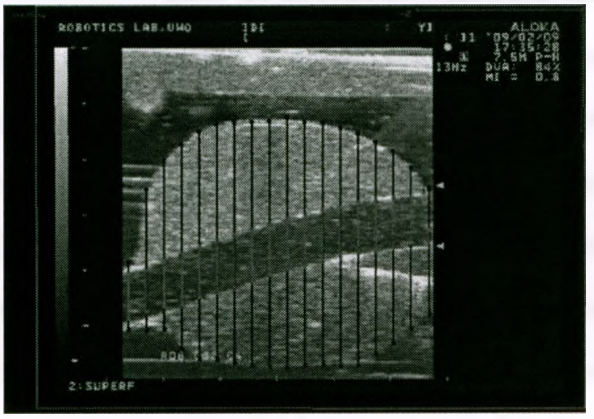

Figure 3.2: Cross-sectional image of segmented prostate volume

Then the volume contour is segmented into a number of slices with equal separation d_h between all slices. There is no strict limitation on the value chosen for d_h; however better results are generally obtained when an approximate value of $0.50cm$ or less is selected. Figure 3.2 shows a cross-sectional image of a segmented prostate volume with all the slices, the separation shown here is $0.50cm$.

Upon segmentation, the contour of each slice is to be interpolated to ensure that there is a sufficient number of points describing each slice so that a proper dose can be delivered to the entire slice. The reason for this is that the objective functions in Eq. (3.9) and Eq. (3.11) have no knowledge of the shape of the slice itself, so the objective functions are only concerned with delivering the desired dose to the shape described by the available contour points. From the algorithm's point of view the target volume appears as a collection of points instead of a shape with surfaces or edges, so a circle described by 4 points might be misinterpreted by the algorithm as a square. As a result, when the contour points appear quite sparse due to the contour being described by an insufficient number of points, the outcome of the optimization algorithm for such a contour will only deliver dose to the few contour points present, leaving behind

undosed areas in between the contour points. To prevent such misinterpretation from happening, the number of points defining the contour are interpolated to have at least 50 points. This value was chosen after numerous experimental evaluations. The same is done for all apparent contours on a slice, which may include the target region contour, as well as the forbidden contour. As in the case for a prostate tumor, there would be two contours present on every slice of the target volume, where one contour is for the prostate itself (i.e. target region contour), and the other contour is for the urethra (i.e. forbidden region contour). (A more detailed description on target and forbidden regions can be found in section 3.2.2)

After ensuring that the contours of all slices have a sufficient number of points, the Center Of Mass (COM) of each contour is calculated and provided to the optimization routine as a starting temporary seed, *temp_seed*. The coordinates of the COM for a contour with n points are calculated based on the following formula,

$$COM_x = \frac{\sum_{i=0}^{n} m_i x_i}{\sum_{i=0}^{n} m_i} \tag{3.2a}$$

$$COM_y = \frac{\sum_{i=0}^{n} m_i y_i}{\sum_{i=0}^{n} m_i} \tag{3.2b}$$

where m_i is the mass of point i and x_i and y_i are the x and y coordinates of point i respectively. In using the above formulas, each contour is assumed to have a uniform weight distribution, which implies that the value of m_i is 1 for each coordinate.

Prior to invoking the DOPAL algorithm, the user is required to select values for U_b

and L_b. In the case of a prostate tumor, the user may specify U_b and L_b values for the target volume as 150% and 100% of the prescribed dose respectively; whereas for the urethra, the U_b and L_b values may be specified as 120% and 100% of the prescribed dose [47]. For this reason, the values for U_b and L_b were not hard-coded, to provide flexibility for the different values they may take as required by different types of tumor. These user-specified U_b and L_b values, along with the contour information of the 3D volume, as well as the contour information of the 2D slice of interest, are used as inputs to formulate the 2D optimization problem. The resulting output is a set of optimal seeds located on the current slice of interest.

A 2D optimization problem must be formulated for every slice from the current target volume, and the resulting volume-wise optimal seeds (*DOPAL_2Dseeds*) from each particular slice are stored and the corresponding volume-wise violation amount is calculated accordingly. A violation occurs when the dose delivered to point i, $D(i)$, is greater than the accepted upper limited ($D(i) > U_b$) which corresponds to an overdose, or less than the accepted lower limit ($D(i) < L_b$) which corresponds to an underdose. The violation amount (*vio_amt*) is defined below as the summation of the amount of overdose (*overdose_amt*) and underdose (*underdose_amt*), taken from each and all contour points. Thus for a volume with n slices, where each slice is defined by, say 50 contour points, *overdose_amt*, *underdose_amt* and *vio_amt* are given by:

$$\begin{aligned} underdose\_amt &= \sum_{k=0}^{n}(\sum_{i=0}^{50}[L_b - D(i)]) \text{ for } D(i) < L_b \\ overdose\_amt &= \sum_{k=0}^{n}(\sum_{i=0}^{50}[D(i) - U_b]) \text{ for } D(i) > U_b \\ vio\_amt &= underdose\_amt + overdose\_amt \end{aligned} \tag{3.3}$$

This volume-wise slice-by-slice optimization is repeated in this manner until no

further change is seen, at which time the output have converged to a solution. Even in the case when the solution does not converge, this algorithm is still terminated after a maximum number of iterations denoted by a value that is set by the user prior to executing the algorithm.

3.2.2 Pre-planning 2D Problem Formulation

This section of the algorithm is invoked for every slice contour that is a segment of the tumor volume, the goal here is to add more seeds to the slice of interest if it helps to provide a better dosimetry plan overall. Figure 3.3 illustrates the steps involved in the algorithm, which are discussed below in detail.

In some cases it appears better to leave the slice void of any seeds. As such, each slice invokes the optimization routine with no seeds present on this particular slice, but instead provides the seeds found on all other slices, which is referred to as *seeds_other_slices*. Based on *seeds_other_slices*, a *vio_amt* is calculated and stored so that it can be compared later against the new *vio_amt* due to *new_DOPAL_seeds*. *new_DOPAL_seeds* is a matrix containing the set of seeds from the previous execution of the optimization routine, plus one new entry of 'modified *temp_seed*'. The values of the 'modified *temp_seed*' and the reason for this modification are explained shortly.

When this algorithm (*2D_Optimization*) is executed, it assumes that other than the current slice of interest, there are seeds on all other slices throughout the volume. However on the first call of *2D_Optimization* of the 1^{st} slice, this would not be the case since the entire volume would be empty of seeds. Nevertheless, the algorithm starts with the assumption that every contour point of the slice is either underdosed or overdosed, thus the total number of violation points of the current slice, which is defined as *min_vio*, is assigned a value that is equal to the total number of contour

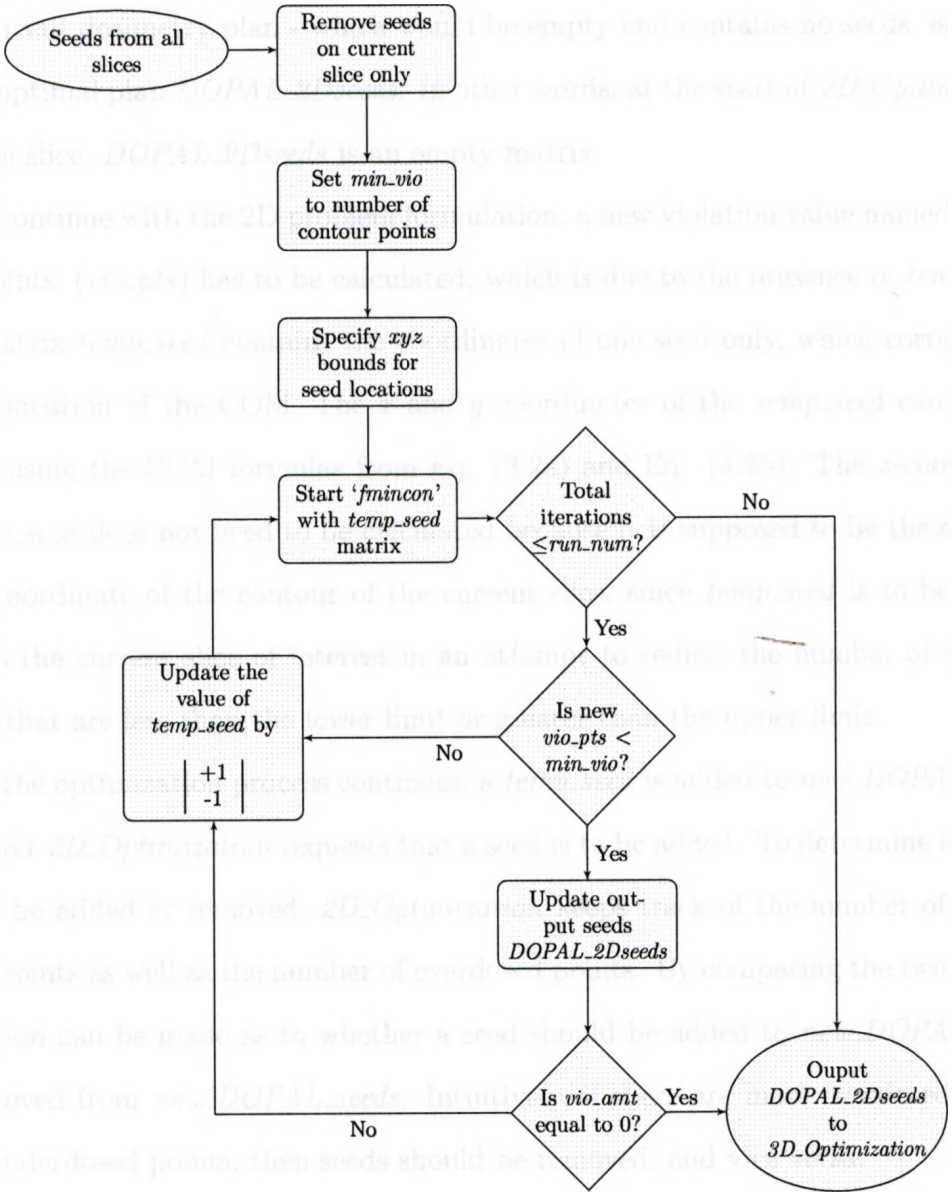

Figure 3.3: Flowchart for *2D_Optimization*

points on the current slice. For instance, a slice contour having a total of 50 points would imply an initial number of 50 violation points, as in Eq. (3.4):

$$min\_vio = 50 \tag{3.4}$$

The current dosimetry plan - which would be empty and contains no seeds, is stored as the optimal plan *DOPAL_2Dseeds*. In other words, at the start of *2D_Optimization* for each slice, *DOPAL_2Dseeds* is an empty matrix.

To continue with the 2D problem formulation, a new violation value named 'violation points' (*vio_pts*) has to be calculated, which is due to the presence of *temp_seed*. The matrix *temp_seed* contains the coordinates of one seed only, which corresponds to the location of the COM. The x and y coordinates of the *temp_seed* can be obtained using the COM formulas from Eq. (3.2a) and Eq. (3.2b). The z-coordinate of *temp_seed* does not need to be calculated because it is supposed to be the same as the z-coordinate of the contour of the current slice, since *temp_seed* is to be added only to the current slice of interest in an attempt to reduce the number of contour points that are less than the lower limit or greater than the upper limit.

As the optimization process continues, a *temp_seed* is added to *new_DOPAL_seeds* whenever *2D_Optimization* requests that a seed is to be added. To determine if a seed should be added or removed, *2D_Optimization* keeps track of the number of underdosed points as well as the number of overdosed points. By comparing the two values, a decision can be made as to whether a seed should be added to *new_DOPAL_seeds* or removed from *new_DOPAL_seeds*. Intuitively, if there are more overdosed points than underdosed points, then seeds should be removed, and vice versa.

If seed removal is required, then a random seed is removed from *new_DOPAL_seeds*. If *new_DOPAL_seeds* is already empty, meaning that any seed addition would only cause more overdose, then *DOPAL_2Dseeds* is sent back to *3D_Optimization* as an empty matrix and *3D_Optimization* moves onto the next slice in the volume.

The calculation of *vio_pts* takes into account the effects of seeds from all slices in the volume, including the seeds from the current slice of interest, and tracks the total

number of contour points that are overdosed ($> U_b$) or underdosed ($< L_b$).

$$vio\_pts = \sum(i)$$
$$\text{such that} \tag{3.5}$$
$$Dose(i) > U_b, \text{ or } Dose(i) < L_b$$

vio_pts is calculated on each run of the optimization routine, and if this new violation is strictly less than the initial *min_vio* amount, meaning that one or more contour points are now dosed properly, then *min_vio* is overwritten by *vio_pts* and *DOPAL_2Dseeds* is updated to the values of *new_DOPAL_seeds*. In the event that *new_DOPAL_seeds* does not reduce the total number of violation points, neither *min_vio* nor *DOPAL_2Dseeds* gets modified.

The most desirable outcome is having *vio_pts* equal to 0, which means that the value of the objective function of the minimization optimization routine is at its absolute minimum or is equal to zero, and that each and every contour point i is within the desirable range of the accepted dose such that,

$$\forall i, L_b \leq Dose(i) \leq U_b \tag{3.6}$$

When this happens, the optimization process is terminated and the most recent *new_DOPAL_seeds* replaces *DOPAL_2Dseeds*, and is sent back to the *3D_Optimization* algorithm for the 3D problem from the previous section.

It is possible that a target contour may never receive a perfect dose to all its points, implying that the value of the objective function may never reach an absolute minimum, therefore it is necessary to make sure that the optimization does not get stuck in a loop by using a counter variable named *run_num*. The optimization

process is allowed to iterate for a total of 18 times, a number which has been verified experimentally as being sufficiently large to produce satisfactory results. If the number of iterations exceeds *run_num*, meaning that the optimization process has not produced a dosimetry plan with a lower *vio_pts* than the current *min_vio*, the process is terminated and the currently stored *DOPAL_2Dseeds* (which may or may not be the most recent result but is the result that produced the lowest *vio_pts*) is returned to *3D_Optimization* as the output of the optimization.

Care must be exercised in storing and updating the values in *new_DOPAL_seeds*. For instance, if *new_DOPAL_seeds* consists of only 1 seed, (which was taken from *temp_seed*) and is placed outside of the target volume, the seed is deemed unusable and would get removed, therefore making the *DOPAL_2Dseeds* variable empty. On the next consecutive iteration of *2D_Optimization*, the same *temp_seed* is again added to and then removed from *new_DOPAL_seeds*, thus forcing the algorithm in to an infinite loop. The same scenario may also occur if the latest addition to *new_DOPAL_seeds* always produces a local minimum as a solution to the optimization problem, forcing all new seed additions to that particular solution. To prevent the above from happening, *temp_seed* is modified prior to every iteration by $+1$ in the x direction and -1 in the y direciton. By doing this, the latest addition to *new_DOPAL_seeds* is different from the one that was added in the previous iteration. Using different initial seed locations on every iteration prevents the optimization routine from producing similar solutions, especially if the one produced is not valid. Also, using all different values of *temp_seed* in *new_DOPAL_seeds* allows maximum exploration of the entire seed domain.

The boundary of this domain is the boundary of the solution to this optimization problem, and is essentially denoted by the bounds for the location of all potential seeds. The z-direction bound for a seed is restricted to the value of the z-coordinate of the contour of the current slice, in the same way that the z-coordinate of *temp_seed*

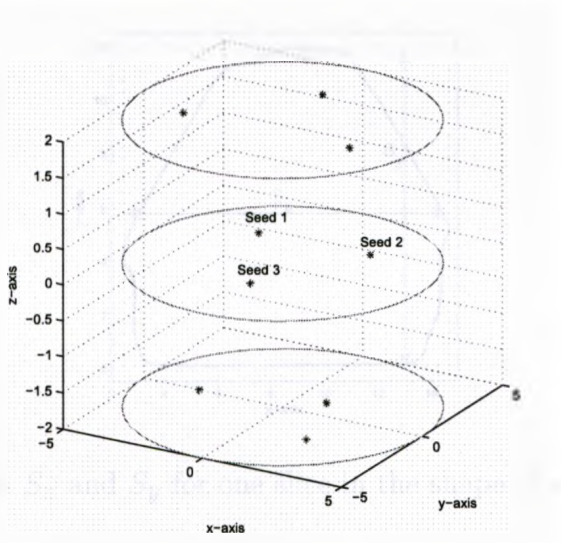

Figure 3.4: Figure illustrating 3 seeds having identical z-coordinate values

was restricted as well. In other words, the result of running the optimization routine on every slice produces a set of seeds that have identical z-coordinate values, because they are all on the same slice. As a result, bounds only have to be specified in the x and y directions to control the location of the seeds.

Figure 3.4 shows a volume with 3 slices where there are 3 seeds on each slice. Assume that seeds S_1, S_2 and S_3 (Seed 1, Seed 2 and Seed 3 in Fig. 3.4) are the elements of *DOPAL_2Dseeds* (which is the output of *2D_Optimization*). It is clear that the values of the x and y coordinates for all 3 seeds are different but the z-coordinate value for all three seeds are identical. Furthermore, the seeds from *2D_Optimization* are required to fall inside the target contour defined by the x and y coordinate values of the contour, because it makes no sense for a seed to be deposited outside of the tumor volume.

The bounds for each slice can be approximated by a rectangular region, since the contour of a slice is assumed to be in the shape of a random polygon. The respective

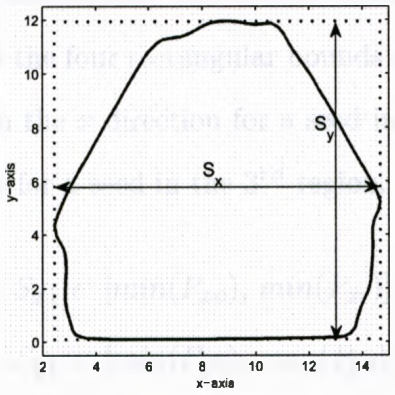

Figure 3.5: Bounds S_x and S_y for one slice in the shape of a random polygon

bounds S_x and S_y in the x and y directions are given as follows,

$$\begin{aligned} S_x &\in [min(P_x),\, max(P_x)] \\ S_y &\in [min(P_y),\, max(P_y)] \end{aligned} \tag{3.7}$$

where P_x and P_y are the collection of the x and y coordinates of the points that describe the slice contour. In Fig. 3.5, the contour is described by P_x and P_y, and S_x and S_y form the rectangular bound that defines the potential location of all seeds on this slice. As can be seen from this figure, the bounds are not the exact shape of the contour and include space outside of the contour that are not usable as seed locations. For this reason, the location of each seed still needs to be verified to make sure that it is in fact inside the contour.

For a target contour that encloses a forbidden contour, e.g., a slice from the prostate tumor volume, the single rectangular bound from Fig. 3.5 is then further divided up into four smaller rectangular bounds, which is illustrated by Fig. 3.6. In Fig. 3.6(c), the 4 smaller rectangular bounds are overlaid on top of the planar view of a simplified prostate contour in the shape of a donut, where the inside circle

is a representation of the urethra and the outside circle is a representation of the prostate. The equations for the four rectangular bounds are given in Eq. (3.8), where S_{x1} indicates the bounds in the x direction for a seed in the 1^{st} region; likewise S_{y3} indicates the y-axis bounds for a seed in the 3^{rd} region.

$$\begin{aligned}
S_{x1} &\in [min(P_{xo}),\ min(P_{xi})] \\
S_{y1} &\in [min(P_{yo}),\ max(P_{yo})] \\
S_{x2} &\in [min(P_{xo}),\ max(P_{xo})] \\
S_{y2} &\in [max(P_{yi}),\ max(P_{yo})] \\
S_{x3} &\in [max(P_{xi}),\ max(P_{xo})] \\
S_{y3} &\in [min(P_{yo}),\ max(P_{yo})] \\
S_{x4} &\in [min(P_{xo}),\ max(P_{xo})] \\
S_{y4} &\in [min(P_{yo}),\ min(P_{yi})]
\end{aligned} \tag{3.8}$$

In Eq. (3.8), P_{xo} and P_{yo} are the respective values of the x and y-coordinate that describe the outside contour, which corresponds to the target region; while P_{xi} and P_{yi} are the respective values of the x and y-coordinate that describe the inside contour, which corresponds to the forbidden region. The essence in employing this approach is to try and avoid placing seeds in or near the forbidden contour. Evident in Fig. 3.6(c), the four rectangular bounds combine together to cover up the majority of the target region, but cover no part of the forbidden region at all. When these bounds are used to control the placement of a new seed, the forbidden region is effectively avoided.

One drawback here is that there is a certain amount of space included in the bounds that in fact belong to neither the target region nor the forbidden region. To account for this inclusion of unusable space, the location of each of the optimized

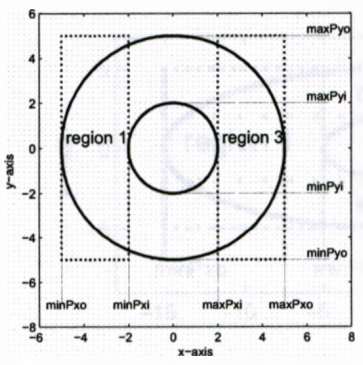

(a) Bounds for regions 1 and 3

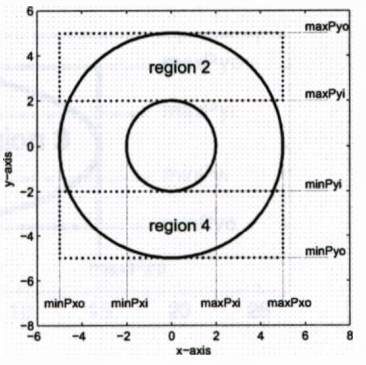

(b) Bounds for regions 2 and 4

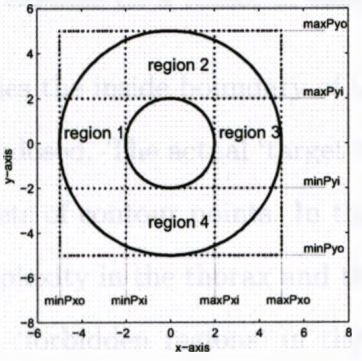

(c) All four bounds overlaid on top of simplified prostate contour

Figure 3.6: Boundaries of the 4 regions for seed placement

entries in *new_DOPAL_seeds* must be verified to ensure that none of the seeds are outside of the target. If a seed has been found to lie outside of the target region, i.e. outside of the contour itself, it is removed from the *new_DOPAL_seeds* matrix and the value of *temp_seed* is modified like previously mentioned. So that when *temp_seed* is added to *new_DOAPL_seeds* on the next iteration, the new optimizatoin based on the updated *new_DOPAL_seeds* will not run into the same problem.

These bounds are especially useful in dosimetry planning for prostate cancer, where it is crucial to try and avoid delivering dose to the urethra, which runs through the center of the prostate. The urethra thus becomes the 'forbidden region', and the

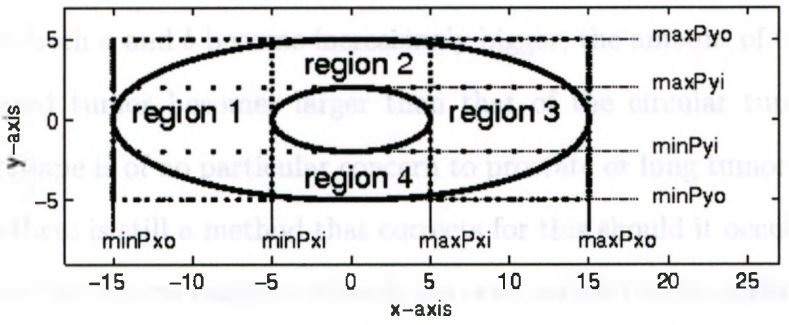

Figure 3.7: Bounds on a tumor of elongated shape

surface of the urethra becomes the inside boundary of the 'target region' so it would get protected from being overdosed. The actual 'target volume' of the prostate tumor is therefore defined by two sets of contour points. In the case of the lung, because of the significantly greater complexity in the thorax and the current state of the robotic lung brachytherapy project, 'forbidden regions' in the lung (which could be quite complex) were not considered in this initial study. This problem will be addressed in depth in a more detailed study in the future.

When the method mentioned above is applied to a tumor that is more elongated than usual, the portion of the tumor covered by the bounds is shown in Fig. 3.7. It can be seen from this figure that there is also a certain amount of unusable space being covered by the bounds. The surface area of an ellipse with a major axis of radius, a, and a minor axis of radius, b, is given by

$$\text{SA of Ellipse} = \pi \cdot a \cdot b$$

while the overall surface area of the bounds can be calculated as $2a \times 2b$. Ignoring the bounds around the forbidden region, the unusable space around the target region is $4ab - \pi ab = ab(4 - \pi)$. The unusable space around the target region for a regular

circular shape with radius r is, $4r^2 - \pi r^2 = r^2(4 - \pi)$. It can be shown from the above that as both a and b become increasingly bigger, the amount of unusable space in an elongated tumor becomes larger than that of the circular tumor. Such an exaggerated shape is of no particular concern to prostate or lung tumors at this time; nevertheless there is still a method that corrects for this should it occur. The trick is to break down the four rectangular bounds into ever smaller rectangular bounds. The smaller the bounds are, the more accurately they approximate the actual elongated shape. The disadvantage in employing such an approach is that there are more computations required to figure out the exact parameters that define these smaller bounds. Though, the improved accuracy in the resulting dosimetry plan may be worth the effort. In addition, this correcting method would also improve the accuracy of the shape-approximation for a general circular tumor too.

Once all the parameters have been obtained, i.e., contour information of the current slice, contour information of the present volume which is composed of all slices from the 1^{st} to the current slice, the set of temporary seeds to be optimized, U_b and L_b values, as well as the xyz bounds for potential seed locations, the optimization routine '*fmincon*' is ready to be invoked to solve the problem at hand.

3.2.3 Pre-planning's '*fmincon*'

'*fmincon*' is the constrained minimization routine from MATLAB's optimization toolbox. This particular routine was selected because it offers the option to minimize the objective function subject to a set of constraints. Figure 3.8 is an illustration of how '*fmincon*' has been used by *2D_Optimization* to solve the dosimetry planning problem.

The objective function requires the following parameters as its input,

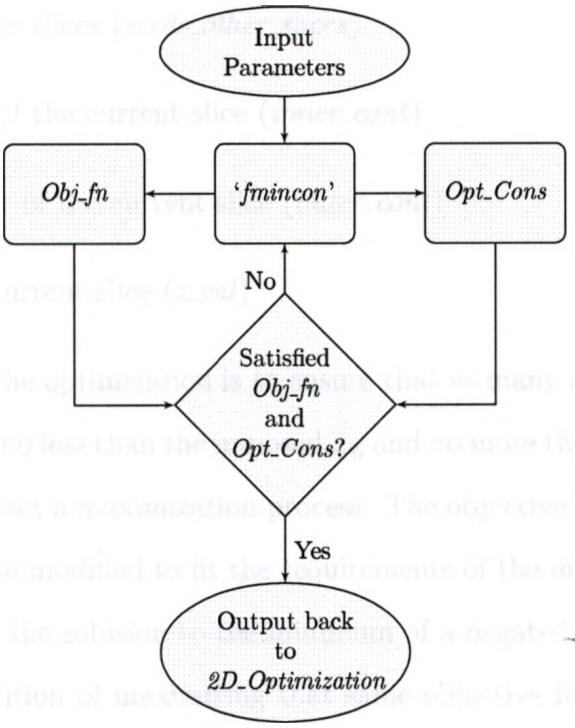

Figure 3.8: Flowchart for '*fmincon*'

- Current slice seeds (*cur_seeds*), which is equivalent to *new_DOPAL_seeds*
- Seeds from other slices (*seeds_other_slices*)
- Volume contour (*vol_contour*), which is made up of all slices prior to and including the current slice
- U_b and L_b
- Desired % dose (*desd_goal*)
- z value of the current slice (*z_val*)

As for the optimization constraint, the required input parameters are as follows,

- Current slice seeds (*cur_seeds*), which is equivalent to *new_DOPAL_seeds*

- Seeds form other slices (*seeds_other_slices*)
- Inside contour of the current slice (*inner_cont*)
- Outside contour of the current slice (*outer_cont*)
- z value of the current slice (*z_val*)

The objective of the optimization is to ensure that as many contour points would receive a dose that is no less than the imposed L_b and no more than the imposed U_b as possible, which is in fact a maximization process. The objective function (*Obj_fn*) for maximization must be modified to fit the requirements of the minimization routine - *fmincon*. Essentially, the solution to the minimum of a negated objective function is equivalent to the solution of maximizing that same objective function. In any case, the objective function is mathematically stated below:

$$\sum(i), \ | \ \forall i, \ i \ \epsilon \ (\bar{P}_x, \bar{P}_y), \text{ where } L_b \leq D(i) \leq U_b \tag{3.9}$$

where $D(i)$ is the total amount of dose present at point i. Since '*fmincon*' is invoked by *2D_Optimization* for every slice of the contour volume, and because *2D_Optimization* is an iterative process where each successive optimization includes the contours from all previous iterations, then $\bar{P}_x$ and $\bar{P}_y$ are coordinates that describe the volume which is made up of all slices from the 1^{st} slice to the current slice. In words, Eq. (3.9) states that for the contour described by $\bar{P}_x$ and $\bar{P}_y$ (which is the collection of points from the first point on the first contour slice to the last point on the current contour slice), the dose at every point i is desired to be $\geq L_b$ and $\leq U_b$ at the same time. References [18, 54] stated that the total dose at a particular contour point can be approximated as the summation of dose from all available seeds. Mathematically, the

approximation of the dose at point P_0 can be expressed as:

$$\sum_{i=0}^{n} D(\|P_0 - \bar{S}_i\|) \tag{3.10}$$

In this equation, $D(r)$ denotes the dose contribution of a seed to a point at a distance of r units, $\|\cdot\|$ denotes the Euclidean norm, and $\bar{S}_i$ is the vector of the coordinates of seed i of a total of n seeds. Equation (3.10) says that, the total dose apparent at point P_0 is the summation due to the dose from each of the seeds from $\bar{S}_0$ to $\bar{S}_n$. The dose of each seed, as stated in [18, 54], is based on the Euclidean distance between the point of interest (P_0) and the location of the seed ($\bar{S}_i$), where the seed itself can be approximated as a point source. Specific to the work in this thesis, the irradiation of a single seed is approximated using the point source formula provided by [5], which was given in Eq. (2.5).

In the objective function stated in Eq. (3.9), the total amount of dose, $D(i)$, at each point is calculated using Eq. (3.10). So the total dose is the summation of dose contributions from all seeds in the volume, essentially this is the summation of the dose contributions from *seeds_other_slices*, and the dose contributions from *cur_seeds*. Therefore, even though the dose calculation is performed in a 2D setting, it still takes into consideration the dose contributions within the 3D volume.

It is worthwhile to note here that *vol_contour* was divided up into the outside volume contour (*outer_cont*) representing the target volume, and the inside volume contour (*inner_cont*) representing the forbidden volume. Should there be no need for a forbidden region (such is the case of lung tumors at the current stage), then *inner_cont* is an empty matrix that does not affect the outcome of the optimization. U_b and L_b values may be specified differently for each set of contour, thus effectively controlling the amount of dose that can be delivered to different volumes.

Furthermore, the objective function attempts to minimize the total dose deviation at all points on the contour from *desd_goal* (which may be 100% of the prescribed dose), using a least squares method, the mathematical expression is given below:

$$\text{Minimize } \{\sum_i [D(i) - desd\_goal]^2\}, \text{ where } i \in (\bar{P}_x, \bar{P}_y) \tag{3.11}$$

Here, *desd_goal* may be set to different values for the target and the forbidden volumes to achieve the respective desired dose.

The exact value of the desired dose at point j, $D(j)$, is specified by the optimization constraints (*Opt_Cons*), given below:

$$\begin{gathered} \forall j \in [0, n] \\ D(j) = \text{Desired \% Dose} \end{gathered} \tag{3.12}$$

Different to the objective function, the optimization constraints are applied to the current slice only, where n can be interpreted as 50 to represent the number of points defining the contour of a slice. Then, Eq. (3.12) states that for all points on the current contour, the intention is to deliver the desired amount of dose to each and every one of them. The only complication here is that constraints for the inside and outside contours need to be specified separately, because the urethra (e.g. forbidden region) and the prostate (e.g. target region) have different dose bounds [47]. To maximize the amount of prescribed dose delivered to the target region, the algorithm in [47] incorporates a conformity index on the target region. To achieve the same goal, the algorithm proposed in this thesis simply specifies a different *desd_goal* for each of the inside and outside contours. For simplicity, the variable *desd_goal* for all the slice contours in the target region are given identical values. Similarly, the same value of *desd_goal* is used for all slices of the forbidden region.

One possible, although invalid, solution to the optimization problem is having multiple sources at the exact same location to achieve the desired overall coverage of the entire tumor volume. This was mentioned before in the previous section and the prevention method was to use a modified *temp_seed* value for each entry in *new_DOPAL_seeds*. Another constraint (Eq. (3.13)) is used to control the spacing between adjacent seeds and to further emphasize the importance in preventing this undesirable outcome. Even though a solution consisting of say 10 seeds at the exact same location can still produce a complete coverage to the entire tumor volume, in which the seeds assume a point source approximation, it is physically impossible to place multiple seeds at the exact same location due to the actual size and shape of the brachytherapy seeds. Thence, the equation below is used to specify the minimum allowable distance k between two adjacent seeds,

$$\|S_{i+1} - S_i\| \geq k, \text{ for } S_i \in \bar{S_{xy}} \tag{3.13}$$

where S_i and S_{i+1} are available seeds in the matrix $\bar{S_{xy}}$ and $\|\cdot\|$ is the Euclidean norm. Equation (3.13) basically says that for all neighboring seeds on the same slice, the minimum separation between any two seeds must be more than k units.

The results obtained from '*fmincon*' is sent back to the *2D_Optimization* algorithm where the seed locations are checked and verified again to make sure that all seeds are inside the target region but outside the forbidden region if applicable. The algorithm then returns to the start of the *3D_Optimization* algorithm and once again the number of violation points is checked and the above procedure is repeated until covergence is obtained.

The solution is said to have converged if there are 0 *vio_pts* in the volume, implying that each and every contour point is within the accepted upper and lower limits

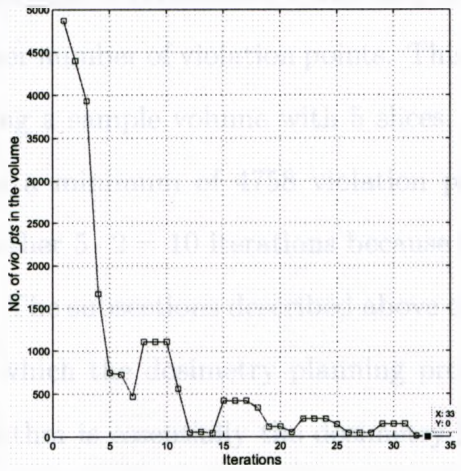

(a) Iteration vs. *vio_pts* graph of a convergent solution

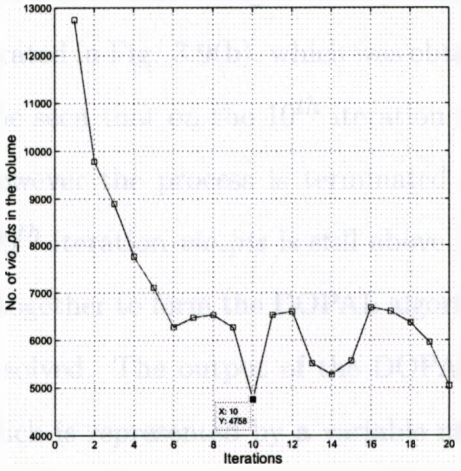

(b) Iteration vs. *vio_pts* graph of a non-convergent solution

Figure 3.9: Graphs showing convergent and non-convergent solutions of DOPAL

of the prescribed dose, at which time both *2D_Optimization* and *3D_Optimization* algorithms are terminated immediately because an optimal solution is found (Fig. 3.9(a)).

In the case when convergence is not achieved, two conditions are in place to make sure that a most optimal solution is produced and that the algorithms do not run indefinitely. The first condition is that the user can specify the maximum number of times the *3D_Optimization* algorithm should iterate, so that the total number of executions of the *3D_Optimization* algorithm cannot be more than this value regardless of whether the solution converged or not. The second termination condition deals with the case when a sub-optimal solution is found for a problem where the globally-optimal solution may not even exist. To do this, for a volume that has n slices, when a seed configuration has been found that produces a minimum number of violation points (not necessarily 0), the *3D_Optimization* algorithm is allowed to iterate for an extra $n \cdot 2$ number of times. During this time, the *3D_Optimization*

algorithm is terminated if and only if none of the new seed configurations produces a lower number of violation points. This is illustrated in Fig. 3.9(b), which was obtained using a sample volume with 5 slices. It can be seen that on the 10^{th} iteration there was a minimum of 4758 violation points, however the process is terminated after another $5 \cdot 2 = 10$ iterations because by the 20^{th} iteration *vio_pts* is still above 5000.

The subsections described above combine together to form the DOPAL algorithm, in which the dosimetry planning problem is solved. The output of the DOPAL algorithm is essentially the dosimetry plan, which is represented by a variable named *DOPAL_3Dseeds*.

3.3 IDDO Algorithm Description

This section gives an in-depth description of the IDDO algorithm. The details on the formulation and solving of the IDDO problem are given in section 3.3.1. Section 3.3.2 provides the details of the optimization routine employed by the IDDO algorithm. Figure 3.10 explains the details of this algorithm.

3.3.1 IDDO Problem Formulation

Similar to DOPAL, IDDO also requires the contour information of the tumor volume to start with. Unlike DOPAL however, (in which *vol_contour* was made up of all slices up to and including the particular slice of interest), IDDO deals with the entire tumor volume all at once to achieve a volume-wise optimal seed compensation. Therefore, the volume contour information provided to IDDO does not have to be segmented. Even so, the same segmented volume from DOPAL are currently used for simplicity purposes. As inputs, the IDDO algorithm requires a set of seeds from pre-planning (*preplan_seeds*) as well as a set of currently deposited seeds (*cur_dep_seeds*). Using

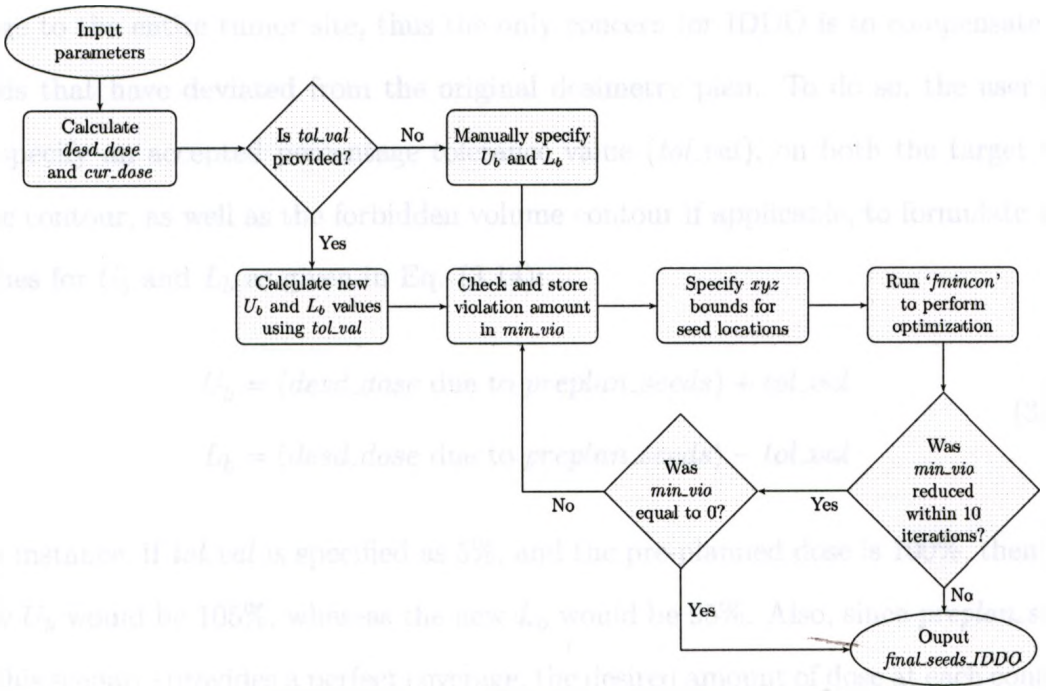

Figure 3.10: Flowchart for IDDO

these two sets of seeds, IDDO can then calculate the desired dose (*desd_dose*) due to *preplan_seeds*, also the actual dose (*cur_dose*) due to *cur_dep_seeds*. These values are required to achieve the goal of the IDDO algorithm, which is to compensate for any cold spots (underdosed target volumes) or hot spots (overdosed target volumes) caused by seed misplacements.

Additional seeds can be added for any cold spots; however seeds cannot be removed to compensate for any existing hot spots. Thus the optimal plan devised by IDDO is one where the overall sum of overdose and underdose is kept to a minimum. It is worthwhile to note here that the IDDO algorithm is designed not only for use with the DOPAL algorithm, but also as a stand-alone algorithm by itself, provided that it is given *vol_contour*, *preplan_seeds* and *cur_dep_seeds*. Either way, there are two scenarios that need to be taken into consideration.

The first scenario is that the dosimetry from *preplan_seeds* provides perfect cov-

erage to the entire tumor site, thus the only concern for IDDO is to compensate for seeds that have deviated from the original dosimetry plan. To do so, the user has to specify an accepted percentage tolerance value (*tol_val*), on both the target volume contour, as well as the forbidden volume contour if applicable, to formulate new values for U_b and L_b as given in Eq. (3.14):

$$\begin{aligned} U_b &= (\textit{desd\_dose} \text{ due to } \textit{preplan\_seeds}) + \textit{tol\_val} \\ L_b &= (\textit{desd\_dose} \text{ due to } \textit{preplan\_seeds}) - \textit{tol\_val} \end{aligned} \tag{3.14}$$

For instance, if *tol_val* is specified as 5%, and the pre-planned dose is 100%, then the new U_b would be 105%, whereas the new L_b would be 95%. Also, since *preplan_seeds* in this scenario provides a perfect coverage, the desired amount of dose at each contour point *desd_dose* is thereby equal to the dose due to *preplan_seeds*.

The second scenario deals with an imperfect dosimetry due to *preplan_seeds*. In which case, the result of IDDO must be an improvement from the dosimetry of *preplan_seeds*. To put the second scenario in another way, the pre-planned seeds provided to IDDO are incapable of delivering the desired dose to all regions of the target volume, thus it is insufficient for IDDO to only compensate for seed deviations from *preplan_seeds*, since this is still not enough to produce a complete coverage to the entire target volume. IDDO in this case should know the actual desired U_b and L_b values imposed on the target volume, so that in addition to compensating for any seed deviations from *preplan_seeds*, IDDO may also take the liberty to add extra seeds in an attempt to compensate for the cold spots from the original dosimetry. In this scenario, there are no values specified for *tol_val*, rather the desired U_b and L_b values must be specified manually, for instance at 120% and 100%. In addition, the determination of *desd_dose* at each contour point can no longer be based on *preplan_seeds*,

which means that the desired dose for both the target and forbidden contours are no longer equal to the dose from *preplan_seeds*, instead they must be specified manually like it has been done in DOPAL using Eq. (3.13).

In any case, based on *desd_dose* and *cur_dose*, the required dose (*req_dose*) at each of the contour points throughout the volume can be calculated. *req_dose* is really the amount of dose that must be delivered to each contour point to produce a full coverage to the entire target volume. The values in *req_dose* are going to be different to each other, in contrast to *desd_goal* for the DOPAL algorithm, which were all identical to each other. This is because *req_dose* is the difference between *desd_dose* and *cur_dose*, as shown in Eq. (3.15), where values for *cur_dose* for instance, are likely to be 46.35% as a result of *cur_dep_seeds*, as compared to say exactly 100% for *desd_goal* from DOPAL.

$$req\_dose = desd\_dose - cur\_dose \tag{3.15}$$

The next step in the algorithm is to check for the amount of violation currently present, based on *cur_dose* and the new U_b and L_b. Similar to how it was done in DOPAL, this volume wise violation amount is stored and referred to as *min_vioamt_IDDO*. As new seed locations (*new_seeds_IDDO*) are generated by the optimization routine, its corresponding volume wise violation amount *cur_vioamt_IDDO* is calculated and compared to the currently stored *min_vioamt_IDDO*. The value of *min_vioamt_IDDO* will get overwritten by *cur_vioamt_IDDO* if and only if IDDO produces a plan with better dose coverage and less violations.

It is worth noting here that the user is also given the option to choose whether the amount of violation should take into account the total number of seeds to be used. If the user chooses not to include the weight of the seeds, this means that the calculated

cur_vioamt_IDDO is equal to the absolute violation only, which is the summation of the amount of overdose and underdose throughout the volume; otherwise 70% of the violation will come from the amount of overdose or underdose throughout the volume, whilst the remaining 30% comes from the total number of seeds that are implanted. These percentage values at this stage are completely experimental and do not reflect the actual effort in implanting an extra seed in to the tumor site. For now, the absolute violation option has been employed, which means that the number of implanted seeds plays no role in the calculation of the overal amount of violation.

$$\begin{aligned}
TopNW &= min(\bar{P}_x) \cap max(\bar{P}_y) \cap max(\bar{P}_z) \\
TopNE &= max(\bar{P}_x) \cap max(\bar{P}_y) \cap max(\bar{P}_z) \\
TopSW &= min(\bar{P}_x) \cap min(\bar{P}_y) \cap max(\bar{P}_z) \\
TopSE &= max(\bar{P}_x) \cap min(\bar{P}_y) \cap max(\bar{P}_z) \\
BotNW &= min(\bar{P}_x) \cap max(\bar{P}_y) \cap min(\bar{P}_z) \\
BotNE &= max(\bar{P}_x) \cap max(\bar{P}_y) \cap min(\bar{P}_z) \\
BotSW &= min(\bar{P}_x) \cap min(\bar{P}_y) \cap min(\bar{P}_z) \\
BotSE &= max(\bar{P}_x) \cap min(\bar{P}_y) \cap min(\bar{P}_z)
\end{aligned} \tag{3.16}$$

Next, the x and y bounds for the potential locations of the seeds must be specified. The placement of seeds in IDDO is different to the placement of seeds in DOPAL, where seeds were placed only on the current slice of interest. In IDDO, the algorithm has been designed to facilitate seed placement at any location throughout the volume. This freedom in placing a seed anywhere in the volume is only made available with the brachytherapy set-up at CSTAR (a more detailed description can be found in section 4.1.1.2), which allows seed deposition at any arbitrary location due to the

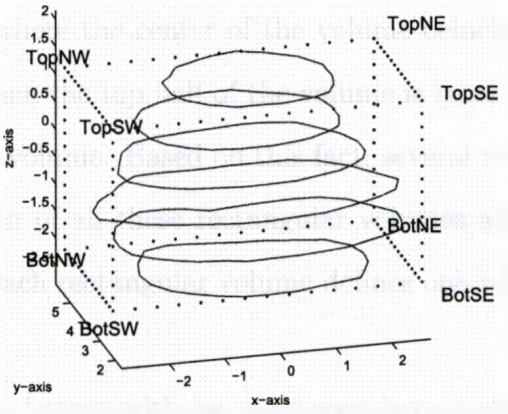

Figure 3.11: Bounding volume for seed locations for the IDDO algorithm

absence of a template grid. To this end, the IDDO algorithm has to specify bounds for the seeds in all three (XY, XZ and YZ) planes. As such, a rectangular volume is created based on the minimum and maximum values of the 3D coordinates of the volume contour. The eight corners defining the bounding volume are given in Eq. (3.16).

This bounding volume encloses the entire target volume, as well as some space exterior to it (Fig. 3.11). As a result, a verification process has to be run on the actual location of the seeds after every optimization call to make sure that the seed has actually fallen inside the target volume and not outside of it. In Eq. (3.16), $TopNW$ represents the north-west corner of the top of the volume, while $BotSE$ represents the south-east corner at the bottom of the volume. $\bar{P}_x$, $\bar{P}_y$ and $\bar{P}_z$ are the collection of x, y and z coordinates of the contours from all slices. The volume contour shown in Fig. 3.11 is the actual contour of a sample lung tumor made specifically for this project, and the dotted lines represent the bounding volume.

For a more regular 3D volume (such as a sphere), a more elegant and efficient algorithm was devised to define the boundaries of the potential locations of the seeds.

This algorithm makes use of the fact that if the spherical volume was placed on the xyz coordinate system, where the center of the volume coincided with the center of the coordinate system, then the top half of the volume is more or less a mirror-image of the bottom half of the volume. Based on this fact, several rectangular volumes are created. The combination of all these rectangular volumes approximate the overall spherical volume where each rectangular volume defines one volumetric space for the placement of the seeds.

This algorithm works better with an even mumber of slices, though it is still applicable to an odd number of slices. For the former, if the center of the volume is treated as 0, then the first rectangular volume is created from the slices immediately above (+1 slice) and below (−1 slice) this center. The cross-sectional view of the 1^{st} rectangular volume is shown in Fig. 3.12(a). The assumption here is that for a relatively spherical body, these two slices will have similar, if not identical coordinates defining their respective contours. As such, these two slices can be considered as 'corresponding slices', which implies that using the planar bounds created from these two slices as the top and bottom surfaces, a rectangular volume can be formed by joining up the eight corners of the two planar bounds. Moreover, this volume will more or less be in the shape of a rectangular volume. The volume is still defined by the equations in Eq. (3.16); however $\bar{P}_x$, $\bar{P}_y$ and $\bar{P}_z$ are now the contours of slices +1 and −1, instead of being the contours of the entire volume. The 2^{nd} rectangular volume is constructed using the same set of equations but $\bar{P}_x$, $\bar{P}_y$ and $\bar{P}_z$ take up the coordinate points of slices +2 and −2, because the slices of interest here are +2 and −2. Similarly, the 3^{rd} volume is constructed using slices +3 and −3, and so on and so forth.

As more rectangular volumes are constructed this way, the corresponding slices become farther apart from the center of the volume and from each other. So the

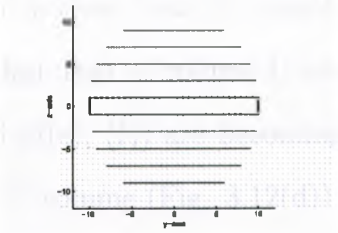

(a) Cross-sectional view of the bounds for the 1^{st} volume

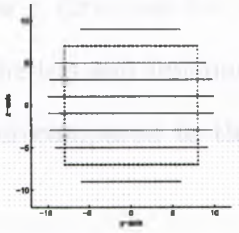

(b) Cross-sectional view of the bounds for the 4^{th} volume

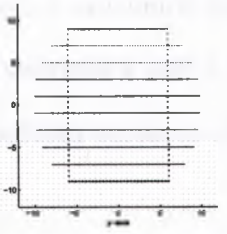

(c) Cross-sectional view of the bounds for the 5^{th} volume

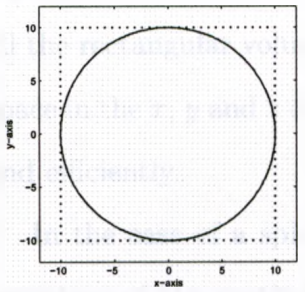

(d) Planar bounds as top and bottom surfaces for the 1^{st} volume

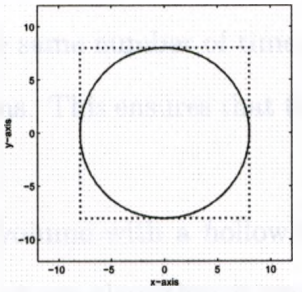

(e) Planar bounds as top and bottom surfaces for the 4^{th} volume

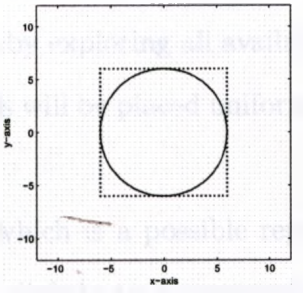

(f) Planar bounds as top and bottom surfaces for the 5^{th} volume

Figure 3.12: Cross-sectional and planar views of IDDO bounds

volumes have progressively smaller top and bottom surfaces (planar bounds) due to less 2D areas covered by $\bar{P}_x$ and $\bar{P}_y$ of the corresponding slices but greater length in the z direction due to the slices being farther apart from each other. Figure 3.12(b) shows the cross-sectional view of the 4^{th} volume, and Fig. 3.12(c) shows the cross-sectional view of the 5^{th} volume. Comparing Fig. 3.12(b) and (c) to Fig. 3.12(a),

it is clear that the lengths in the z direction for volumes 4 and 5 are much bigger than that of volume 1; whereas the top and bottom surfaces of volumes 4 and 5 (Fig. 3.12(e), (f)) are becoming smaller compared to the top and bottom surfaces of the 1^{st} volume (Fig. 3.12(d)).

The collection of rectangular volumes from all slices combine together to form the approximate spherical volume. Each time '*fmincon*' is invoked by the proposed algorithm, a different volume is selected for seed placement. The aim is to go through all the rectangular volumes the same number of times, thereby exploring all available space in the x, y and z directions. This ensures that the seeds will be placed uniformly and efficiently.

In the case of a spherical volume with a hollow tube, which is a possible representation of the urethra, the above algorithm is modified slightly to accommodate this change. In contrast to a solid sphere where one rectangular volume is created from two corresponding slices, now four rectangular volumes will be created instead. The planar bounds for the top and bottom surfaces are still defined by Eq. (3.8), so that there are now 4 regions. The rectangular volumes are still created the same way as before, by joining up the same regions from corresponding slices, e.g., joining region 2 on slices $+1$ and -1 will create a rectangular volume that covers part of the target volume but not the forbidden volume. In this way, 4 rectangular volumes will be created from each pair of corresponding slices. For such a shape, the optimization routine has to cycle through four times as many volumes on each call of '*fmincon*' to uniformly place the seeds throughout the spherical volume. In this manner, the placement of seeds in the forbidden (hollow) region of the volume will be avoided with the best effort.

Having specified the bounds for potential locations of a seed in all (x, y and z) directions, the last requirement prior to invoking the optimization routine is to

provide the location of an arbitrary temporary seed (*temp_seed*). Similar to how it has been done in DOPAL, *temp_seed* for IDDO is also calculated using the COM formula given in Eq. (3.2a) and Eq. (3.2b). The goal of the optimization routine is to move *temp_seed* to a location that will provide an optimal radiation coverage to the whole target, confined in the space set by the equations given in Eq. (3.16). The actual location of the seeds (*new_seeds_IDDO*) produced by the optimization routine are checked and verified to make sure that they are all within the tumor volume, while the overdose and underdose violation amount due to *new_seeds_IDDO* are calculated again.

This process is repeated for a maximum of 10 iterations, unless convergence has been reached before then. This number has been chosen experimentally and can be varied as desired. During these iterations, the current minimum violation amount *cur_vioamt_IDDO* is checked every time *new_seeds_IDDO* is produced by IDDO. If IDDO's current violation amount due to *new_seeds_IDDO* is lower than the currently stored *min_vioamt_IDDO*, then *final_seeds_IDDO*, which is the eventual output of the IDDO algorithm, gets replaced by *new_seeds_IDDO* and *min_vioamt_IDDO* gets replaced by *cur_vioamt_IDDO* and the optimization process can continue on for another 10 iterations. The only condition under which IDDO is terminated immediately is when *cur_vioamt_IDDO* due to *new_seeds_IDDO* happens to be 0, implying that all contour points in the entire volume are within the accepted upper and lower limits of the prescribed dose. At this time, *final_seeds_IDDO* is replaced by *new_seeds_IDDO* and gets produced by IDDO as the final solution.

3.3.2 IDDO's '*fmincon*'

The IDDO algorithm also uses the '*fmincon*' optimization routine from MATLAB's optimization toolbox. In contrast to the complex objective function that governed the optimization of the pre-planning algorithm, this particular objective function (*IDDO_Obj_Fn*) is given below simply as:

$$\text{Minimize } \{\sum_{i=0}^{n}[req\_dose(i) - D(i)]^2\} \tag{3.17}$$

where *req_dose(i)* and *D(i)* correspond to the required dose and the actual dose at the i^{th} point on the contour volume, respectively. *D(i)* here is the summation of dose from all seeds that are currently inside the tumor volume, which consist of *cur_dep_seeds* and *new_seeds_IDDO*. Thus, the aim of the objective function in Eq. (3.17) is to minimize the squared sum of the difference between the actual dose delivered and the desired dose at each point on the contour volume.

The optimization constraints for the IDDO algorithm, *IDDO_Opt_Cons*, are also similar to the pre-planning optimization constraint in Eq. (3.13). In a sense that it also specifies a certain spacing between adjacent seeds (given below in Eq. (3.18)). The only difference here is that the spacing is defined in three-dimensional space whereas for pre-planning, the spacing was only applicable in the XY-plane. So that for every i^{th} seed, S_i, that belongs to the matrix of seeds $\bar{S_{xy}}$, the *IDDO_Opt_Cons* is:

$$\|S_{i+1} - S_i\| \geq k, \text{ for } S_i \in \bar{S_{xy}} \tag{3.18}$$

where $\|\cdot\|$ is the Euclidean norm in 3D space.

Chapter 4

Experiments and Results

This chapter presents information on how the experiments were conducted on a variety of shapes in the simulation environment, as well as in the *ex vivo* environment on sample lung tumors and prostate phantoms. The equipment involved in the experiments for *ex vivo* lung tumors and prostate phantoms is described in section 4.1.1. Section 4.1.2 and 4.1.3 give a description of the evaluation procedure for DOPAL and IDDO respectively, with particuar focus on how to use an existing dosimetry planning software to verify the accuracy of these proposed algorithms. Lastly, the experimental results are presented in section 4.2 and discussed in section 4.3.

4.1 Experimental Evaluation Procedure

In this section, first, the equipment used to evaluate the proposed algorithms is presented, followed by a detailed description on how an existing dosimetry planning software will be used to verify the accuracy of both DOPAL and IDDO.

4.1.1 Equipment Set-up

4.1.1.1 Additional Software

Seed configurations for both DOPAL and IDDO are obtained in the MATLAB environment, since both algorithms have been programmed in MATLAB. However, MATLAB alone is not sufficient for evaluating the accuracy of these algorithms. As such,

a dosimetry planning software provided by Dr. Fenster at Robarts, is used to compare and verify the accuracy of the dosimetry planning results produced by DOPAL. This software will be referred to as RDP, short for "Robarts Dosimetry Planning" software, for ease of reference. A commercial version of this software for prostate brachytherapy is called Sonographic Planning for Oncology Treatment (SPOT) and was described in section 2.1.1. The RDP software used for this project was modified by the Robarts group for the lung brachytherapy project in [50].

4.1.1.2 Additional Hardware

As described in Chapter 3, both DOPAL and IDDO require a set of contour images of the target volume before they can be executed. Therefore accurately obtaining US images of the tumor volume is crucial for the evaluation of the algorithms. To this end, an ultrasound machine (Philips iU22) shown in Fig. 4.1 was used to obtain the US images for *ex vivo* lung tumors. The tumors were constructed based on the approach in [55]; the tumors have diameters $5mm$, $10mm$ and $20mm$. Tumors in operable lung cancer patients are generally less than $3cm$ across [56]. For our experiments, the tumors were made from agar (Sigma Gelrite Gellan Gum), water and barium, and were heated before they were injected into cold, collapsed porcine lungs. The lungs with injected tumors were refrigerated overnight for the tumors to solidify. The C-Arm was used to verify the location of the tumors prior to acquiring the US images using the Philips iU22 US machine. A sample x-ray image obtained from the C-Arm is shown in Fig. 4.2. Tumor 1 in Fig. 4.2(a) is smaller in comparison to the other tumors in Fig. 4.2(b), where the tumors above the lobe (tumors 3 and 4) are considerably larger.

For prostate brachytherapy on the other hand, to obtain US images for the life-sized prostate phantom shown in Fig. 4.4, the TRUS probe in Fig. 4.3 is used, which

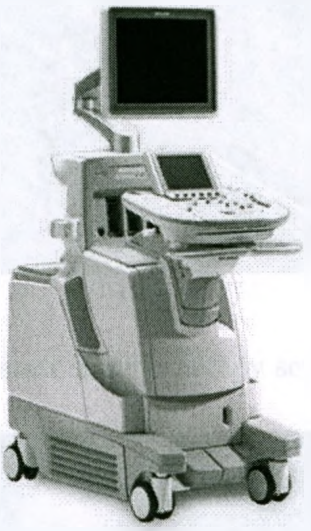

Figure 4.1: Philips iU22 ultrasound machine

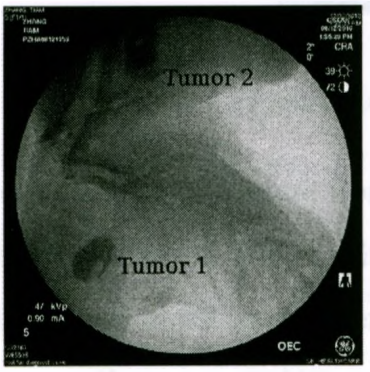

(a) X-ray image showing locations of tumors 1 and 2

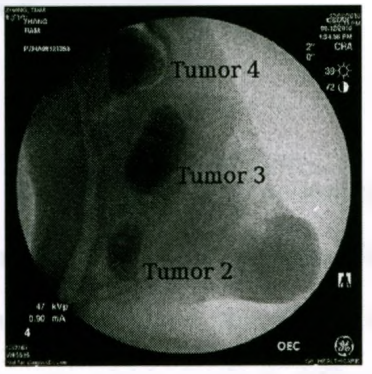

(b) X-ray image showing locations of tumors 2, 3 and 4

Figure 4.2: X-ray images of samples tumors in pig lung

is a part of the prostate brachytherapy set-up from CSTAR [57].

The prostate phantom in Fig. 4.4 was not built for this project; however it is still applicable to the research conducted in this project since the size of the phantom

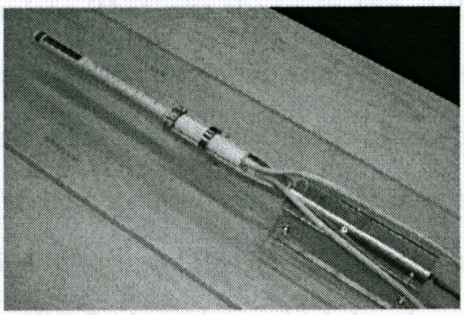

Figure 4.3: Prostate brachytherapy set-up at CSTAR

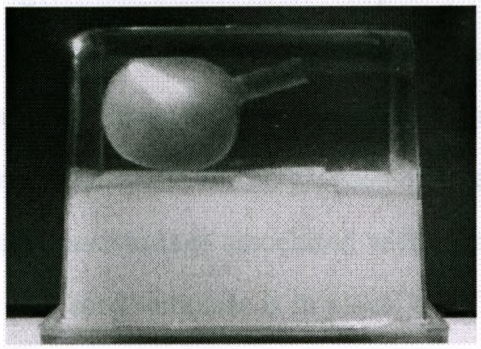

Figure 4.4: Life-sized prostate phantom

matches that of a prostate from real life. Nonetheless, it is necessary to evaluate both DOPAL and IDDO algorithms on more than one test subject. To achieve this goal, two sets of US images were acquired using the same phantom. In the first set of images, there was slightly more noise present, which made it difficult to identify the whole prostate; while the second set of images contained little noise so that the entire prostate was easily identified. The ends of the figure in the first set of images (where there were more noise) were deleted from the image set, thereby resulting in a prostate that was slightly smaller than the prostate from the second set of images.

In terms of seed placement, the AESOP brachytherapy set-up shown in Fig. 4.5 was used. This equipment is different from the current clinical set-up, in the sense

that there is no seed template (that was shown in Fig. 1.2) required to deposit the seeds at their desired locations. Furthermore, the AESOP set-up provides improved precision in seed placement such that the locations of the needles no longer need to be specified in terms of the hole location on the seed template. Instead the location of the seeds can be specified in terms of its desired xyz Cartesian coordinates. This is in the best interest of the IDDO algorithm, which has been implemented to deposit seeds at any location within the volume to achieve an optimal radiation coverage of the tumor. In fact, the algorithms described in Chapter 3 were designed to be used with a robotics-assisted brachytherapy set-up, similar to the AESOP set-up in Fig. 4.5, for use in the prostate, the lung and possibly other organs where seed insertion could be done from various angles due to the absense of a seed template.

However, there is also a disadvantage associated with it from the algorithm implementation point of view. If a seed template is in place, then there would be a limited number of potential seed locations, as is the case with Lee's MIP optimization. In the absence of a seed template, associated with the AESOP set-up is an infinite number of potential seed locations, making the optimization problem more difficult to solve because more calculations and more logical eliminations are required to determine the seed locations of an optimal plan.

With these additional hardware and software, the DOPAL and IDDO algorithms can be properly evaluated. The evaluation procedure for these algorithms are described below.

4.1.2 Evaluation Procedure for DOPAL

The evaluation of the performance of the algorithms starts with simple 2D shapes such as a circle, or a planar donut (a simplified representation of a prostate with the

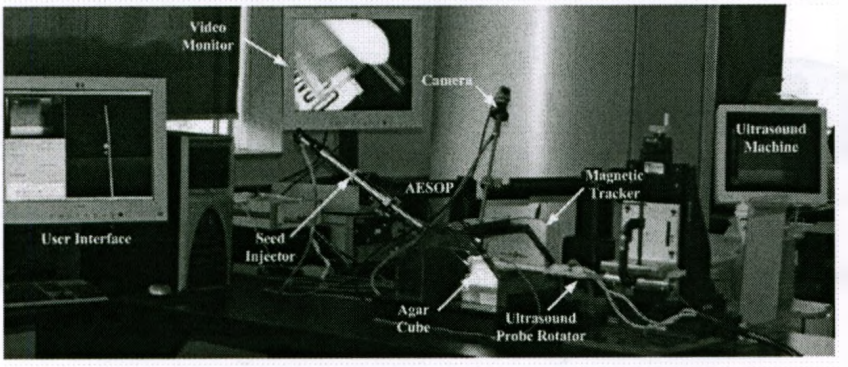

Figure 4.5: AESOP brachytherapy set-up at CSTAR

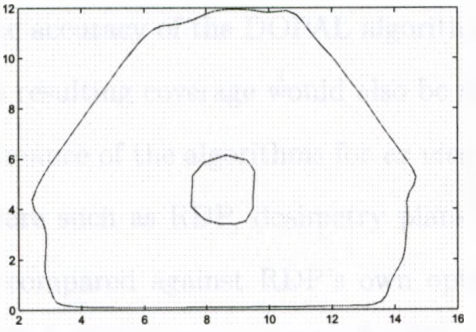

Figure 4.6: 2D view of the prostate with urethra

urethra), before moving on to a slightly more complicated scenario such as a realistic planar view of the prostate with the urethra, as shown in Fig. 4.6.

The next step of the evaluation process involves performing dosimetry planning on simple 3D shapes, such as a solid cylinder, a cylinder with a hollow tube or, a sphere with a hollow tube. These figures are shown in Fig. 4.7.

The DOPAL algorithm is invoked to produce a dosimetry plan on the shapes illustrated in Figs. 4.6 and 4.7, their corresponding results are presented in section 4.2.1 and section 4.2.2. The target regions have all been assigned a U_b value of 110% of the desired dose, and a L_b value of 90% of the desired dose. The U_b and L_b values

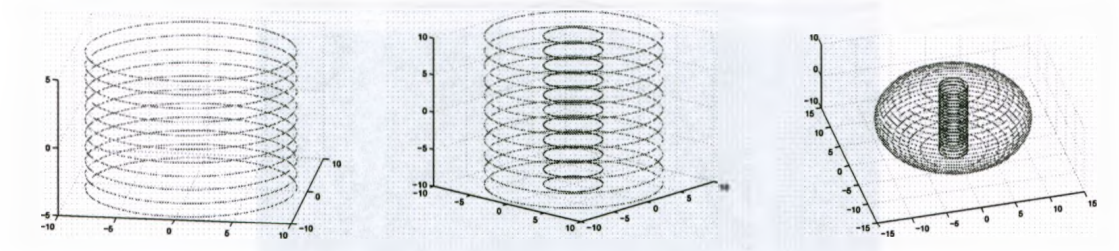

(a) Solid Cylinder (b) Cylinder with Hollow tube (c) Sphere with Hollow tube

Figure 4.7: Simple 3D shapes

assigned to the forbidden regions in Fig. 4.7(b) and Fig. 4.7(c) are 110% and 80% of the desired dose, respectively. These values were chosen relatively close to the desired dose at 100% to reflect the accuracy of the DOPAL algorithm. Depending on the U_b and L_b values chosen, the resulting coverage would also be different.

To evaluate the performance of the algorithms for *ex vivo* tumors against existing dosimetry planning software such as RDP, dosimetry plans created by DOPAL are imported into RDP and compared against RDP's own optimized dosimetry plans. As described in section 3.2, DOPAL requires only the 3D contour of the target volume, which may be acquired through any imaging modality. However, to prove that DOPAL is working correctly, the same target volume information also has to be provided to RDP for verification purposes. Due to the fact that RDP works exclusively with US images, these experiments were therefore limited to the US imaging modality only.

After obtaining the ultrasound images of the tumors as explained in section 4.1.1.2, the images are imported into RDP for contouring. Contouring in RDP has to be done manually by clicking and selecting points on every slice of the target volume. The minimum interval for contouring in RDP is $1mm$ along the z-axis, however the minimum interval at which the contour can be viewed is $2.5mm$, as shown in the bottom of Fig. 4.8. As a result, needles and seeds can only be added to consecutive

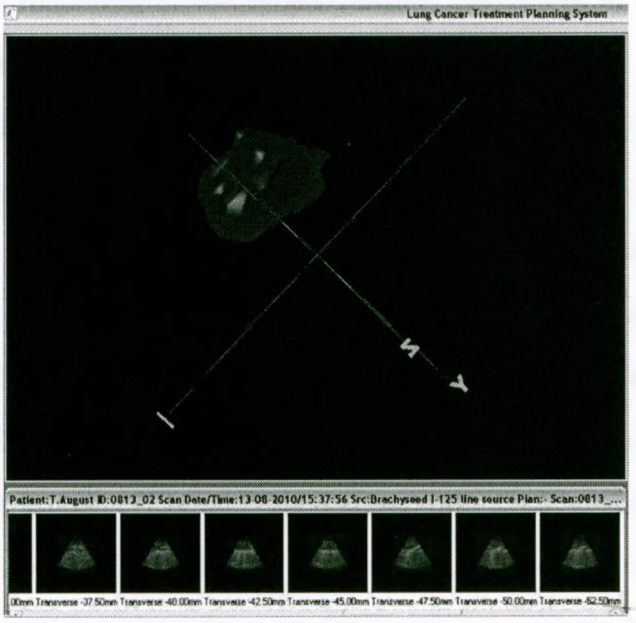

Figure 4.8: 3D view of a sample tumor in RDP

contours at multiples of $2.5mm$, meaning that the minimum spacing between seeds on adjacent slices is $2.5mm$ if added manually. Needles and seeds can also be added to slices that are 5.0, 7.5 or $10mm$ apart, and so on up to the last contour in the volume. For instance, if the first contour slice is placed at $z = 0mm$, then seeds can only be added on slices with a z-coordinate of 2.5, 5.0, or $n \times 2.5$, where n is the n^{th} consecutive slice from the first slice. This implies that the z-coordinate of a seed (S_z) must be at a distance of multiples of $2.5mm$ from where the first slice is, which effectively limits the location of the seeds produced during pre-planning and seed compensation. Even if DOPAL can be designed to cope with this, the same cannot be done for IDDO since seed compensation should produce seeds anywhere inside the tumor volume as long as a compensated coverage can be obtained. This is to say that seeds produced by IDDO cannot be placed in RDP for verification purposes.

Nonetheless, the target volume is in fact defined by a discrete number of slices, so

to get a 3D surface rendering of the target volume, the values in between the slices are interpolated using RDP's own built-in interpolation scheme. The 3D surface rendering from RDP is a useful feature in displaying the volumetric isodose coverage, a 3D surface rendering of a sample target volume is shown in Fig. 4.8.

Next, the set of points describing the volume is recorded and stored in RDP, however RDP offers no direct exportation to MATLAB so the only way to use this information in MATLAB is to first store it in another program, say for example Microsoft Excel™. Once the 3D contour information has been pasted into Excel, which contains the x, y and z coordinates of the volume contour in a slice-by-slice arrangement, it is then imported into MATLAB for use in the DOPAL and IDDO algorithms. The results obtained from these algorithms can be compared against the results obtained from RDP.

RDP also contains an optimization feature that can generate dosimetry plans automatically. Spacing between neighboring seeds on the same slice can be selected as either $5mm$ or $10mm$; spacing between neighboring seeds on adjacent slices can also be selected as either $5mm$ or $10mm$. Therefore there are a total of four optimization schemes from RDP, so in total 4 dosimetry plans are generated by RDP for the *ex vivo* lung tumors and the prostate phantoms.

To compare the above dosimetry plans from RDP against the dosimetry plan from DOPAL, we use several parameters obtained from the Dose Volume Histogram (DVH), as done in [47, 50, 58, 59, 60]. A sample DVH graph is shown in Fig. 4.9, where the percentage dose is the horizontal axis while the percentage volume is the vertical axis. In Fig. 4.9, approximately 83.8% of the volume is receiving 100% of the dose as indicated. To evaluate the dosimetry plan for a lung tumor, we use the same DVH parameters as the ones that are used in [50], they are $D90$ (dose to 90% of the volume), $V90$ (volume receiving at least 90% of the dose), $V100$ (volume

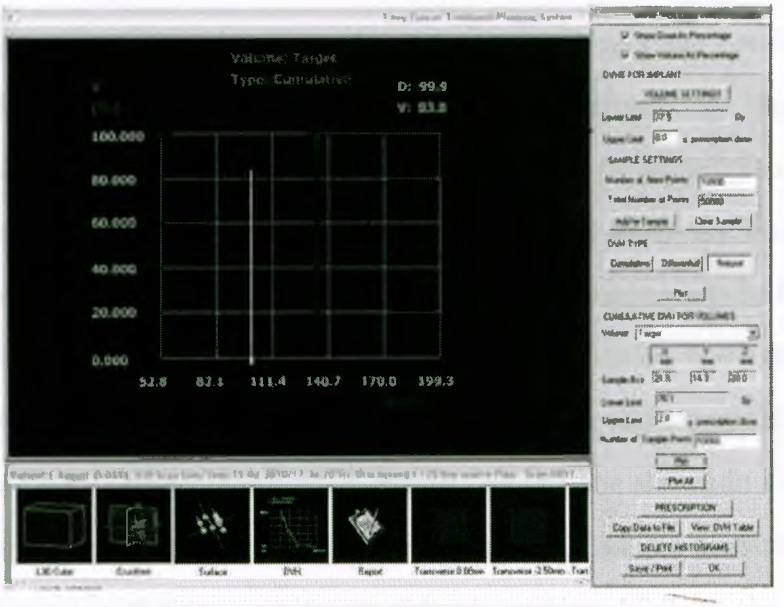

Figure 4.9: Sample Dose Volume Histogram from RDP

receiving at least 100% of the dose) and $V200$ (volume receiving at least 200% of the dose). The $V90$ and $V100$ parameters have been shown to be uninfluenced by seed misplacements, which implies that values close to 100% for these two parameters will ensure a good plan has been achieved. For prostate brachytherapy, $D90$, $D100$, $V100$, $V120$ and $V150$ are used in [47, 58, 59, 60]. These parameters will also be used in this thesis. Reference [6] also provides recommended values for $V150$ and $D90$ for an optimal plan in prostate brachytherapy.

In order to obtain DVH parameters in the same environment so that they are consistent between both RDP and DOPAL, it was decided that the DVH function from RDP will be used instead of writing another program in MATLAB to do the same thing. To obtain DVH parameters for the dosimetry plan from DOPAL, the seeds from the DOPAL plan must be plotted in RDP, where a xyz translation was

performed to translate the seeds from MATLAB units to RDP units. In RDP, and like in any other dosimetry planning software, the position of the needles and seeds can be viewed after they have been added manually. In contrast, now that the desired locations of the seeds are known, needles and seeds can be added accordingly. By activating all the seeds that are deposited at their desired locations, an overall slice-by-slice isodose coverage can be obtained similar to the one shown in Fig. 1.4. An isodose coverage shows regions within a target volume receiving the same amount of dose. Then the pre-planning DVH parameters from both RDP and DOPAL can be obtained from their corresponding DVH graphs like the one shown in Fig. 4.9.

The pre-planning results obtained from RDP and DOPAL are presented in section 4.2.2. The discussion of these results are given in section 4.3.2 for the lung tumors and section 4.3.4 for the prostate phantoms.

4.1.3 Evaluation Procedure for IDDO

To verify the functionality of the IDDO component, a portion of the seeds obtained from DOPAL are manipulated such that the new coverage is no longer the same as the coverage of the original plan from DOPAL. These manipulated seeds are used as an input (*cur_dep_seeds*) to the IDDO algorithm, and IDDO is asked to generate new locations for the remaining seeds (*new_seeds_IDDO*) in order to compensate for the manipulations that took place. The final coverage as a result of the combination of *cur_dep_seeds* and *new_seeds_IDDO* should satisfy the imposed upper and lower limits of the accepted dose. These limits were described in section 3.3.1, the values of which can be either the summation of pre-plan's intended dose and the user-specified *tol_val* or new upper and lower limits specified by the user.

Unfortunately, the result of IDDO - *new_seeds_IDDO*, cannot be plotted in RDP

for comparison like it was done for DOPAL. This is because the result produced by IDDO contains seeds throughout the entire tumor volume, not necessarily fixed to the available slices. As mentioned previously, since the seeds produced by IDDO cannot be plotted in RDP to verify their accuracy, 3D radiation coverage graphs are then used to compare the seed compensation results before and after running IDDO. A separate program was written solely for this purposes, which is called *isodose3D*. It displays the isodose coverage, in both planar (2D) and volumetric (3D) views. The coverages shown by *isodose3D* will be used to evaluate the accuracy of the IDDO algorithm. The seed compensation figures are presented in section 4.2.4 and the discussion on *ex vivo* lung tumors is given in section 4.3.3 and in section 4.3.5 for prostate phantoms.

4.2 Results

4.2.1 Result for 2D Shapes

Figure 4.10 shows the simulation results of the simple 2D shapes. Figure 4.10(a), (c) and (e) show the configuration of the seeds according to the dosimetry plan produced by DOPAL, their corresponding radiation coverages at 100% of the prescribed dose are shown in Fig. 4.10(b), (d) and (f). It can be seen from Fig. 4.10(a) and (c) that for circular shapes, the seed arrangements are very uniform, even in the presence of an enclosed circle as in Fig. 4.10(c). As a result, Fig. 4.10(b) and (d) show very uniform and complete radiation coverages at 100% of the prescribed dose. The robustness of the algorithm is illustrated in Fig. 4.10(e) and (f), where the seed arrangement and the 100% radiation coverage are also uniform and complete, even though this time it is for an irregular, complex shape such as the prostate with the urethra.

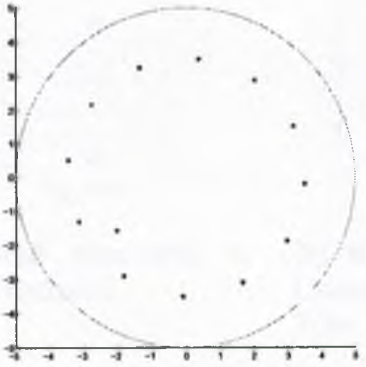

(a) Seed placement in Circle

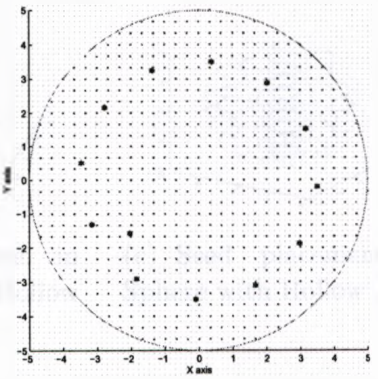

(b) Radiation coverage of Circle

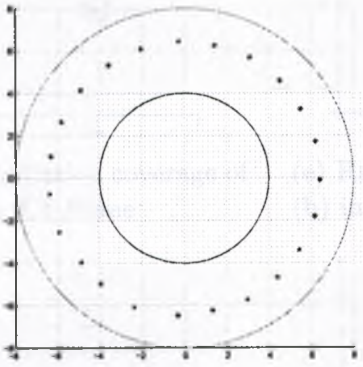

(c) Seed placement in Coax Circle

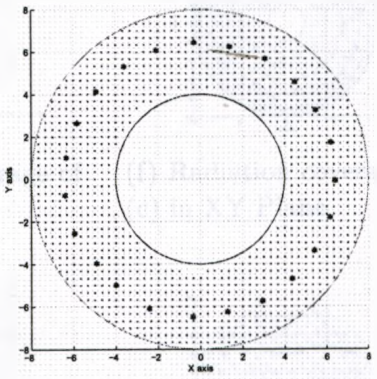

(d) Radiation coverage of Coax Circle

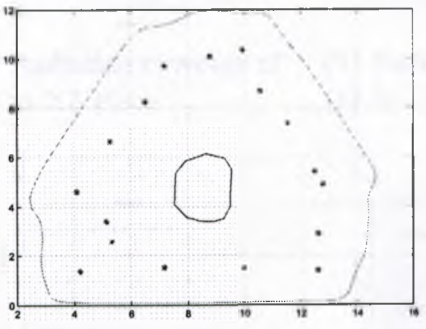

(e) Seed placement in Prostate

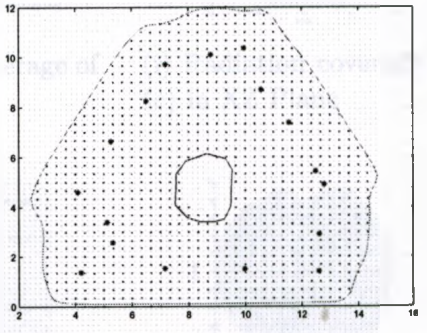

(f) Radiation coverage of Prostate

Figure 4.10: Simulation results for simple 2D shapes

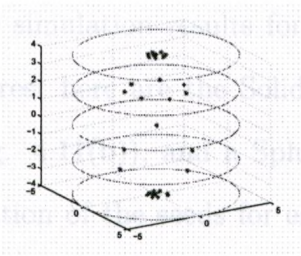

(a) Seed placement in Solid Cylinder

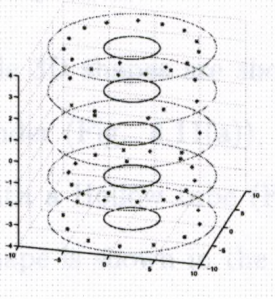

(b) Seed placement in Cylinder with Hollow Tube

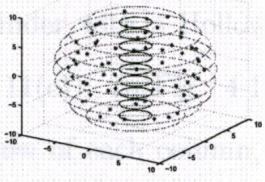

(c) Seed placement in Sphere with Hollow Tube

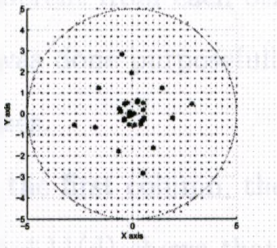

(d) Radiation coverage of (a) in XY Plane

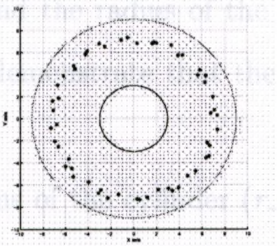

(e) Radiation coverage of (b) in XY Plane

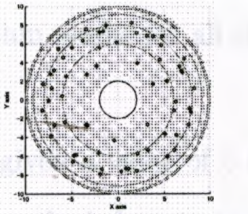

(f) Radiation coverage of (c) in XY Plane

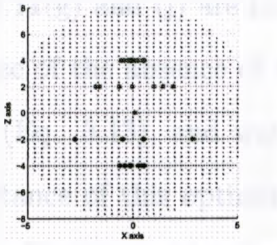

(g) Radiation coverage of (a) in XZ Plane

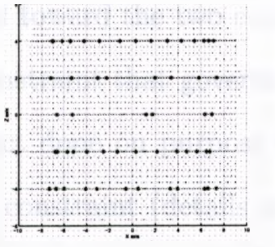

(h) Radiation coverage of (b) in XZ Plane

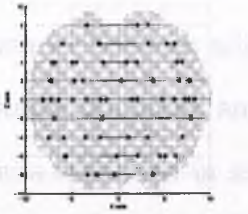

(i) Radiation coverage of (c) in XZ Plane

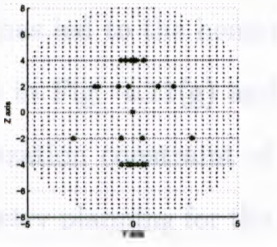

(j) Radiation coverage of (a) in YZ Plane

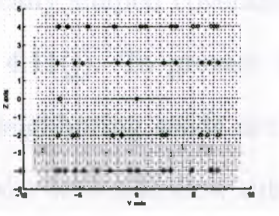

(k) Radiation coverage of (b) in YZ Plane

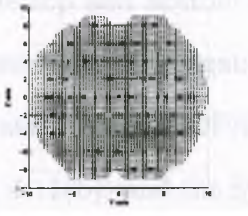

(l) Radiation coverage of (c) in XZ Plane

Figure 4.11: Simulation results for simple 3D shapes

4.2.2 Result for 3D Shapes

The simulation results for simple 3D shapes are shown in Fig. 4.11, the shapes of interest here are the Solid Cylinder (Fig. 4.11(a)), a Cylinder with a Hollow tube (Fig. 4.11(b)), and a Sphere with a Hollow tube (Fig. 4.11(c)). In Fig. 4.11, the location of the seeds for each shape is shown in the first row of each column, while the 100% radiation coverage due to the seeds viewed in XY, XZ and YZ planes are shown underneath for a complete illustration. The radius of the cylinders and sphere are different from each other, and the radius of the hollow tubes are also different. This was done purposefully to demonstrate that the algorithm works for all shapes and sizes.

In the first column, the radius of the cylinder (*r_cyl*) is given a value of 5 units. Figure 4.11(d) shows that the coverage at 100% of the prescribed dose in the XY plane is complete and uniform, however the coverages in XZ and YZ planes shown in Fig. 4.11(g) and (j) are spherical toward the two ends of the cylinder. This occured because of the absence of the constraint that governs the distance between adjacent seeds (Eq. 3.13), and was in fact done on purpose to illustrate the effect and the importance of this optimization constraint (details on this was explained in section 3.2.3). Examining the distribution of the seeds in Fig. 4.11(a), it can be seen that the seeds bunch together in the center of the top and bottom slices. This bunching of seeds has led to the hemi-spherically shaped coverages on the top and bottom slices shown in Fig. 4.11(g) and Fig. 4.11(j). To prevent this from happening again, the optimization constraint of the neighboring seeds are made available in DOPAL for dosimetry planning for the Cylinder with a Hollow tube (Fig. 4.11(b)) and the Sphere with a Hollow tube (Fig. 4.11(c)).

The cylinder in Fig. 4.11(b) has a *r_cyl* value of 9 units, while the hollow tube has

a radius (*r_tube*) of 3 units. The seeds in this figure can be seen to have assumed an uniform distribution, which resulted in uniform and complete coverages in the XY, XZ and YZ planes shown in Fig. 4.11(e), (h) and (k).

Similarly, uniform and complete coverages have been achieved in all XY, XZ and YZ planes for the Sphere with a Hollow tube, where the radius of the sphere (*r_sph*) is 10 MATLAB units and *r_tube* is 2 units. The only drawback here are the small underdosed regions (cold spots) close to the top and bottom slices of the sphere shown in Fig. 4.11(i) and (l). Had this been a solid sphere without a forbidden region, these cold spots would not have been present. The top and bottom slices of the sphere have a target radius of only 6 units, where *r_tube* is consistently at 2 units from one end to the other. The value of *r_tube* on these slices in relation to the relatively smaller value of *r_sph* makes it difficult to deliver the perfect amount of dose to these slices. Despite the observable cold spots for the coverage at 100% of the prescribed dose, these regions are fully dosed at 90% of the prescribed dose, therefore still satisfying the U_b and L_b conditions.

4.2.3 *ex vivo* and Phantom Pre-planning Results

The effectiveness of the dosimetry plans from DOPAL on *ex vivo* tumors and prostate phantoms are compared against all four of RDP's optimization schemes. The most optimal plan would consist of high values ($\approx$ 100%) for $V100$ parameters, and low values for $V200$ or $V150$ parameters. This is beacuse the amount of dose delivered to the entire volume should be as close to 100% of the prescribed dose as possible, while the amount of volume receiving $>$ 100% of the prescribed should be limited in order to prevent damage to the surrounding anatomical structures.

Tables 4.1-4.3 show the DVH values of all five plans (4 from RDP and 1 from

Table 4.1: DVH parameters of $5mm$ diameter tumors

Plan	D90	V90	V100	V200
DOPAL	82.5Gy	64%	56.9%	19.5%
	109.9Gy	80%	74%	31.9%
RDP 5_5	DNE	DNE	DNE	DNE
	54.9Gy	61.9%	58.7%	33.8%
RDP 5_10	DNE	DNE	DNE	DNE
	DNE	DNE	DNE	DNE
RDP 10_5	DNE	DNE	DNE	DNE
	DNE	DNE	DNE	DNE
RDP 10_10	DNE	DNE	DNE	DNE
	DNE	DNE	DNE	DNE

DOPAL) for lung tumors with diameters of $5mm$, $1cm$ and $2cm$. These tumor sizes were selected because the tumors found on clinically operable patients are less than $3cm$ as suggested by [56]. The first row under each plan name refers to the first experimental tumor while the second row refers to experimental tumor number two. The convention used to distinguish the four different plans from RDP is done by the use of two numbers, for example in $RDP5\_5$, the 1^{st} number represents the distance between neighboring seeds on the same slice, while the 2^{nd} number represents the distance between neighboring seeds on adjacent slices. The results in these tables are obtained using the default value for the initial strength of the source at $1U$.

One thing worth mentioning here is that when DOPAL was used on the $1cm$ tumor, the U_b and L_b values were specified as 10% higher than the U_b and L_b values for the $5mm$ and $2cm$ tumors. This resulted in the elevated values for the $D90$ and $V200$ parameters in Table 4.2, in comparison to the lower $D90$ and $V200$ values in Tables 4.1 and 4.3.

Table 4.4 shows the DVH values of all five plans for the target region of the prostate phantom, and Table 4.5 shows the DVH values of all five plans for the urethra region. Both tables follow the same convention to the lung tumor tables, where the first row

Table 4.2: DVH parameters of $1cm$ diameter tumors

Plan	D90	V90	V100	V200
DOPAL	169.1Gy	97.2%	95.3%	51.7%
	160.1Gy	96.7%	93.7%	59%
RDP 5_5	163.9Gy	99%	94.4%	60.4%
	146.1Gy	92.8%	90.4%	71.3%
RDP 5_10	76.1Gy	68.3%	60.1%	32.4%
	133.1Gy	89.6%	88.2%	69.8%
RDP 10_5	30.1Gy	27.4%	26.4%	10%
	DNE	DNE	DNE	DNE
RDP 10_10	30.1Gy	27%	25.7%	10.5%
	DNE	DNE	DNE	DNE

Table 4.3: DVH parameters of $2cm$ diameter tumors

Plan	D90	V90	V100	V200
DOPAL	149.9Gy	96.7%	92.1%	40.5%
	140Gy	93.3%	88.8%	54.2%
RDP 5_5	24.6Gy	28.1%	26.6%	12.3%
	185.4Gy	98.8%	98%	70.5%
RDP 5_10	24.6Gy	28.3%	27%	12.3%
	133.9Gy	91.2%	87.4%	51.4%
RDP 10_5	DNE	DNE	DNE	DNE
	106.3Gy	78.8%	71.6%	27.5%
RDP 10_10	DNE	DNE	DNE	DNE
	84.4Gy	63.8%	55.8%	19.1%

under each plan name represents the values for the 1^{st} prostate phantom, and the second row represents the values for the 2^{nd} phantom. The naming of the dosimetry plans in these table also use the same convention as before.

Lee's results from [47] are also presented in these two tables. Due to the $0.57U$ source strength used in [47], DOPAL and RDP results in Table 4.4 and 4.5 have also used the same source strength. Reference [47] presents the DVH values for certain parameters only, thus Not Available (N/A) are used in places in Tables 4.4 and 4.5 where values for the desired DVH parameters from [47] are unknown.

Table 4.4: Target DVH parameters of prostate phantoms

Plan	D90	D100	V93	V100	V150
DOPAL	150.9Gy	87.5Gy	96.7%	93.3%	40.8%
	153.1Gy	99.7Gy	96.8%	94%	42.3%
RDP 5_5	115.8Gy	50.8Gy	85.9%	83.4%	57.4%
	129.9Gy	68Gy	88.9%	86.6%	65.8%
RDP 5_10	115.4Gy	42.8Gy	85.5%	82.7%	58%
	127Gy	68.5Gy	87.8%	85.2%	62%
RDP 10_5	23.7Gy	9.7Gy	28.8%	25.4%	9.9%
	34.2Gy	20.9Gy	22.6%	20.2%	9.0%
RDP 10_10	13.6Gy	5.8Gy	7.2%	4.7%	3.5%
	10.1Gy	5.3Gy	6.3%	5.7%	3.7%
Lee	N/A	N/A	100%	N/A	N/A

4.2.4 *ex vivo* and Phantom IDDO Results

As described in section 4.1.3, only MATLAB figures are used to verify the accuracy of the IDDO component, which is due to the fact that IDDO allows seed placement in the entire z-space of the target volume, meaning that the seeds are likely to fall in regions between slices, which cannot be specified in RDP since the slices in RDP are fixed. In any case, it would be sufficient to verify the accuracy of the IDDO component using MATLAB figures alone, as long as the coverage displayed by *isodose3D* of this thesis (refer to section 4.1.3) can be shown to match the figures from RDP. Figure 4.12(a) shows the isodose coverage on every slice of a target volume obtained from RDP, and Fig. 4.12(b) shows the isodose coverage from *isodose3D* of the same slices of the same volume using the same seeds. There are only a few small differences at certain points, the causes of which are explained in section 5.1. Nonetheless, the differences are negligibly small so that the slice-by-slice views from RDP are considered to be identical to the slice-by-slice views from MATLAB.

To show a different coverage to the one from dosimetry planning, seeds from pre-planning are deliberately misplaced or skipped, the resulting coverages due to this are

Table 4.5: Urethra DVH parameters of prostate phantoms

Plan	D90	D100	V90	V100	V120	V150
DOPAL	142.1Gy	117.1Gy	97.1%	86.4%	18.6%	0.3%
	148Gy	122.8Gy	99.5%	95.7%	28.4%	3.7%
RDP 5_5	98.3Gy	60.6Gy	75.9%	71.7%	62.2%	42.8%
	144.2Gy	92.3Gy	95.7%	90.1%	74.7%	55.9%
RDP 5_10	85.5Gy	49.6Gy	81.1%	77.1%	68%	44.4%
	122.1Gy	75.8Gy	87.2%	80.6%	64.6%	33.9%
RDP 10_5	20.2Gy	11.9Gy	20.8%	10.6%	1.3%	0%
	35.9Gy	29.4Gy	5.3%	2.5%	0.5%	0.1%
RDP 10_10	11.3Gy	7.1Gy	0.5%	0.1%	0%	0%
	5.9Gy	3.8Gy	0.2%	0.1%	0%	0%
Lee	N/A	N/A	N/A	N/A	> 50%	N/A

(a) Slice by slice isodose views of a tumor volume from RDP

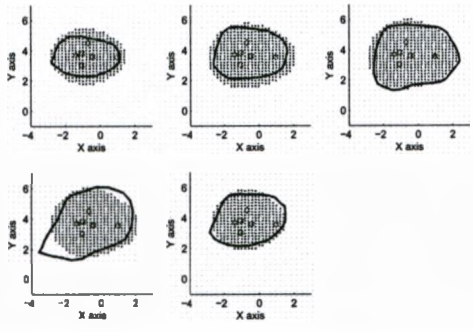

(b) Same isodose views as in Fig. 4.12(a) from *isodose3D*

Figure 4.12: Isodose comparison between RDP and *isodose3D*

shown in the 1^{st} and 2^{nd} columns of Figs. 4.13 and 4.14. These two figures show the coverage at 100% of the prescribed dose for the lung tumors in the XY-plane due to

the pre-plan seeds, manipulated seeds as well as the compensated seeds from IDDO, in columns 1, 2 and 3 of each figure respectively. Each row in these figures represents the same slice.

Figures 4.17 and 4.18 provide a comparison between the original coverage (first row in each figure), coverage due to seed manipulations (second row in each figure), and the coverage after compensating for the manipulation by running IDDO (third row in each figure), for the two prostate phantoms. The compensated results in Fig. 4.17(e) and (f) are obtained by running IDDO with the aid of a tolerance value, which was specified as *tol_val*= 5; on the otherhand, the coverage due to seed compensation in Fig. 4.18(e) and (f) are obtained without *tol_val*, which means that U_b and L_b values of the target volume were specified manually.

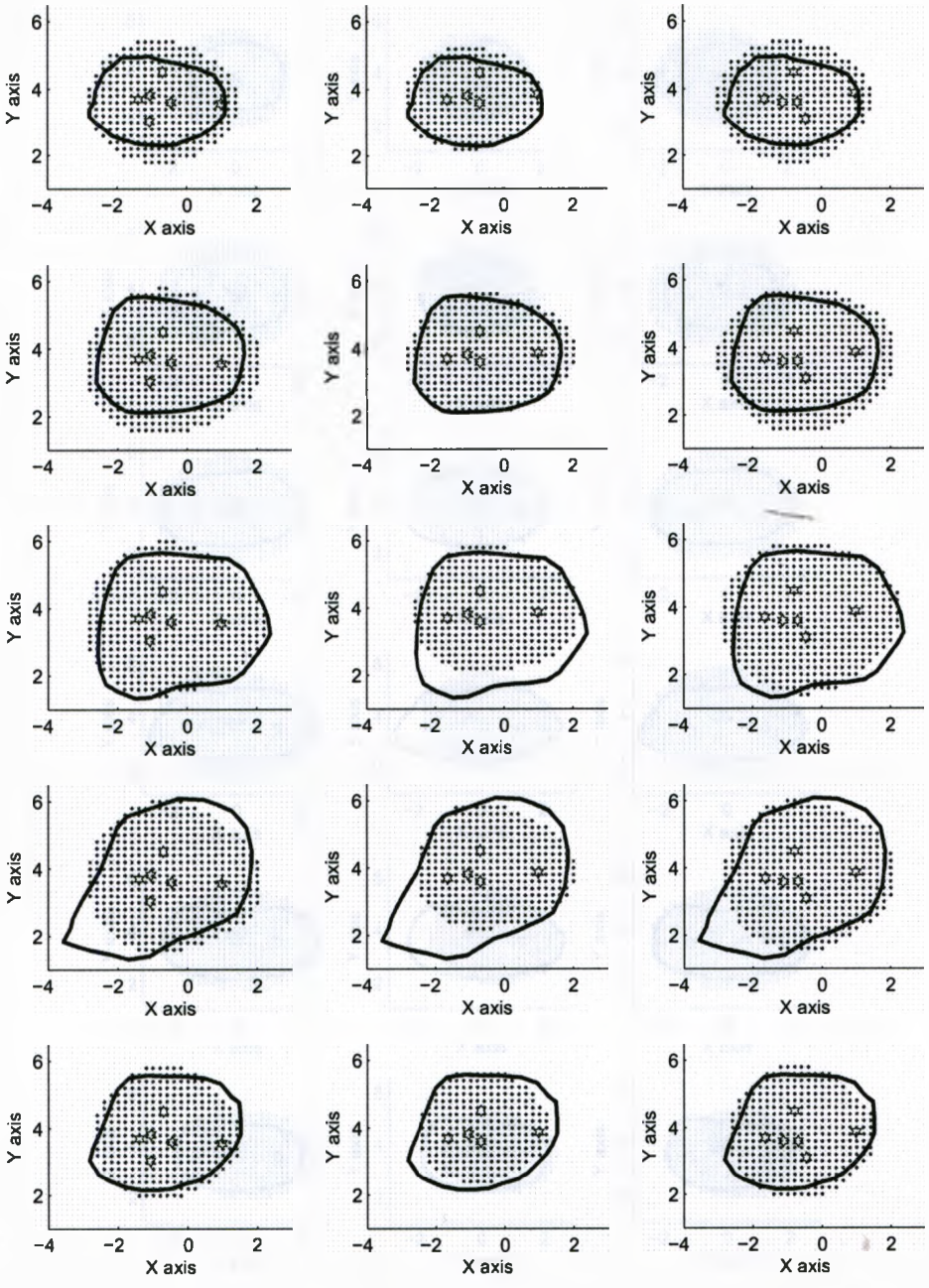

Figure 4.13: Before and after seed compensation for tumor 1 in XY-plane

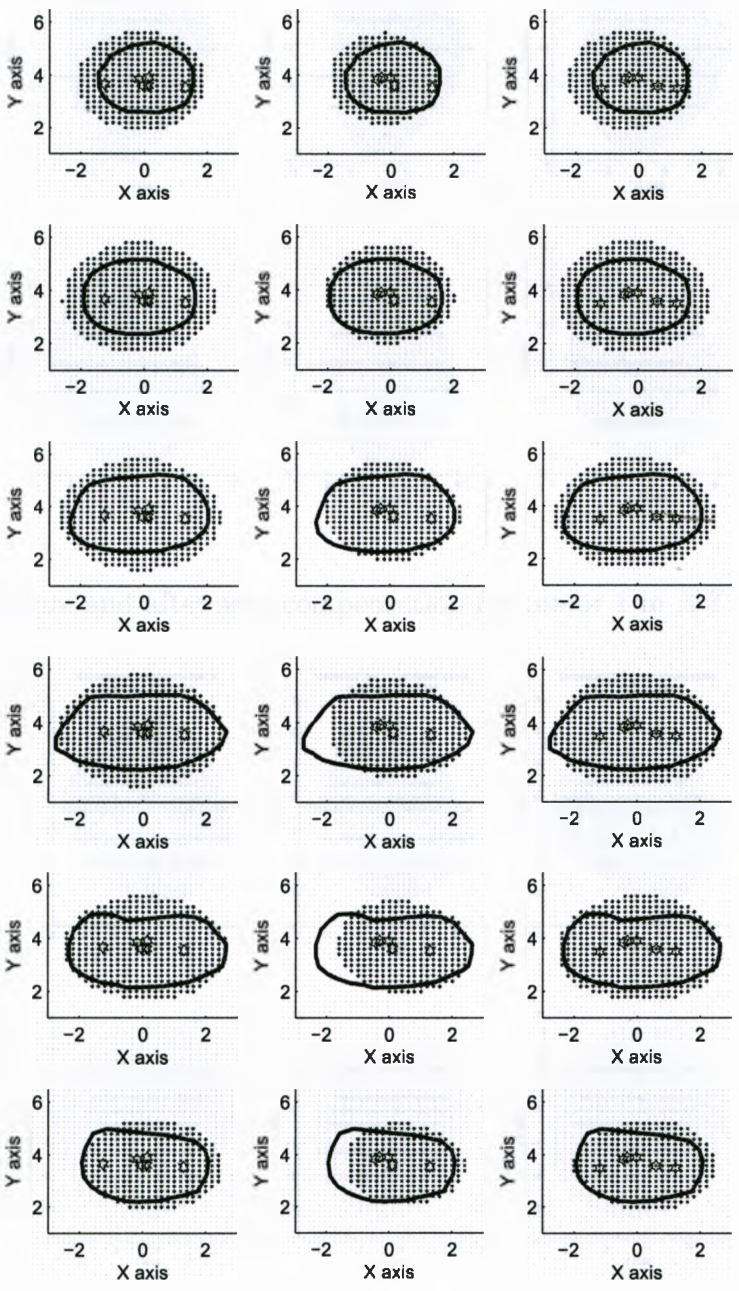

Figure 4.14: Before and after seed compensation for tumor 2 in XY-plane

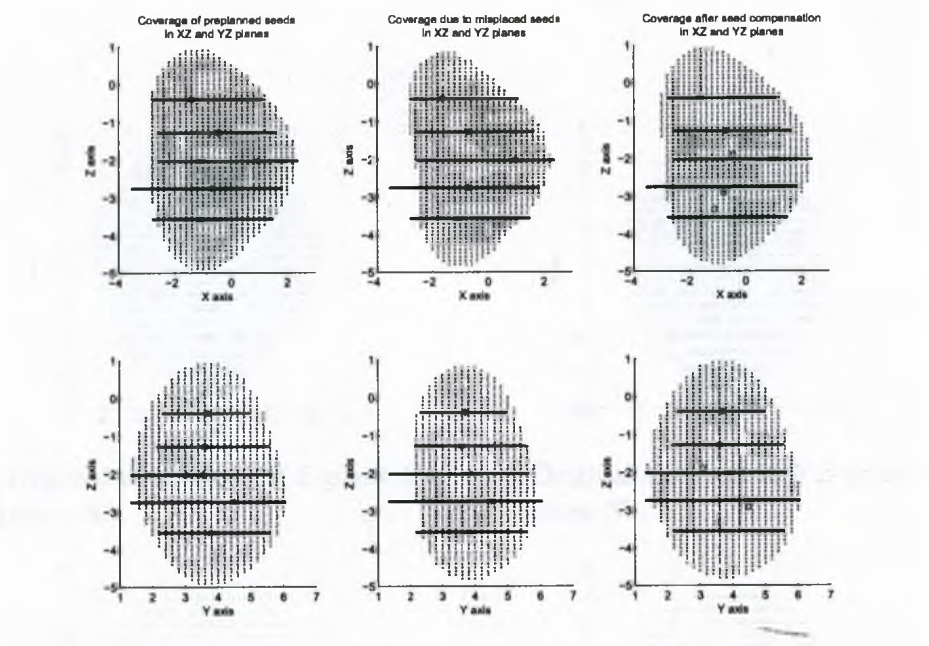

Figure 4.15: Before and after seed compensation for tumor 1 in XZ and YZ-planes

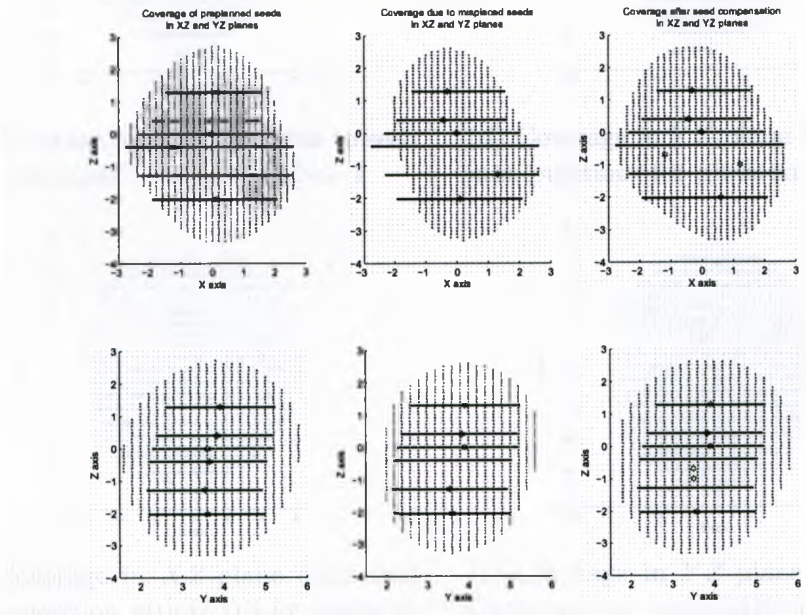

Figure 4.16: Before and after seed compensation for tumor 2 in XZ and YZ-planes

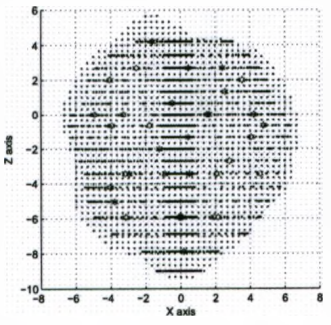

(a) Original coverage in XZ-plane for phantom No. 1

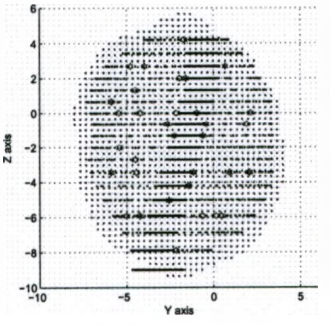

(b) Original coverage in YZ-plane for phantom No. 1

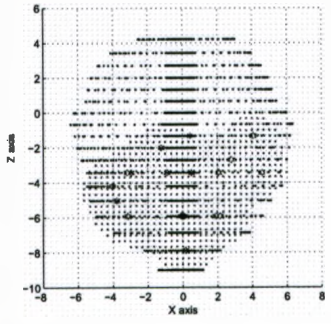

(c) Coverage in XZ-plane due to seed manipulations for phantom No. 1

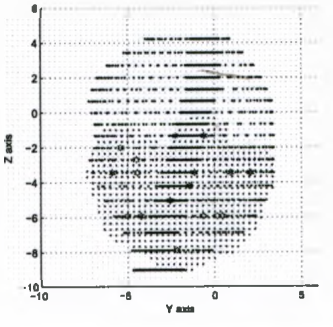

(d) Coverage in YZ-plane due to seed manipulations for phantom No. 1

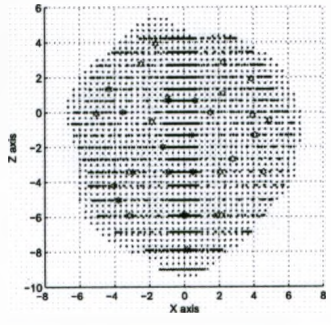

(e) Coverage in XZ-plane after seed compensation with IDDO for phantom No. 1

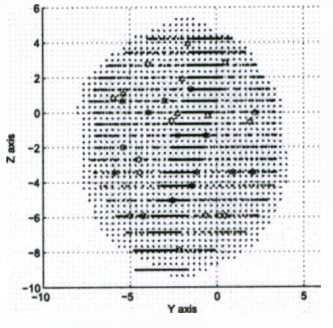

(f) Coverage in YZ-plane after seed compensation with IDDO for phantom No. 1

Figure 4.17: IDDO results for prostate phantom No. 1

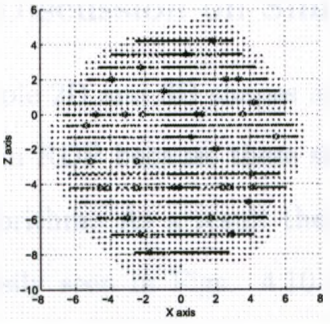

(a) Original coverage in XZ-plane for phantom No. 2

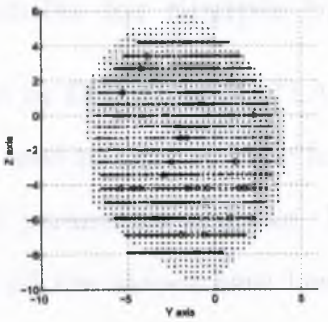

(b) Original coverage in YZ-plane for phantom No. 2

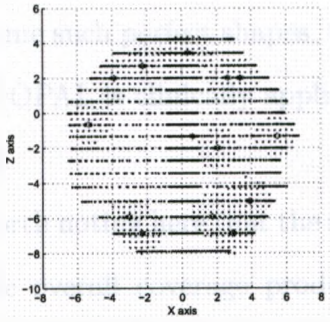

(c) Coverage in XZ-plane due to seed manipulations for phantom No. 2

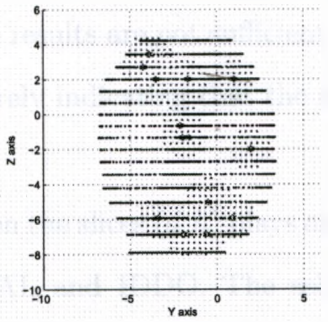

(d) Coverage in YZ-plane due to seed manipulations for phantom No. 2

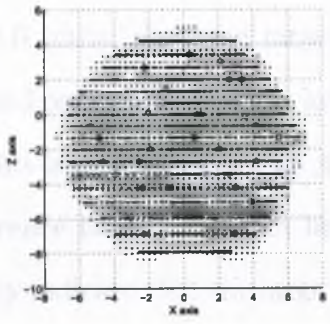

(e) Coverage in XZ-plane after seed compensation with IDDO for phantom No. 2

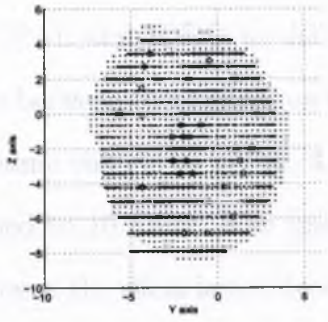

(f) Coverage in YZ-plane after seed compensation with IDDO for phantom No. 2

Figure 4.18: IDDO results for prostate phantom No. 2

4.3 Discussion

4.3.1 Discussion on Simulation Results for Simple Shapes

These simple 2D and 3D shapes are only graphed by DOPAL in MATLAB, nothing was done in RDP because these shapes are only used to test the basic functionality of the algorithm. As a result there are no DVH parameters available. Even so, it can be easily seen in Figs. 4.10 and 4.11 that all the shapes have been properly dosed, since all the 100% radiation coverages appear to cover the entire surface of the planes (Fig. 4.10) or the entire volume (Fig. 4.11). However, realistic tumors will never assume such perfect shapes, therefore these results are not sufficient to indicate whether DOPAL is clinically applicable; it is merely indicating that the algorithm is functional.

It is worth noting here that the spacing between the slices (d_h) plays an important role in the overall coverage produced by DOPAL and IDDO. The selected value for d_h was 2 MATLAB units for the images in Fig. 4.11. It has been verified through experimentation that the algorithms work best with a d_h value of less than 4 MATLAB units, anything larger will force DOPAL and IDDO to deliver dose to the specified contour slices only, leaving the space between these slices un-dosed. The effect of this is illustrated in Fig. 4.19 using the same volume as in Fig. 4.11(b). The only difference here is that d_h has been increased to 10 units. The images in Fig. 4.19 clearly indicate that the large spacing in between the slices is not dosed properly, even though each individual slice has received adequate coverage.

This is not unexpected since the optimization schemes in DOPAL and IDDO have no knowledge of the large spaces in between the slices, for their only concern is to deliver the desired dose to the points provided to them. This implies that to completely dose one entire volume that is composed of well separated slices, the

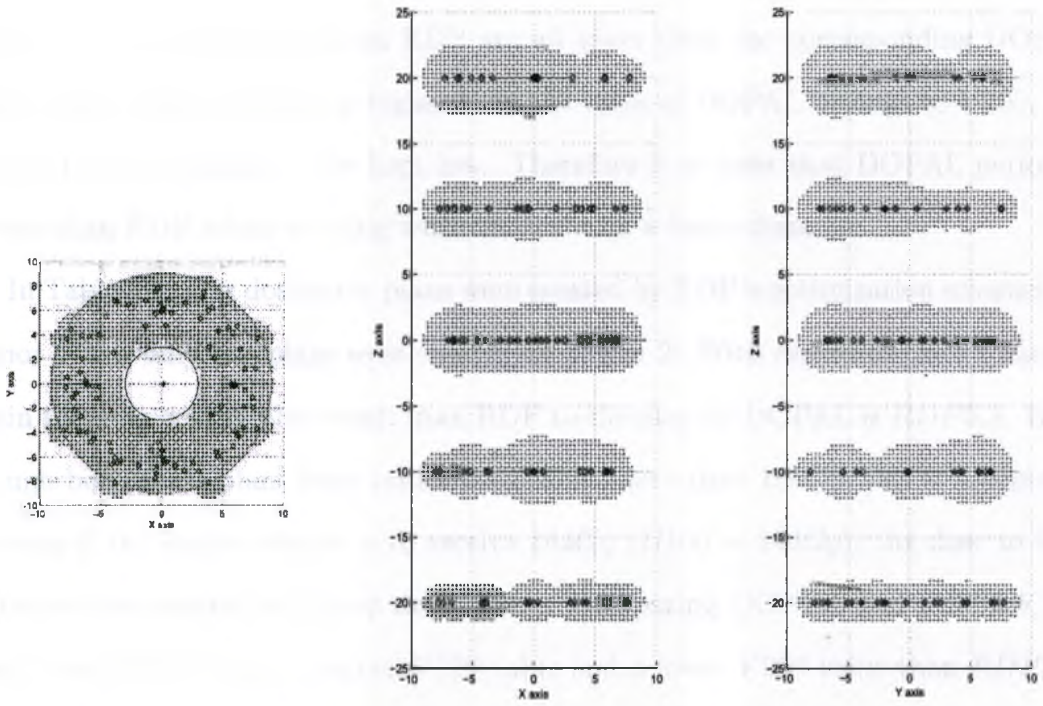

(a) Good coverage in XY-plane

(b) Visible Cold Spots in XZ-plane

(c) Visible Cold Spots in YZ-plane

Figure 4.19: Coverage due to large spacing between slices

contours of the slices have to be traced out at no more than 4 MATLAB units, which converts approximately to less than $15mm$ between slices. This does not affect the experiments, since the spacing between slices in DOPAL can be specified as low as $1mm$, as was mentioned in section 4.1.2.

4.3.2 Discussion on DOPAL for Lung Tumors

In Table 4.1, the majority of RDP's optimization schemes were not able to produce a dosimetry plan, indicated by DNE (Dose Not Exist), while DOPAL was able to produce satisfactory plans for both tumors. Comparing the only result from RDP

($RDP5\_5$) on the second $5mm$ tumor against the DOPAL result on the second tumor, the first three parameters from RDP are all lower than the corresponding DOPAL result. The only value that is higher than the value of DOPAL belongs to $V200$, but this in fact is desirable to be kept low. Therefore it is clear that DOPAL performs better than RDP when working with tumors with a $5mm$ diameter.

In Table 4.2, four dosimetry plans were created by RDP's optimization schemes for tumor 1, but only two plans were created for tumor 2. With regard to the 1^{st} tumor, again the only comparable result from RDP to the plan by DOPAL is $RDP5\_5$. Even though both these plans have values for $D90$ at more than $160Gy$, this is acceptable because if the entire volume is to receive $144Gy$ ($D100 = 144Gy$), the dose to 90% of the volume should be higher than $144Gy$. Comparing $DOPAL$ and $RDP5\_5$, the plan from $DOPAL$ has a higher $V100$ value and a lower $V200$ value than $RDP5\_5$, implying that the DOPAL plan is actually more preferable. As is described in [50], $V100$ is less likely to be affected by seed displacements, so it is better to have a higher value in order to achieve a better coverage. For the 2^{nd} tumor, the $DOPAL$ plan produced better values than both $RDP5\_5$ and $RDP5\_10$ in terms of $V90$, $V100$ and $V200$. A higher percentage volume receiving 90% and 100% of the prescribed dose is always desirable as this implies a more complete coverage, while there should be a lower percentage volume receiving 200% of the prescribed dose to limit radiation to the OAR. $DOPAL$ managed to achieve higher values than the plans from RDP for both $V90$ and $V100$, while a lower value was achieved for $V200$. The plan from DOPAL has a higher $D90$ value than the plans from RDP, but this is still acceptable since the overall radiation is actually 'harming' less tissue than $RDP5\_5$ or $RDP5\_10$ as shown by the $V200$ values. The remaining results from RDP were not comparable to DOPAL's results and therefore they will not be discussed here.

Regarding the results of the first $2cm$ tumor that are displayed in Table 4.3, not

only is RDP capable of producing just 2 valid results, but these results have extremely low values for the $V100$ parameter, no more than 27%. Comparing this, as well as the values of all other parameters to the values shown under $DOPAL$, even though the $V200$ value from $RDP5\_5$ is as low as 12.3%, but the inferior $D90$, $V90$ and $V100$ values mean that the prescribed dose is unlikely to be delivered to the tumor. Therefore, this implies that the pre-plan from DOPAL is better even if the value for $V200$ is higher. As for the second tumor, the plan from DOPAL is very similar to the one produced by $RDP5\_10$. Although $RDP5\_5$ has a considerably better $V100$ value than $DOPAL$, the $V200$ value from this plan is far too high, thereby more likely to cause damage to the OAR than the one from DOPAL. The $V200$ value of the latter is about 25% lower. Like in the case of the $1cm$ tumors, $RDP10\_5$ and $RDP10\_10$ are all too poor compared to DOPAL and are omitted for discussion purposes.

Overall, the proposed pre-planning algorithm - DOPAL, has outperformed most of RDP's optimization schemes, for a range of different sized lung tumors. Not only are most of the dosimetry plans from DOPAL more capable at delivering the desired dose, but they are also less likely to harm other anatomical structures than the corresponding plans from RDP.

4.3.3 Discussion on IDDO for Lung Tumors

Since *isodose3D* from MATLAB has been proven to provide identical coverage to the isodose graphs from RDP (Fig. 4.12), the IDDO algorithm can be verified by visually comparing the XY-plane coverage before and after updating the dosimetry plan with IDDO's output. The figures in the 2^{nd} column of Fig. 4.13 show the slice-by-slice radiation coverage at 100% prescription dose due to manipulated seeds on the $1cm$ tumor, where the 1^{st} figure in that column corresponds to the 1^{st} slice and the last

figure is for the last slice. In this column of figures, slices 3 and 4 show the most significant effect due to seed manipulations, where greater underdosed regions can be observed closer to the boundary of the tumor. This is evident when compared to the same images from the 1^{st} column, which are the 100% radiation coverages from pre-planning. The seeds on these figures also appear to be clustered, but only because the seeds on these slices are viewed all at once in the XY-plane, when in fact every individual slice contains far fewer seeds. The 3^{rd} column in Fig. 4.13 shows the slices after seed compensation with IDDO. Slices 3 and 4 in this column show that the cold spots from the same images from the 2^{nd} column are no longer present, due to the newly deposited seeds as a result of IDDO. The new IDDO seeds are visible upon closer inspection, since the seeds on each slice in the 3^{rd} column in Fig. 4.13 are different from the seeds seen in the previous two columns. The overall coverage shown in the last column is very similar, if not identical, to the original coverage in the first column, which indicates that IDDO is working well for the $1cm$ tumor.

As for the $2cm$ tumor in Fig. 4.14, the most visible effects due to seed manipulations (column 2) are found on slices 4, 5 and 6. Similar to the $1cm$ tumor case before, the 100% prescription dose coverages of slices 4, 5 and 6 in Fig. 4.14 due to seed compensation by IDDO (column 3) show very well compensated coverages since the cold spots that are visible in the manipulated coverage can no longer be seen. Intuitively, for IDDO coverage to be similar to the original coverage, the seed configuration from IDDO should also be similar to the original seed configuration. This is evident when taking a closer look at the seeds present between the original and IDDO configurations, even though the IDDO seeds are a little different from the original seeds, they look very similar indeed.

Column 1 in Fig. 4.15 ($1cm$ tumor) and Fig. 4.16 ($2cm$ tumor) show the pre-planned 100% coverage in the XZ, and YZ planes, while column 2 shows the coverage

due to misplaced seeds and column 3 shows the coverage after seed compensation. These figures indicate that the results for XZ and YZ planes are consistent with those for XY-plane.

4.3.4 Discussion on DOPAL for Prostate Phantoms

With regard to prostate brachytherapy, both [59] and [6] have suggested adequate values in obtaining a robust and optimal dosimetry plan. In [59], the suggested value for $V100$ in the target region (i.e. the prostate and not the urethra) is $> 80\%$, and the suggested value for $D90$ is between 140 to $160Gy$. This matches the value given in [6], in which the recommended value for $D90$ is given as $160Gy$. [6] also suggested that an optimal plan for prostate brachytherapy should result in a value of 40% for $V150$, also for the target region.

Intuitively, the most optimal plan is one that has a $V100$ value of 100% with $V200$ of 0%. Obviously this can only be a 'goal', since it is not realistic for prostate brahchytherapy due to the presence of the urethra, bladder and rectum. The urethra runs through the center of the prostate, and it would receive more dose than the desired 100% prescription dose if the whole prostate itself has actually been delivered $144Gy$ of dose. Therefore the upper dose limit imposed on the urethra in [47] is actually 150%, which resulted in the urethra from half of the test cases receiving more than 120% of the prescribed dose. Although this value is higher than 100%, it is to ensure that the prostate can still receive adequate dosage. Even so, the work in [47] suggested that the dose to the rectum cannot exceed the upper limit of 78%. The violation of this limit is strongly correlated with a high dose on the prostate [47, 61]. It is necessary to mention here that the work in [47] has used an initial source strength of $0.57U$, which is slightly lower than the $1U$ source activity used

for the evaluation of the *ex vivo* lung tumors. To be consistent with the work from [47], the same source strength of $0.57U$ is used for evaluating the DOPAL results for the prostate phantoms. For simplicity, the RDP and DOPAL results regarding the prostate phantom in Table 4.4 and 4.5 are also obtained using a source strength of $0.57U$.

To examine the robustness of the proposed algorithm on prostate phantoms, there are two regions that must be examined, namely, the target region (the prostate) where the full prescription dose should be delivered to the entire volume; and the forbidden region (the urethra) where ideally no dose should be delivered to any part of the region at all. First, from the urethra DVH values in Table 4.5, it can be seen that the $V150$ value for both $RDP5\_5$ and $RDP5\_10$ are well above 30% for tumors 1 and 2. Although for each tumor $RDP5\_5$ and $RDP5\_10$ produced lower values than the corresponding $DOPAL$ result with regards to $D90$, $D100$, $V90$ and $V100$, the $V120$ result of $DOPAL$ is significantly lower than both $RDP5\_5$ and $RDP5\_10$ which is desirbed to be kept low to prevent harming the surrounding OAR. Since it is not possible to prevent the urethra from receiving a substantial amount of dose, it is important that the maximum dose delivered to the urethra should be kept to a minimum, which is described by the $V120$ value. It is safe to say that based on the $V120$ and $V150$ urethra values, DOPAL has performed better than both $RDP5\_5$ and $RDP5\_10$; the remaining two plans from RDP - $RDP10\_5$ and $RDP10\_10$ seem to have outperformed DOPAL with regards to the dosimetric values of the urethra. However, the DVH parameters for the prostate must also be analyzed to determine the effectiveness of $RDP10\_5$ and $RDP10\_10$ versus DOPAL.

In addition, the average urethral dose has been given as 156% as a result of the intra-operative 3D algorithm (I-3D) by [60], this translates to more than $224Gy$ of dose for $D100$ for the urethra. This is not at all desirable and is not comparable to

DOPAL's $D100$, which has been kept below the prescribed dose. Also, [40] presents the data from their research, which shows an average $D30$ for the urethra from 6 patients as $180.72Gy$. In comparison, the average dose delivered to 30% of the urethral volume by DOPAL is $167.7Gy$. Since the urethra is the subject of interest here, it is desirable to have a low value for $D30$. As such, DOPAL also performs better than the method proposed in [40].

In Table 4.4, $RDP10\_5$ and $RDP10\_10$ also show very low values for all the DVH parameters. Even though the low values for $V150$ is desirable, but it can be seen from all the other values that there is hardly any dose delivered to the target volume by these two plans. The maximum volume receiving the full amount of the prescribed dose is from $RDP10\_5$, which is just over 25%. This is not at all comparable to DOPAL's $V100$ at 93.3%. Therfore, $RDP10\_5$ and $RDP10\_10$ are not performing as well as DOPAL is in delivering a good dose to the tumor volume. Furthermore, all parameters under $DOPAL$ show better values than all the other two plans from RDP ($RDP5\_5$ and $RDP5\_10$). For $D100$ and $V100$, which are parameters that should have a high value, the values from $DOPAL$ are much higher than those from RDP, while $V150$, which should be as low as possible, the value under $DOPAL$ is at least 17% lower than its corresponding value from RDP. It can be concluded then that for the prostate phantom, DOPAL has performed much better than RDP.

The $V100$ and $V150$ values from [60] were given respectively as 96% and 71%. This high $V100$ result has been obtained at the expense of increasing dosage to the entire volume. Evidence of this is the high $V150$ value, as well as the high urethral dose at 156% as mentioned previously. In this respect, DOPAL is arguably better than the I-3D algorithm proposed by [60], since DOPAL delivered a relatively high dose to the prostate, while delivered relatively little dose to the urethra. Also, the average $V150$ value for the prostate given by [40] is 70.3%, and the average $V100$

value given is 96%. It can be seen that in terms of the $V100$ parameter alone the algorithm from [40] performs better than DOPAL. However, considering the fact that the average $V100$ value from DOPAL for the prostate is 93.7% (which is very close to 96%), and that the average $V150$ value from DOPAL is 41.5%, and the fact that DOPAL harms the urethra less than the algorithm from [40], in an overall sense the DOPAL algorithm may be better than the proposed algorithm in [40].

Elsewhere, reference [62] reported that an average of 86.34% was achieved for $V100$ of the prostate among data from five treatment centers, which is somewhat inferior to the results produced by DOPAL. Also, $V100$ presented by [63] for the prostate is 95%, while $D100$ is $190Gy$ for the urethra. The $V100$ for the prostate from this work is slightly higher than the result from DOPAL, however the urethral $D100$ result from DOPAL ($\approx 120Gy$) is significantly lower and thus better than the one from [63].

The results for Lee *et al.*'s work on prostate dosimetry planning are given in [47], in which it is stated that 93% of the prescribed dose was delivered to the gland, which can be intepreted as $V93 = 100\%$, as shown in Table 4.4. Reference [47] also stated that 50% (total of 15 patients) of the urethra received more than 120% of the prescribed dose on average, with the range of the dose delivered to the urethra being 100% to 150%. This can be intepreted as $V120 > 50\%$ for the urethra, which is shown in Table 4.5. Since these are the only values that are explicitly provided by [47], it is not possible to perform a complete comparison between DOPAL and Lee's work. For the available values that are shown in Table 4.4, the results from Lee's work appear to have a slight advantage over DOPAL, their $V93$ value is less than 5% better than the $V93$ value of DOPAL. On the other hand, no information is given regarding how Lee's algorithm performed in terms of $D90$ and $V100$, but it can be seen that the $D90$ results from DOPAL are within the suggested $140Gy$ to $160Gy$ range, while the $V100$

results are well above the suggested adequate 80% mark. In terms of the prostate alone, even though DOPAL did not perform as well as Lee's algorithm did for $V93$, they are still good dosimetry plans overall.

The urethra comparison against Lee's work has to rely on the $V120$ results only. In [47], more than 50% of the urethra volume received 120% of the prescribed dose, whereas the values under $DOPAL$ are at least 30% lower as shown in Table 4.5. The one concern for the results in this table is that the results from Lee's work were based on 15 patients, while DOPAL's results were from two prostate phantoms. It might be a possibility that values for $V120$ will increase as more data is collected; however, the consistency shown by the values from the prostate DVH parameters, as well as the $V120$ and $V150$ values for the urethra is a sign that similar results to those shown in Table 4.5 would be produced even when DOPAL is tested on a number of test subjects.

It was also mentioned in [6] that an optimal use of the brachytherapy sources should result in a value of 40% for $V150$ and $160Gy$ for $D90$, for the prostate. The DOPAL results shown in Table 4.4 show that the $D90$ values for the two phantoms are at $150.9Gy$ and $153.1Gy$, while the $V150$ values are at 40.8% and 42.3%. These DOPAL values are very close to the values suggested in [6].

Overall, it can be concluded that DOPAL is comparable to Lee's MIP based dosimetry planning algorithm, if not better. The urethra is clearly receiving much less dose with the dosimetry plan from DOPAL, even though 93% of the prescribed dose isn't delivered to as much of the target volume as Lee's algorithm did.

4.3.5 Discussion on IDDO for Prostate Phantoms

The IDDO results for the 1^{st} prostate phantom is shown in Fig. 4.17, which shows the pre-planned 100% prescription coverage in the first row, 100% coverage due to seed manipulations in the second row, and 100% coverage after seed compensation with IDDO in the third row. As mentioned in section 4.2.4, the IDDO compensation results in this figure (4.18(e), (f)) are obtained by using a *tol_val*= ±5%, which means that the new upper limit is now 5% more than the upper limit of the pre-planning seeds, while the new lower limit is 5% lower than the lower limit of the pre-planning seeds. As shown in Fig. 4.18(c) and Fig. 4.18(d), only seeds in the bottom half of the prostate have been kept in their original positions. Upon closer inspection, the seeds (which are hexagons in the figures) after running IDDO compensation are different from those from pre-planning, even though the compensated coverages are almost identical to the original coverage, even at places where a slight overdose is visible. This further confirms that IDDO is working well, since a *tol_val*= 5% has been specified prior to running the algorithm, the desired outcome of which is a compensated coverage of no more and no less than 5% of the original coverage.

For the 2^{nd} phantom (Fig. 4.18), the seeds have been manipulated differently from those in the 1^{st} phantom, where the seeds have been kept on various slices throughout the volume and not just on the bottom half. Furthermore, U_b and L_b values on the target and forbidden regions have been specified manually in IDDO to obtain the compensated coverages shown in Fig. 4.18(e) and (f), meaning that a *tol_val* was not in place. These has been done purposefully to show that the IDDO algorithm is working for another scenario than the in the 1^{st} phantom. Although the compensated coverages at 100% prescribed dose in Fig. 4.18 still closely resemble the original 100% coverages, the overdosed regions on the top and bottom slices seen in Fig. 4.18(a)

and (b) are no longer visible in Fig. 4.18(e) and (f). This can be easily explained since a *tol_val* was not used for this phantom, such that the seed compensation of IDDO no longer focuses on delivering the same dose to the entire volume as the dose from pre-plan, rather its concern now is to deliver the dose according to the new U_b and L_b specified by the user. Evidently, IDDO is working fine with or without *tol_val*; however one can argue that it might be better to include *tol_val* in IDDO. Simply because in Fig. 4.17(a) and (a) the pre-planning seeds already provided a good coverage.

In Fig. 4.18(e), the bottom slice is covered but not the space below it. This space refers to the completeness of the prostate volume, and even though the space below the bottom slice in Fig. 4.18(a) dose not seem to be properly covered either, at least the two ends of the coverage are more prostate-like than those displayed in Fig. 4.18(e) and (f). Nonetheless, the IDDO algorithm itself is proven to be fully functional and produces the desired coverage to the tumor volume given to it. Supplying the IDDO algorithm with a more complete description of the tumor volume would most likely resolve the issue mentioned above regarding the un-dosed space below the bottom slice.

Chapter 5

Conclusion and Future Work

In this chapter, the sources of error that affected the accuracy of the results of this research are first discussed. Then in section 5.2, the various areas that require further work are discussed. Concluding remarks are given in section 5.3.

5.1 Sources of Error

One source of error in this work comes from the slight discrepancies observed when comparing Fig. 4.12(a) and (b). These are due to differences in the dose calculation formulas employed by RDP and DOPAL. In the implementation of DOPAL, an inverse squared method has been used to calculate the dose delivered to various points. In particular, the dose calculation in DOPAL is based on the point source approximation suggested by [5], which has also been used by Lee *et al.* [18] in their research. It is not clear what is the exact formula used by RDP as it is a commercial and proprietary package. This uncertainty is the likely cause of the offset observed in Fig. 4.12. Reference [5] discusses the possible cause of this offset, which is likely due to the values of the parameters involved in Eq. (2.5). It was noted in [5] that although it is sufficient to approximate the dose using the point source formula, it might lead to errors in the range of 3% to 9%.

Another source of error is with regard to the values presented in Tables 4.4 and 4.5 for the prostate and urethra pre-planning results, because the DVH values of the

DOPAL plans from these tables have been obtained using different methods from Lee's plans. RDP was used to obtain the DVH values for the DOPAL plans, which are then compared against Lee's DVH values, even though there is no indication as to how the DVH values in Lee's work in [47] have been obtained. On the other hand, it is justified to use RDP to obtain the DVH values for the plans generated by both RDP and DOPAL in Tables 4.1 to 4.5, because the DVH values from DOPAL are compared against those from RDP. Other than the fact that obtaining the DVH values from a commercial software such as RDP provided a certain degree of validity, it would have been better to have known the seed locations from [47] instead of the DVH values, so that the seeds from both DOPAL and [47] can be plotted in RDP and their corresponding DVH values can be obtained using the same program to minimize any discrepancies.

This led to another error for the results in these tables, which is the lack of knowledge of the prostate volume used by Lee in [47]. The results from [47] have been obtained from a wide range of test subjects, the prostate volume in these studies are likely to be of various shapes and sizes. As was shown by the DOPAL results for the two prostate phantoms in this thesis, the DVH parameters for each prostate phantom are different. So, without knowing the exact volume and shape of the test subjects used by [47], the results displayed in Tables 4.4 and 4.5 may not provide an objective comparison.

5.2 Future Work

One area of improvment that can be done in the future is to test the DOPAL and IDDO algorithms in the *ex vivo* environment for the lung, kidney and other organs in the presence of forbidden regions that have a more complex shape than the urethra.

The algorithms should work very well regardlessly of the shapes of the forbidden regions, but tests are still planned to get a qualitative and quantitative feedback.

As was mentioned in section 4.3.4, the results in [47] from Lee's dosimetry planning algorithm has been tested on prostate data from 15 patients. In contrast, the DOPAL algorithm proposed in this thesis has been verified on two sets of prostate data only. Despite the reasonable results shown in Table 4.4 and Table 4.5, not enough results were available to make a statistical comparison with Lee's approach. Also, it was not possible to draw conclusions about robustness of the algorithm by comparing only two sets of DVH values ($V93$ for the target and $V120$ for the urethra), which are the only values provided by [47]. A robust algorithm is one that can deliver a high dose to the target and low dose to the other organs such as the urethra, bladder, or rectum. An overall better (more robust) algorithm can only be determined by performing dosimetry planning using DOPAL on a number of test subjects, as well as comparing DVH values from both algorithms that cover a greater variety of aspects. This is planned for future work.

Another concern is related to the induced edema upon needle tissue interaction. Edema is the abnormal accumulation of fluid beneath the skin, which may occur when brachytherapy needles penetrate the skin to deposit seeds. This edema might even cause the tumor size to change during seed implantation, thus reducing the degree of accuracy of the dosimetry plan. If IDDO does not account for edema either, its accuracy would be reduced as well. So the correct modeling of induced edema can further improve the overall accuracy in brachytherapy.

Also, both DOPAL and IDDO currently work with only one type of seed – ^{125}I, or ^{103}Pd, but not both. It might be beneficial to expand the algorithms to use multiple sources in the future, which could involve the expansion of the dose calculation module to take into consideration the irradiation and interaction of two or more types of seeds.

From an optimization point-of-view, even though good results were obtained for dosimetry planning and seed compensation, the solutions to DOPAL and IDDO are not globally-optimal. For example, the location of the initial seed *temp_seed* affects the outcome of the final seed configuration. In Fig. 4.10 for the 2D results, the COM value was used as the initial *temp_seed* location. However, if a very different location was used as the initial *temp_seed* value, e.g., one on the boundary of the contour slice, then the final seed configuration would be different to those shown in Fig. 4.10. Therefore, although DOPAL's DVH values and IDDO's radiation coverage all showed good results with sub-optimal results, this is a potential drawback for these algorithms.

MIP might provide a global solution to these optimization problems, however the discretized solution space might also reduce the accuracy that DOPAL and IDDO currently possess. On the other hand, as was mentioned in [18], the solution to the dosimetry planning problem might never satisfy all constraints. In other words, the global solution may not exist for such a problem. And even if a global solution can be found, it might take too long to arrive at that solution. It is worth noting here again that one focus of the DOPAL algorithm is to address the problems that resulted from time delay between pre-operative image-based planning and the implantation stage. So as long as the currently sub-optimal solutions from the algorithms can be proven to be clinically acceptable, it is still more advantageous over a time-consuming globally optimal solution. Nevertheless, future work is planned in upgrading the current algorithm implementation if a method can be found that provides an optimal trade-off between the size of the solution space and the speed to arrive at a solution.

Finally, precise contouring of the implanted tumors using US images was sometimes difficult, as was the case with *ex vivo* lung tumors, where the vessels and air ducts made contouring of the tumor difficult even if the lung had already been col-

lapsed. However, the US images have only been used to compare pre-planning results from DOPAL with the results from RDP, so there are options of employing other high quality imaging modalities in the future for contouring, such as x-ray. Furthermore, experimental *in vivo* testing on animal models is planned for the near future.

5.3 Concluding Remarks

In summary, this thesis presented the development of a dosimetry pre-planning algorithm (DOPAL) and an intra-operative dynamic dose optimization algorithm (IDDO), which can be used in a robot-assisted brachytherapy procedure for the prostate, lung and other organs. In the proposed algorithms, there are no pre-defined shapes for which they can work with. Thus although the focus of this thesis has been on the lung and the prostate, the algorithms have actually been designed to work with a range of cancer tumors. Even though commercial software can also be used in a robot-assisted brachytherapy procedure, the results in section 4.2.3 and 4.2.4 clearly show that they cannot provide the accuracy comparable with those from DOPAL and IDDO.

The main achievement of DOPAL is on-line real-time dosimetry planning. In doing so, two potential sources of error linked with the current brachytherapy method are addressed. The first error is related to the reduced accuracy of the dosimetry plan from the time of its creation to the time of its use. In the current brachytherapy procedure, especially with regard to the prostate, there is a long waiting time (usually several weeks) between the pre-plan and the seed implantation. The tumor's size is likely to have been enlarged by the time seed implantation takes place, making the pre-plan not as accurate anymore. DOPAL is able to perform dosimetry planning right before seed implantation, so the pre-plan produced by DOPAL is based on the

shape of the tumor at seed implantation, thereby making the pre-plan as accurate as it can possibly be.

The second issue is also related to the accuracy of the pre-plan, this time due to errors in the images used for pre-planning and seed implantation. In the current procedure, dosimetry planning is performed based on images acquired during pre-operative imaging with the patient in lithotomy position. When seed implantation takes place (based on the dosimetry plan created), the patient is again placed in lithotomy position but most likely not in the exact same way. Due to this difference in how the patient has been placed between the pre-operative imaging stage and the seed implantation stage, the images for the dosimetry plan are going to be different from those for seed implantation. Thus, the intended locations from the dosimetry plan could be inaccurate. DOPAL is able to perform dosimetry planning in real-time, meaning that the exact same images that are used for dosimetry planning are also used for seed implantation. Therefore, making the pre-plan more accurate than the current method.

In addition, the upper and lower limits of the dose delivered to the target volume can be adjusted as required. So in the event that a different dose needs to be administered to a particular organ, the desired dose can be separately specified for each of the organs present, such as the case for the prostate tumor, where the imposed U_b and L_b on the urethra and prostate were given different values from each other to obtain a high dose to the prostate but a low dose to the urethra. In reference [47], a similar approach is also described. In contrast, commercial software such as RDP does not offer this flexibility, which might have lead to the poor dosimetry results in Tables 4.4 and 4.5. In these tables, the urethral dose from RDP are as high as the prostate dose, when in fact the dose to the urethra should have been much lower.

The main achievement of IDDO lies with the real-time compensation for seed

misplacements. As mentioned earlier in this thesis, seed misplacements may occur due to inaccurate seed deposition by the physician or robot. If the remaining seeds are still deposited according to their original plan, the overall coverage of the tumor is going to be different from the intended coverage as a result of these misplacements. IDDO is able to compensate for any seed deviations from their intended locations by generating new locations for the remaining seeds, such that the overall coverage at the end of the procedure is as close to the intended coverage as possible.

Similar to RDP, both DOPAL and IDDO also provide the option to exchange the type of seeds to be implanted, for instance between ^{125}I or ^{103}Pd, or even amongst different types of ^{125}I. Each type of seed has different radiation properties, and thus the values involved in dose calculation are also different. These values for the chosen seed type for this thesis, type 6711 of ^{125}I, have all been stored in an individual file which can be called-upon when performing dose calculation. These values are given in Appendix B for reference. There are no limits on the number of seed types that DOPAL and IDDO can work with, accurate results can be obtained as long as there is a file that contains the values of the corresponding radiation parameters.

The algorithms can be used as stand-alone components or they can be used together. Either use of the algorithms must be accompanied by a robot-assisted brachytherapy set-up, one such set-up is the AESOP which was described in section 4.1.1.2. The aim of either use is to minimize the errors present in the current brachytherapy procedures and to improve the overall radiation coverage results. The algorithms have been tested experimentally using artificial tumors of different sizes embedded in *ex vivo* porcine lung tissue and prostate phantoms. The outcome of the tests have shown superior performance in comparison with a commercially available software.

Bibliography

[1] J. J. Stein and S. R. Baker, "Radiation therapy of cancer," *Cancer Studies*, vol. 102, no. 5, pp. 370–375, 1965.

[2] P. Bownes and A. Flynn, "Prostate brachytherapy: A review of current practice," *J of Radiotherapy in Practice*, vol. 4, pp. 86–101, 2004.

[3] A. T. Porter, J. C. Blasko, P. D. Grimm, S. M. Reddy, and H. Ragde, "Brachytherapy for prostate cancer," *CA Cancer J Clin*, vol. 45, pp. 165–178, 1995.

[4] J. Robinson, "Verification of direct brachytherapy dosimetry for a single seed implant," Master's thesis, Louisiana State University, 1984.

[5] R. Nath *et al.*, "Dosimetry of interstitial brachytherapy sources: Recommendations of the AAPM radiation therapy committee Task Group No. 43," *Int J Med Phys Res and Prac*, vol. 22, pp. 209–234, 1995.

[6] R. S. Kirby, A. W. Partin, J. K. Parsons, and M. R. Feneley, *Treatment Methods for Early and Advanced Prostate Cancer.* Informa Healthcare, 2008.

[7] D. Baltas, L. Sakelliou, and N. Zamboglou, *The Physics of Modern Brachytherapy for Oncology.* Taylor & Francis, 2007.

[8] R. Nath and A. Melillo, "Dosimetric characteristics of a double wall ^{125}I source for interstitial brachytherapy," *Medical Physics*, vol. 20, no. 5, pp. 1475–1483, 1993.

[9] P. M. Devlin, *Brachytherapy Applications and Techniques.* Lippincott Williams & Wilkins, 2007.

[10] H. Hricak and P. T. Scardino, *Prostate Cancer.* Cambridge University Press, 2009.

[11] C. Bangard, R. Semrau, H. Bovenschulte, and K. J. Lackner, "Percutaneous fluoroscopically guided salvage of misplaced perirectal ^{125}I prostate seeds – easy way out," *J Urol*, vol. 74, no. 4, pp. 924 – 925, 2009.

[12] S. Nag, J. P. Ciezki, and R. Cormack, "Intraoperative planning and evaluation of permanent prostate brachytherapy: Report of the American Brachytherapy

Society," *International Journal of Radiation Oncology Biology Physics*, vol. 51, no. 5, pp. 1422–1430, 2001.

[13] G. W. Ma, M. Pytel, A. L. Trejos, V. Hornblower, J. Smallwood, R. Patel, A. Fenster, and R. A. Malthaner, "Robot-assisted thoracoscopic brachytherapy for lung cancer: Comparison of the ZEUS robot, VATS, and manual seed implantation," *Computer Aided Surgery*, vol. 12, no. 5, pp. 270–277, 2007.

[14] A. L. Trejos, A. W. Lin, M. P. Pytel, R. V. Patel, and R. A. Malthaner, "Robot-assisted minimially invasive lung brachytherapy," *Int J Med Robot Comput Assist Surg*, vol. 3, pp. 41–51, 2007.

[15] "Canadian cancer statistics 2010, special topic: End-of-life care."

[16] A. Jermal, R. Siegel, J. Xu, and E. Ward, "Cancer statistics, 2010," *CA Cancer J Clin 2010*, 2010.

[17] D. M. Parkin, F. Bray, J. Ferlay, and P. Pisani, "Global cancer statistics, 2002," *CA Cancer J Clin*, vol. 55, pp. 74–108, 2005.

[18] E. K. Lee, R. J. Gallagher, D. Silvern, C. S. Wuu, and M. Zaider, "Treatment planning for brachytherapy: An integer programming model, two computational approaches and experiments with permanent prostate implant planning," *Physics in Medicine and Biology*, vol. 44, no. 1, pp. 145–165, 1999.

[19] B. S. Barringer, "Radium in the treatment of cancer of the bladder and prostate," *J Am Med Assoc*, vol. 68, pp. 1227–1230, 1917.

[20] H. H. Holm, "The history of interstital brachytherapy of prostate cancer," *Semin Surg Oncol*, vol. 13, pp. 431–437, 1997.

[21] W. F. Whitemore Jr, B. Hilaris, and H. Grabstald, "Retropubic implantation to iodine 125 in the treatment of prostatic cancer," *J Urol*, vol. 108, no. 6, pp. 918–920, 1972.

[22] J. J. Battermann, T. A. Boon, and H. J. de Voogt, "Preliminary results with iodine-125 seeds for permanent implantation in patients with localized prostatic cancer," *Radiother Oncol*, vol. 10, no. 2, pp. 91–95, 1987.

[23] M. J. Zelefsky and W. F. Whitmore Jr., "Long-term results of retropubic permanent 125-iodine implantation of the prostate for clinically localized prostatic cancer," *J Urol*, vol. 158, no. 1, pp. 23–29, 1997.

[24] H. Ragde, G. L. Grado, and B. S. Nadir, "Brachytherapy for clinically localized prostate cancer: Thirteen-year disease-free survival of 769 consecutive prostate

cancer patients treated with permanent implants alone," *Arch Esp Urol*, vol. 54, no. 7, pp. 739–747, 2001.

[25] L. Gomella, G. Merrick, R. K. Valicenti, and F. Waterman, *Basic and Advanced Techniques in Prostate Brachytherapy.* Taylor & Francis, 2005.

[26] D. G. French, "Real-time dosimetry for prostate brachytherapy using TRUS and Fluoroscopy," Master's thesis, The University of British Columbia, Dec. 2004.

[27] G. Cheng, H. Liu, L. Liao, and Y. Yu, "Dynamic brachytherapy of the prostate under active image guidance," in *Medical Image Computing and Computer-Assisted Intervention MICCAI 2001*, ser. Lecture Notes in Computer Science, W. Niessen and M. Viergever, Eds. Springer Berlin / Heidelberg, 2001, vol. 2208, pp. 351–359.

[28] Z. Wei, M. Ding, D. Downey, and A. Fenster, "3D TRUS guided robot assisted prostate brachytherapy," in *Medical Image Computing and Computer-Assisted Intervention MICCAI 2005*, ser. Lecture Notes in Computer Science, J. Duncan and G. Gerig, Eds. Springer Berlin / Heidelberg, 2005, vol. 3750, pp. 17–24.

[29] ——, "Dynamic intraoperative prostate brachytherapy using 3D TRUS guidance with robot assistance," in *Engineering in Medicine and Biology Society, 2005. IEEE-EMBS 2005. 27th Annual International Conference of the*, Jan. 2005, pp. 7429 –7432.

[30] H. M. Ladak, F. Mao, Y. Wang, D. B. Downey, D. A. Steinman, and A. Fenster, "Prostate boundary segmentation from 2D ultrasound images," *Medical Physics*, vol. 27, no. 8, pp. 1777–1788, 2000.

[31] Y. Wang, H. N. Cardinal, D. B. Downey, and A. Fenster, "Semiautomatic three-dimensional segmentation of the prostate using two-dimensional ultrasound images," *Medical Physics*, vol. 30, no. 5, pp. 887–897, 2003.

[32] M. Ding, L. Gardi, Z. Wei, and A. Fenster, "3D TRUS image segmentation in prostate brachytherapy," in *Engineering in Medicine and Biology Society, 2005. IEEE-EMBS 2005. 27th Annual International Conference of the*, 2005, pp. 7170 –7173.

[33] L. Potters, E. Calguaru, K. B. Thornton, T. Jackson, and D. Huang, "Toward a dynamic real-time intraoperative permanent prostate brachytherapy methodology," *Brachytherapy*, vol. 2, no. 3, pp. 172 – 180, 2003.

[34] R. G. Stock, N. N. Stone, M. F. Wesson, and J. K. DeWyngaert, "A modified technique allowing interactive ultrasound-guided three-dimensional transperineal prostate implantation," *International Journal of Radiation Oncology Biology Physics*, vol. 32, no. 1, pp. 219 – 225, 1995.

[35] G. K. Edmundson, N. R. Rizzo, M. Teahan, D. Brabbins, F. A. Vicini, and A. Martinez, "Concurrent treatment planning for outpatient high dose rate prostate template implants," *International Journal of Radiation Oncology Biology Physics*, vol. 27, no. 5, pp. 1215 – 1223, 1993.

[36] R. A. Cormack, C. M. Tempany, and A. V. D'Amico, "Optimizing target coverage by dosimetric feedback during prostate brachytherapy," *International Journal of Radiation Oncology Biology Physics*, vol. 48, no. 4, pp. 1245 – 1249, 2000.

[37] H. Bassan, R. V. Patel, and M. Moallem, "A novel manipulator for percutaneous needle insertion: Design and experimentation," in *IEEE/ASME Trans. Mechatron.*, Nov. 2008, accepted for publication.

[38] N. Abolhassani, R. Patel, and F. Ayazi, "Needle control along desired tracks in robotic prostate brachytherapy," in *Systems, Man and Cybernetics, 2007. ISIC. IEEE International Conference on*, Oct. 2007, pp. 3361 –3366.

[39] D. French, J. Morris, M. Keyes, and S. Salcudean, "Real-time dosimetry for prostate brachytherapy using TRUS and Fluoroscopy," in *Medical Image Computing and Computer-Assisted Intervention MICCAI 2004*, ser. Lecture Notes in Computer Science, C. Barillot, D. R. Haynor, and P. Hellier, Eds. Springer Berlin / Heidelberg, 2004, vol. 3217, pp. 983–991.

[40] D. Y. Song, A. K. Jain, Z. Zhang, A. Deguet, Y. Le, E. Armour, E. C. Burdette, and G. Fichtinger, "Dynamic intraoperative dosimetry for prostate brachytherapy using a nonisocentric C-arm," *Brachytherapy*, vol. In Press, Corrected Proof, pp. –, 2010.

[41] D. A. Todor, M. Zaider, G. N. Cohen, M. F. Worman, and M. J. Zelefsky, "Intraoperative dynamic dosimetry for prostate implants," *Physics in Medicine and Biology*, vol. 48, no. 9, p. 1153, 2003.

[42] Y. Chen, R. E. Stanton, R. J. Holst, C. D. Koprowski, and E. B. Krisch, "Treatment planning for prostate implant with loose seeds," *Medical Physics*, vol. 24, no. 7, pp. 1141–1145, 1997.

[43] S. Yoo, M. E. Kowalok, B. R. Thomadsen, and D. L. Henderson, "Treatment planning for prostate brachytherapy using region of interest adjoint functions and a greedy heuristic," *Physics in Medicine and Biology*, vol. 48, no. 24, p. 4077, 2003.

[44] R. Alterovitz, "Planning and optimization algorithms for image-guided medical procedures," Ph.D. dissertation, University of California, Berkeley, Sept 2006.

[45] Y. Yu and M. C. Schell, "A genetic algorithm for the optimization of prostate implants," *Medical Physics*, vol. 23, no. 12, pp. 2085–2091, 1996.

[46] R. R. Meyer, W. D. D'Souza, M. C. Ferris, and B. R. Thomadsen, "MIP models and BB strategies in brachytherapy treatment optimization," *Journal of Global Optimization*, vol. 25, pp. 23–42, 2003.

[47] E. K. Lee and M. Zaider, "Intraoperative dynamic dose optimization in permanent prostate implants," *International Journal of Radiation Oncology Biology Physics*, vol. 56, no. 3, pp. 854–861, 2003.

[48] A. L. Trejos, S. Mohan, H. Bassan, A. W. Lin, A. Kashigar, R. V. Patel, and R. A. Malthaner, "An experimental test-bed for robot-assisted image-guided minimally invasive lung brachytherapy," in *IEEE/RSJ International Conference on Intelligent Robots and Systems, 2007. IROS 2007*, San Deigo, CA, USA, Oct. 2007, pp. 392 –397.

[49] A. L. Trejos, R. V. Patel, and R. A. Malthaner, "A device for robot-assisted minimally-invasive lung brachytherapy," in *IEEE International Conference on Robotics and Automation, 2006. ICRA 2006*, Orlanda, FL, USA, May 2006, pp. 4187–4192.

[50] A. L. Trejos, A. W. Lin, S. Mohan, H. Bassan, C. Edirisinghe, R. V. Patel, C. Lewis, E. Yu, A. Fenster, and R. A. Malthaner, "MIRA V: An integrated system for minimally invasive robot-assisted lung brachytherapy," in *IEEE International Conference on Robotics and Automation, 2008. ICRA 2008*, Pasadena, CA, USA, May 2008, pp. 2982–2987.

[51] J. Pisch, S. J. Belsley, R. Ashton, L. Wang, R. Woode, and C. Connery, "Placement of ^{125}I implants with the da Vinci robotic system after video-assisted thoracoscopic wedge resection: A feasibility study," *International Journal of Radiation Oncology Biology Physics*, vol. 60, no. 3, pp. 928 – 932, 2004.

[52] C. C. Ling, M. C. Schell, E. D. Yorke, B. B. Palos, and D. O. Kubiatowicz, "Two-dimensional dose distribution of ^{125}I seeds," *Medical Physics*, vol. 12, 1985.

[53] G. H. Hartmann, W. Schlegel, and H. Scharfenberg, "The three-dimensional dose distribution of ^{125}I seeds in tissue," *Physics in Medicine and Biology*, vol. 28, no. 6, pp. 693–699, 1983.

[54] E. K. Lee and M. Zaider, "Mixed integer programming approaches to treatment plannign for brachytherapy - application to permanent prostate implants," *An Operations Res Optimiza Med*, vol. 119, pp. 147–163, 2003.

[55] G. L. McCreery, A. L. Trejos, M. D. Naish, R. V. Patel, and R. A. Malthaner, "Feasibility of locating tumours in lung via kinaesthetic feedback," in *Int J Med Robot Comput Assist Surg*, vol. 4, 2008, pp. 58–68.

[56] C. I. Henschke, D. F. Yankelevitz, D. M. Libby, M. W. Pasmantier, J. P. Smith, and O. S. Miettinen, "Survival of patients with stage I lung cancer detected on CT screening," *N Engl J Med*, vol. 355, pp. 1763–1771, 2006.

[57] H. S. Bassan, "Design, construction and control of a micro manipulator for prostate brachytherapy," Ph.D. dissertation, The Univeristy of Western Ontario, London, Ontario, Canada, 2007.

[58] D. C. Beyer, F. Puente, K. L. Rogers, and E. M. Gurgoze, "Prostate brachytherapy: Comparison of dose distribution with different ^{125}I source designs," *Radiology*, vol. 221, pp. 623–627, 2001.

[59] C. Wuu, R. D. Ennis, P. B. Schiff, E. K. Lee, and M. Zaider, "Dosimetric and volumetric criteria for selecting a source activity and a source type (^{125}I or ^{103}Pd) in the presence of irregular seed placement in permanent prostate implants," *International Journal of Radiation Oncology Biology Physics*, vol. 47, no. 3, pp. 815–820, 2000.

[60] M. J. Zelefsky, Y. Yamada, G. Cohen, E. S. Venkatraman, A. Y. C. Fung, E. Furhang, D. Silvern, and M. Zaider, "Postimplantation dosimetric analysis of permanent transperineal prostate implantation: Improved dose distributions with an intraoperative computer-optimized conformal planning technique," *International Journal of Radiation Oncology Biology Physics*, vol. 48, no. 2, pp. 601 – 608, 2000.

[61] R. J. Gallagher and E. K. Lee, "Mixed integer programming optimization models for brachytherapy treatment planning," in *Proc AMIA Annu Fall Symp*, 1997, pp. 278–282.

[62] W. S. Bice, B. R. Prestidge, P. D. Grimm, J. L. Friedland, V. Feygelman, M. Roach, J. J. Prete, D. F. Dubois, and J. C. Blasko, "Centralized multi-institutional postimplant analysis for interstitial brachytherapy," *International Journal of Radiation Oncology Biology Physics*, vol. 41, pp. 921–927, 1998.

[63] G. S. Merrick, W. M. Butler, A. T. Dorsey, and J. H. Lief, "Potential role of various dosimetric quality indicators in prostate brachytherapy," *International Journal of Radiation Oncology Biology Physics*, vol. 44, no. 3, pp. 717 – 724, 1999.

[64] (2009, Feb.) Prostate cancer canada website. [Online]. Available: http://www.prostatecancer.ca/english/prostate_owners_manual/psa

[65] R. S. Kirby, T. J. Christmas, and M. K. Brawer, *Prostate Cancer*, 2nd ed. Mosby, 2001.

[66] (2010, Oct.) National cancer institute. [Online]. Available: http://www.cancer.gov/cancertopics/factsheet/Detection/PSA/

[67] (2005, Oct.) Newsmax. [Online]. Available: http://archive.newsmax.com/archives/articles/2005/10/28/91724.shtml

[68] (2010, Dec.) BBC News - Index finger length prostate cancer clue. [Online]. Available: http:/www.bbc.co.uk/news/health-11880415

[69] J. Subramanian and R. Govindan, "Lung cancer in never smokers: A review," *Journal of Clinical Oncology*, vol. 25, no. 5, pp. 561–570, 2007.

[70] P. Rubin and J. T. Hansen, *TNM Staging Atlas.* Wolters Kluwer, Lippincott Williams & Wilkins, 2008.

[71] C. F. Mountain, H. I. Libshitz, and K. E. Hermes, *Lung Cancer, A Handbook for Staging, Imaging and Lymph Node Classification.* Houston, TX: Charles P Young Company, 1999.

[72] C. F. Mountain, "Revisions in the international system for staging lung cancer," *Chest*, vol. 111, no. 6, pp. 1710–1717, 1997.

[73] M. Abdel-Wahab and O. E. Silva, *Prostate Cancer, A Practical Guide.* Saunders Elsevier, 2008.

[74] K. Arshak and O. Korostynska, *Advanced Materials and Techniques for Radiation Dosimetry.* Artech House, 2006.

[75] M. G. Stabin, *Radiation Protection and Dosimetry: An Introduction to Health Physics.* Springer, 2008.

[76] A. Martin and S. Harbison, *An Introduction to Radiation Protection*, 5th ed. Hodder Arnold, 2006.

Appendix A

Tumor Classification

A.1 Prostate Specific Antigen

Prostate Specific Antigen (PSA), is a protein (glycoprotein of the kallikrein family - kallikrein 3) produced by the cells of the Prostate Gland. The size of the prostate gland is similar to that of a pea at birth, and it continues to grow as the man ages. By the time the child has reached puberty the size of the prostate is doubled. The size of the prostate of an adult is comparable to that of a walnut. The prostate specific antigen is found in small quantities in the serum of normal men, whereas in men with prostate cancer or other prostate disorders, the quantities of PSA are usually elevated. Table A.1 shows the normal PSA values for men of different races from different age groups [64]. PSA is useful in the early detection, staging and follow-up of patients who have prostate cancer [65]. A PSA level of 4ng/ml or under are considered normal while level over 4ng/ml are considered abnormal.

Table A.1: PSA values for different ages groups and races

Age	Caucasian	Blacks	Asian
40~49	2.5	2	2
50~59	3.5	4	3
60~69	4.5	4.5	4
70~79	6.5	5.5	5

The possible cause of prostate cancer is unknown, but it is thought to be mostly related to unhealthy diet, age, genetics, heredity, etc. Measuring PSA level in blood, known as a PSA test, is the most effective way right now to determine prostate cancer. A rise in PSA levels over time indicate prostate cancer or benign (not cancerous) conditions. The most common form of benign condition is Benign Prostatic Hyperplasia, which is the englargement of the prostate gland; or Prostatitis, which is the inflammation or infection of the prostate gland [66]. Therefore, a single level of PSA is an unreliable measure of the extent of the disease in this context.

Scientists at Michigan Medical School discovered a possible cause for prostate cancer, their findings show that in prostate cancer cases, specific genes merge due to a recurring pattern of scrambled chromosomes. The outcome of this research is aimed at developing more accurate diagnosis of the disease, as well as improving its treatment [67].

Recently, the BBC has reported that men with longer index fingers than their ring fingers are less likely to develop prostate cancer. However, the lead of this research, Dr. Helen Rippon also states that men with shorter index fingers does not imply that they will definitely develop prostate cancer [68].

A.2 Gleason Score

The Gleason score, or the Gleason grading system is the sum of two numbers that classifies the grade or the stage of the prostate cancer. The first number defines the most common tumor pattern and is given a number of 1 to 5, where 1 implies that the cancerous prostate closely resembles healthy prostate tissue, and 5 implies that the prostate gland is no longer recognizable. The second number defines the second most common tumor pattern, and is numbered in the same way as the first number.

Table A.2: Non-small cell lung carcinoma staging

Categories	TNM staging
Stage 1A	T1 N0 M0
Stage 1B	T2 N0 M0
Stage 2A	T1 N1 M0
Stage 2B	T2 N1 M0 T3 N0 M0
Stage 3A	T1 N2 M0 T2 N2 M0 T3 N1 M0 T3 N2 M0
Stage 3B	Any T N3 M0 T4 Any N M0
Stage 4	Any T Any N M1

Thus the lowest Gleason score is 2, and the highest Gleason score is 10, which is the worst prognosis. It is important to point out that a Gleason score of $4 + 3 = 7$ is more severe than a Gleason score of $3 + 4 = 7$.

A Gleason score of $2 - 4$ is categorized as Grade 1 (G1), a Gleason score of $5 - 6$ is categorized as Grade 2 (G2) and a Gleason score of $7 - 10$ is categorized as Grade 3 (G3) [65].

A.3 Lung Cancer Staging

The two most common classifications of lung cancer are Non-Small Cell Lung Carcinoma (NSCLC), and Small Cell Lung Carcinoma (SCLC), with the latter being less common. SCLC is strongly associated with smoking, while lung cancer patients who have never smoked before are commonly diagnosed with NSCLC [69]. For NSCLC, the severity of the tumor is described by threes letter, T, M and N.

T stands for tumor size and invasiveness, which ranges from T1 to T4. T1 tumors are $< 3cm$; T2 tumors are either $> 3cm$ or extend into the main bronchus; T3 tumors

extend into the chest, but may be operable; T4 tumors invade the mediastinum (the area and organs between the lungs) and cannot be surgically resected. N stands for Nodal involvement, which ranges from N0 to N3. N0 imples that there is no regional lymph node metastasis; N1 implies metastasis to ipsilateral peribronchial and/or ipsilateral hilar lymph nodes; N2 implies metastasis to ipsilateral mediastinal, and/or subcarinal lymph node(s); and N3 is metastasis to contralateral mediastinal, contralateral hilar, ipsilateral or contralateral scalene, or spraclavicular lymph node(s) [70]. M stands for metastases, where M0 indicates no distant metastasis present while M1 means distant metastasis is present.

In [71], NSCLC are further categorized as in Table A.2. It can be seen in this table that Stage 4 is the worst diagnosis since the tumor is spreading as indicated by M1, with a one year survival rate of 19% and five year survival rate of 1% [72].

A.4 Clinical Staging for Prostate Cancer

In prostate cancer, clinical staging is an expression of both tumor volume and extent of disease (EOD). Clinical staging for prostate cancer uses the same TNM convention as for lung cancer; more specifically, T refers to the size of the primary tumor in the prostate (T1 to T4); N refers to the involvement of and cancer spread to the lymph nodes, where N0 implies there is no regional lymph node metastasis and N1 implies there is metastasis in the regional lymph node(s); and M (metastases) refers to whether the cancer has spread to other body parts, where M0 means there is no distant metastasis and M1 means distant metastasis is present [73].

Furthermore, there are four categories that further classify the clinical stage of the primary tumor (T) [65, 73], which is given below in Table A.3.

Table A.3: Clinical staging of primary tumor (T)

T1	**Clinically inapparent tumor not palpable or visible by imaging**
T1a	Tumor incidental histological finding in 5% or less of tissue resected
T1b	Tumor incidental histological finding in more than 5% of tissue resected
T1c	Tumor identified by needle biopsy (e.g. because of elevated PSA)
T2	**Tumor confined within the prostate**
T2a	Tumor involves one of the prostate gland's two lobes
T2b	Tumor involves both of the prostate gland's two lobes
T3	**Tumor extends through the prostate capsule**
T3a	Unilateral extracapsular extension
T3b	Bilateral extracapsular extension
T3c	Tumor invades the seminal vesicle(s)
T4	**Tumor invades any of bladder neck, external sphincter, or rectum**
T4a	Tumor invades any of bladder neck, external sphincter or rectum
T4b	Tumor invades levator muscles and/or the pelvic wall

Based on the T, N and M values given above, as well as the Gleason score grades, there are also four groups that differentiate the severity of prostate cancer, which is shown in Table A.4.

Table A.4: TNMG stage grouping for prostate cancer

Categories	**TNM staging**
Stage 1	T1a N0 M0 G1
Stage 2	T1a N0 M0 G2/G3 T1b N0 M0 Any G T1c N0 M0 Any G T1 N0 M0 Any G T2 N0 M0 Any G
Stage 3	T3 N0 M0 Any G
Stage 4	T4 N0 M0 Any G Any T N1 M0 Any G Any T Any N M1 Any G

Appendix B

Dose Rate and Dose

B.1 Dose Rate

The Dose Rate ($\dot{D}(r)$) for a point source approximation as given in [5] is as follows:

$$\dot{D}(r) = S_k \cdot \Lambda \cdot g(r) \cdot G(r, \Theta) \cdot \Phi_{an}(r) \tag{B.1}$$

- S_k is the initial activity of the source in units of U, where $1U$ is equal to 1 unit of air kerma strength. The quantity *kerma*, which is short for *kinetic energy released* per unit *mass*, refers to the amount of kinetic energy liberated by uncharged particles such as photons from charged particles such as electrons and positrons. The kerma can be expressed as joules per kilogram (J/kg), which is equivalent to the unit of absorbed dose, gray (Gy). Air kerma strength is a measure of the brachytherapy source strength, which is defined as the product of air kerma rate at a calibration distance, d, in free space, $\dot{K}(d)$, and the square of the distance, d. $\dot{K}(d)$ is measured along the transverse bisector of the source. So,

$$S_k = \dot{K}(d) \cdot d^2 \tag{B.2}$$

Table B.1: Recommended dose rate constant in a water medium

Seed	cGy $hr^{-1}U^{-1}$
^{192}Ir	1.12
^{125}I Model 6702	0.93
^{125}I Model 6711	0.88
^{103}Pd	0.74

So if kerma, time and distance are specified in units of μGy, h, and m, respectively, then S_k will have units of μGy m^2h^{-1} [5]. Then,

$$\begin{aligned} 1\ \mathrm{U} &= 1\ \mu Gy\ m^2\ h^{-1} \\ &= 1\ cGy\ cm^2\ h^{-1} \end{aligned} \tag{B.3}$$

The calibration of the source must be done at a distance d large enough so that the source can be treated as a mathematical point. Though, it is customary to specify the air kerma strength at a reference calibration distance, d_0, of $1m$. Kerma rate, $\dot{K}$, can usually be defined for a specific material at a point inside a medium; in this case the medium is air. The unit of kerma rate is $Jkg^{-1}s^{-1}$, and is given as the derivative determined from the amount of change in kerma, dK, over the time interval, dt, i.e.,

$$\dot{K} = \frac{dK}{dt} \tag{B.4}$$

- Λ is the dose rate constant, the precise definition is given in [5] which basically translates to the dose rate at a distance of $1cm$ in water for a source with air kerma strength of $1U$. The $1cm$ used in determining the value of the source is specified along the transverse axis of the actual source, as opposed to an idealized point source. The dose rate constant is an absolute quantity, which

accounts for geometric effects, source encapsulation, scattering in water, as well as radioactivity and self-filtration within the source. The recommended dose rate constant in a water medium is given by [5] in Table B.1.

Three models of the ^{125}I seed are mentioned in [5], they are the 6711 model, 6702 model and the 2300 model. However, only the first two models are described in detail in [5]. Since sufficient information has been provided by [5] for the 6711 model of the ^{125}I seed, it is chosen for this thesis. Due to the fact that the human body can be considered as a water medium for research purposes, a value of $0.88cGyh^{-1}U^{-1}$ is used for Λ in Eq. (B.1) [5].

- $g(r)$ is the radial dose function, which accounts for absorption and scattering effects in the medium along the transverse axis of the source. The values for $g(r)$ at different distances along the transverse axis areis given in Table B.2. As is evident from the data in Table B.2, the values of $g(r)$ define the falloff of dose rate along the transverse axis due to absorption and scattering in the medium.

- Due to the spatial distribution of activity within the source, the relative dose is varied. This variation is accounted for by the geometry factor $G(r, \Theta)$, which can be approximated as $\frac{1}{r^2}$ for a point source [5]. It ignores the effects due to photon absorption and scattering in the source structure.

- $\Phi_{an}(r)$ is the anisotropy factor. Though as suggested in [5], for the 6711 model of the ^{125}I seed, $\Phi_{an}(r)$ can be approximated by a distance-independent constant, $\bar{\Phi}_{an}$, which is called the anisotropy constant and is usually less than 1.00. The particular value used in this thesis for the 6711 model of the ^{125}I seed, which is given in [5], is 0.93.

Table B.2: Radial dose function, g(r)

Distance along transverse axis(cm)	Radial dose function, g(r)	
	^{125}I Model 6711	^{125}I Model 6702
0.5	1.04	1.04
1.0	1.00	1.00
1.5	0.926	0.934
2.0	0.832	0.851
2.5	0.731	0.760
3.0	0.632	0.670
3.5	0.541	0.586
4.0	0.463	0.511
4.5	0.397	0.445
5.0	0.344	0.389
5.5	0.300	0.341
6.0	0.264	0.301
6.5	0.233	0.266
7.0	0.204	0.235

B.2 Dose

In order to calculate the dose at a particular point, a conversion is required to convert $\dot{D}(r)$ to $D(r)$.

The mean life of a radionuclide is given by

$$\tau = \frac{1}{\lambda} \tag{B.5}$$

where λ is the decay constant of the source radionuclide, and

$$\lambda = \frac{ln(2)}{T_{1/2}} \tag{B.6}$$

and $T_{1/2}$ is the half-life of the radionuclide.

Equation (8.56) in [7] is equivalent to Eq. (B.7) for a point source approximation,

$$D(r) = \dot{D}(r)\tau(1 - e^{-\frac{T}{\tau}}) \tag{B.7}$$

where $e^{-\frac{T}{\tau}} \approx 0$ for LDR in particular, since for permanent implants (LDR), T, the irradiation time, is much higher than the mean life of the radionuclide τ, so $T \gg \tau$. For a source whose τ is expressed in *hours*, the corresponding value of the time conversion factor k_u (expressed in *hours*) is equal to 1. Therefore, the dose for a ^{125}I source with a half-life of 1426 hours, is given by

$$\begin{aligned} D(r) &= \dot{D}(r) \cdot \tau \cdot k_u \\ &= S_k \cdot \Lambda \cdot g(r) \cdot G(r,\Theta) \cdot \bar{\Phi}_{an} \cdot \frac{T_{1/2}}{ln(2)} \cdot k_u \\ &= S_k \cdot 0.88 \cdot g(r) \cdot \frac{1}{r^2} \cdot 0.93 \cdot 1.443 \cdot 1426 \cdot 1 \end{aligned} \tag{B.8}$$

Appendix C

Radiation

C.1 Radiation

The most significant effect of ionizing radiation is the damage to cells, mainly through damage to the Deoxyribonucleic Acid (DNA). Even subtle damage to the DNA could lead to mutations, which would further lead to cancer. When the dose is high enough, radiation effectly kills cells [74]. Generally speaking, cells under rapid division are more sensitive to damage by radiation, such as the gonads in males and the uterine area in females, as compared to muscles and nerves that divide slower and are not easily damaged. In a way, this could be understood as that the radiosensitivity of a cell type is proportional to its rate of division [75].

The two broad categories of radiation-related effects in humans are stochastic and nonstochastic [75]. Effects that are generally observable soon after exposure to radiation are called *nonstochastic effects*. Some examples of the damage done by ionizing radiation for this category include depression of bone marrow cell division, or NVD (nausea, vomiting, diarrhea) that is often observed in victims after radiation exposure in the central nervous system. Here, a few examples are given regarding the effects due to various amount of doses [74],

- 2 to $3Gy$ to the skin can result in the reddening of the skin, similar to a mild sunburn. May also result in hair loss due to damage to hair follicles.

Table C.1: Differences between stochastic and nonstochastic radiation effects

Characteristic effects of Nonstochastic Effects	**Characteristic effects of Stochastic Effects**
A threshold exists below which the effects will not be observed	A threshold may not exist
The magnitude of the effect increases with dose above this threshold	The probability of the effect increases with dose
Effect is clearly associated with the radiation exposure	Effect cannot be definitively associated with the radiatione exposure

- $6Gy$ to the ovaries or testicles can result in permanent sterilization.
- $0.5Gy$ to the thyroid gland can result in benign tumors, which are noncancerous.

The **Gray (Gy)** is the SI unit for the absorbed dose, which is defined by [76] as a measure of energy deposition in any medium by any type of ionizing radiation. $1Gy$ is equivalent to 1 joule of energy per kilogram of mass. The mathematical equation for absorbed dose is [7],

$$D = \frac{d\varepsilon}{dm} = \frac{1}{\rho}\frac{d\varepsilon}{dV} \tag{C.1}$$

where $d\varepsilon$ is the mean energy imparted in a volume of mass dm, and $dm = \rho dV$. The traditional unit for absorbed dose is **rad**, where 1 rad is the equivalent of $1cGy$ (centigray) and $100cGy$ is equal to $1Gy$.

The other category of radiation-related effects, *stochastic effects*, are effects that are probabilistic. Examples of this type of effects include cancer induction and genetics effects that may affect offspring. The three important characteristics that distinguish between the two categories are given in Table C.1.

Together with the abosorbed dose described above, there are three other quantities that are of interest to radiation measurements, and they are the equivalent dose, radioactivity and exposure [74]. The equivalent dose takes into consideration that

not all types of radiation would have the same effect in biological systems. Thus it is necessary to apply a quality factor (Q) which essentially represents the ability of the particular type of radiation to cause damage [76]. Mathematically, the equivalent dose is expressed as,

$$\text{equivalent dose} = \text{absorbed dose} \times Q \tag{C.2}$$

where the SI unit for equivalent dose is the **Sievert (Sv)**, and the absorbed dose is in units of Gy. The value of Q is 1 for x-rays, γ-rays and electrons, while for alpha particles, the value of Q is 20. The sievert is a very large dose of radiation. A more useful unit is the millisievert (mSv). The dose received by human beings around the globe due to cosmic background radiation is about $3mSv$ per year. The traditional unit for equivalent dose is **rem**, short for Röntgen Equivalent in Man. 1 rem is equal to $0.01Sv$.

A precise definition for exposure is given in [75], which basically translates to the sum of one type of ion produced by radiation, divided by the mass of air. The SI unit of exposure is C/kg, whereas the traditional unit is the **Röntgen (R)**, which is the same as $2.58 \times 10^{-4} C/kg$.

The radioactivity is defined as the number of nuclear transformations per unit time occurring in a given sample of radioactive material. Mathematically, this can be defined as,

$$A = \frac{dN}{dt} \tag{C.3}$$

where dN is the number of decays observed during the time interval dt. The traditional unit of radioactivity is the **Curie (Ci)**, which is equal to 3.7×10^{10} transformations per second. The SI unit for radioactivity is the **Becquerel (Bq)**, which is

Table C.2: Units used in measuring ionizing radiation

Quantity	Definition	Units
Absorbed dose	The amount of energy deposited per unit mass	SI unit: gray (Gy) 1 Gy = 1J/kg Historic unit: rad 1 rad = 100 erg/g 100 rad = 1 Gy
Equivalent dose	Product of the absorbed dose and the quality factor Q	SI unit: sievert(Sv) SI unit: Sievert (Sv) Historic unit: rem rem=rad × Q 1 Sv = 100 rem
Radioactivity	The number of decays over a given time	SI unit: Becquerels (Bq) Historic unit: Curie (Ci) 1 Bq = 27 pCi 1 Ci = 37 billion Bq
Exposure	The Röntgen is defined as the generation of 1 electrostatic unit of charge per 1 cm^3 of air	SI unit: C/kg Historic unit: Röntgen (R)

equivalent to a single transformation, so that $1Ci = 3.7 \times 10^{10} Bq$. Table C.2 presents the quantities mentioned above, along with their SI and traditional units.

In the United States, brachytherapy sources are still sometimes specified according to the traditional units. For instance, the nominal value of a ^{125}I source may be specified as $0.41mCi$ (range 0.16 to $1mCi$) [9], instead of using the SI units.

Appendix D

Radioactivity of ^{125}I

D.1 Radioactivity of ^{125}I

Iodine 125, or ^{125}I, is currently the most commonly selected source for low dose rate brachytherapy, especially for permanent interstitial implants for prostate cancer [7]. It is an isotope of $^{127}_{53}$I. The ^{125}I radionuclide was discovered in 1946 by Allen Reid and Albert Keston, though the clinical use of ^{125}I for interstitial brachytherapy did not take place for another 20 years [7]. ^{125}I is usually created from ^{125}Xe, which is usually created from ^{124}Xe in a nuclear reactor. The decay chain of ^{125}I is shown below in Eq. (D.1),

$$^{125}_{54}Xe \rightarrow ^{125}_{53}I \rightarrow ^{125}_{52}Te \tag{D.1}$$

$T_{1/2}$ associated with $^{125}_{54}$Xe is $16.9h$ while $T_{1/2}$ associated with $^{125}_{53}$I is $59.49d$.

^{125}I decays to the first excited state of ^{125}Te through electron capture, a process during which 1 electron had been sacrificed. 7% of the de-excitation to the ground state of ^{125}Te is via emission of a $35.5keV$ γ-ray, which is also known as gamma decay. Meanwhile, 93% of the de-excitation is through internal conversion, which gives rise to characteristic x-rays. Model 6711 employed by this research emits silver characteristic x-rays with energies of 22.1 and $25.5keV$. The average photon energy for this type of seed is $27.4keV$, with an average of 1.4 photons being emitted for every disintegration of ^{125}I.

Since the energy of the emitted photons is very low, minimum effort is required regarding shielding thus making the handling of the sources easy and safe. In particular, the HVL, or Half Value Layer, of lead for ^{125}I is as thin as $0.025mm$ [6]. HVL is defined as the thickness of the material, usually lead, required to reduce the radiation of a source to half of its original amount. Therefore, a radioactive source that emits high energy photons usually requires a higher HVL value.

Although the main current application field of ^{125}I radionuclide is for low dose rate prostate brachytherapy, it has also been used for permanent interstitial implants for lung, pancreas and breast cancer; as well as temporary and permanent interstitial implants for brain tumors [7].